

**Frequency Response of Microcantilevers in Gas, Liquid and  
Supercritical CO<sub>2</sub>**

by

**Erdal Uzunlar**

**A Thesis Submitted to the  
Graduate School of Sciences and Engineering  
in Partial Fulfillment of the Requirements for  
the Degree of**

**Master of Science**

in

**Chemical and Biological Engineering**

**Koç University**

**August 2010**

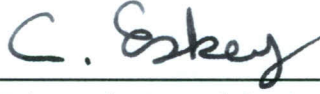
Koç University  
Graduate School of Sciences and Engineering

This is to certify that I have examined this copy of a master's thesis by

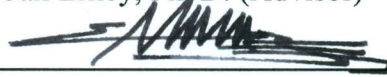
Erdal Uzunlar

and have found that it is complete and satisfactory in all respects,  
and that any and all revisions required by the final  
examining committee have been made.

Committee Members:



Can Erkey, Ph. D. (Advisor)



B. Erdem Alaca, Ph. D.



Hakan Ürey, Ph. D.

Date:

August 2, 2010

*To my family and my fiancée*

## ABSTRACT

Micromechanical resonators have been extensively studied in recent years because of their potential for high-sensitive, low cost, compact device applications, such as *in situ* viscometers and densitometers. This thesis is the first study in the literature that investigates the response of microcantilevers in a supercritical fluid. In this study, the frequency response of microcantilevers in CO<sub>2</sub> was investigated in order to relate the thermophysical properties such as density ( $\rho$ ), viscosity ( $\eta$ ) and isothermal compressibility ( $K_T$ ) to the resonance frequency ( $f_R$ ), quality factor ( $Q$ ) and damping parameter ( $\beta$ ). 200  $\mu\text{m}$ , 225  $\mu\text{m}$ , 250  $\mu\text{m}$  long, 20  $\mu\text{m}$  wide and 1  $\mu\text{m}$  thick multilayered Ni microcantilevers consisting thin Cr and Au films were fabricated by conventional microfabrication techniques. The cantilevers were placed in a high pressure view cell equipped with a custom designed Teflon housing holding the microcantilever chip and the electromagnetic coil which was actuated sinusoidally. A Laser Doppler Vibrometer (LDV) was used for detection. Experiments were carried out in the pressure range of 1 atm to 200 atm and at 25 °C, 35 °C, 45 °C and 55 °C. First, it was observed that  $f_R$  decreased with increasing  $\rho$  and  $Q$  decreased with increasing  $\eta$ . The changes in  $f_R$  and  $Q$  were larger in the gas phase than those in the liquid or supercritical (sc) phase. Second,  $f_R$  was observed to vary linearly with  $\rho$  as well as  $(\rho\eta)^{0.5}$  in the gas phase which enabled the determination of  $\rho$  and  $\eta$  through calibration with percentage errors less than 1 %. A quadratic relationship was observed between  $Q$  and  $\eta$ . Apart from that, the decreases of  $f_R$  observed in successive measurements (i.e. drifts) at a constant temperature and pressure were found to correspond to the shifts of the maxima of the density multiplied by compressibility, defined as  $-\rho K_T = \left(\frac{\partial \rho}{\partial P}\right)_T$ . Moreover, microscale bubbles were observed at a pressure less than the bubble point pressure at 25 °C due to heating of cantilevers by LDV.

## ÖZETÇE

Mikro-mekanik çınlaçlar, yüksek hassasiyetleri, ucuz maliyetleri gibi potansiyel faydaları nedeniyle ağıdalıkölçer ve yoğunlukölçer gibi aygıt uygulamalarında son yıllarda yoğun bir şekilde araştırılmaktadır. Bu tez, mikro-çubukların sıklık yanıtlarının süperkritik akışkanlar içinde incelendiği literatürdeki ilk çalışmadır. Bu çalışmada, mikro-çubukların karbondioksit içindeki sıklık yanıtları kullanılarak, çınlaçların çınlanım sıklığı ( $f_R$ ), nitelik katsayıları ( $Q$ ), ve sönüm katsayıları ( $\beta$ ) ile deney yapılan ortamın yoğunluk ( $\rho$ ), ağıdalık ( $\eta$ ) ve eşsıcaklıklı sıkışırılık ( $K_T$ ) gibi termo-fiziksel özellikleri arasındaki ilişkiler araştırıldı. Uzunlukları 200  $\mu\text{m}$ , 225  $\mu\text{m}$  ve 250  $\mu\text{m}$ , genişlikleri 20  $\mu\text{m}$  ve kalınlıkları 1  $\mu\text{m}$  olan, ince Cr ve Au yaygı içeren çokkatmanlı Ni mikro-çubuklar, geleneksel mikro-yapım teknikleriyle üretildi. Çubuklar, mikro-çubuk yongasını ve sinüsoidal biçimde tahrik edilen elektromıknatısı titreşimsiz tutan özel tasarlanmış Teflon muhafaza yardımıyla, camlı yüksek basınç kabına yerleştirildi. Algılama için bir Lazer Dopler Titreşimölçer kullanıldı. 1 ve 200 atm basınç aralığında 25 °C, 35 °C, 45 °C ve 55 °C sıcaklıklarda deneyler yapıldı. Çınlanım sıklıklarının yoğunlukla, nitelik katsayılarının ise ağıdalıkla azaldığı gözlemlendi. Gaz fazındaki çınlanım sıklığı ve nitelik katsayılarındaki değişmelerin, sıvı veya süperkritik faza oranla daha fazla olduğu kaydedildi. Çınlanım sıklığının gaz fazındaki yoğunluk ve  $(\rho\eta)^{0.5}$  ile doğrusal değişimi kullanılarak basit bir kalibrasyon yöntemiyle, bu fazdaki yoğunluk ve ağıdalık değerlerinin % 1'den küçük hata paylarıyla hesaplanabildiği görüldü. Nitelik katsayıları ve ağıdalık arasında ikinci dereceden bir ilişki olduğu anlaşıldı. Ek olarak, sabit bir basınç ve sıcaklıkta ardıl çınlanım sıklığı ölçümlerindeki azalmaların, yoğunlukla eşsıcaklıklı sıkışırılık katsayıları çarpımının,  $-\rho K_T = \left(\frac{\partial \rho}{\partial P}\right)_T$ , çıkaç değerlerindeki kaymaya karşılık geldiği gözlemlendi. Ek olarak, 25 °C'de kaynama noktasından düşük bir basınçta, Lazer Dopler Titreşimölçer'in verdiği ısıyla ısınan mikro-çubuklar etrafında mikro-boyutlu kabarcıkların oluştuğu gözlemlendi.

## ACKNOWLEDGEMENTS

I would like to express my gratitude for enthusiastic supervision of my advisor Prof. Can Erkey. The guidance and support combined with kindness and sincerity of Prof. Erkey encouraged me to find my niche that is to pursue my doctorate studies. I would like to thank Asst. Prof. B. Erdem Alaca and Assc. Prof. Hakan Ürey for their generous guidance in the fields of mechanics and electronics which are normally unknown to me. I am grateful to all my friends in Boğaziçi University and Koç University, to name some, the members of Energy Technologies and Supercritical Fluids Laboratory Selmi E. Bozbağ, Deniz Şanlı, N. Seda Yaşar, A. Meriç Kartal, Seda Giray and N. Ezgi Dinçer, my comrades from Boğaziçi Onur Dinçel, Kaan Ayaz and Meriç Ataman, my friends M. Salih Kılıç, Serhat Yavuz, Enis Demir and Zeynep Ülker and my best friends İzzet Yıldız, Evren F. Arkan, Şeyda İpek and Onur Öztaş.

Above all, I praise to God for endowing me with a wonderful family full of love, patience and support. I also praise to God for sending an angel to Earth for me, my fiancée Sibel Kalyoncu.

## TABLE OF CONTENTS

<b>List of Tables</b> .....	<b>x</b>
<b>List of Figures</b> .....	<b>xi</b>
<b>Nomenclature</b> .....	<b>xviii</b>
<b>1 Introduction</b> .....	<b>1</b>
1.1 Overview .....	1
1.1.1 Microcantilever Uses and Operation in Fluids .....	1
1.1.2 Supercritical CO <sub>2</sub> (scCO <sub>2</sub> ) .....	3
1.2 Literature Review .....	4
1.3 Statement of the Problem .....	9
1.4 Outline .....	10
<b>2 Device Fabrication</b> .....	<b>11</b>
2.1 Fabrication Flow .....	11
2.1.1 Substrate Preparation .....	11
2.1.2 Seed Layer Formation .....	11
2.1.3 Mold-pattern preparation .....	13
2.1.4 Structural layer formation .....	14
2.1.5 Wet-etching of Au and Cr layers .....	16
2.1.6 Final cleaning .....	17
2.2 Encountered problems .....	18
2.2.1 White precipitate occurring after Au etchant .....	18
2.2.2 Over-etching of Si substrate .....	20
<b>3 Measurement Setup and Procedure</b> .....	<b>21</b>
3.1 Interferometry and Measurement Setup .....	21
3.2 Experimental Conditions .....	25
3.2.1 Measurements in Air .....	26

3.2.2	Measurements in Pressurized CO <sub>2</sub> .....	26
<b>4</b>	<b>Results and Discussion.....</b>	<b>29</b>
4.1	Measurements in Air at P=1 atm.....	29
4.2	Measurements in Pressurized CO <sub>2</sub> .....	32
4.2.1	$f_R$ vs P.....	33
4.2.2	$f_R$ vs $\rho$ .....	38
4.2.3	$f_R$ vs $(\rho\eta)^{0.5}$ .....	42
4.2.4	Q vs P.....	44
4.2.5	Q vs $\eta$ .....	46
4.2.6	$\beta$ vs $\eta^{0.5}$ .....	47
<b>5</b>	<b>Conclusion.....</b>	<b>51</b>
5.1	Conclusion.....	51
5.2	Suggestions for further studies.....	52
5.3	Future Work.....	55
<b>Appendix</b>	<b>.....</b>	<b>57</b>
A.1	Raw Experimental Data.....	57
A.1.1	Raw Data for L=200 $\mu\text{m}$ .....	57
A.1.2	Raw Data for L=225 $\mu\text{m}$ .....	59
A.1.3	Raw Data for L=250 $\mu\text{m}$ .....	61
A.2	Density and Viscosity in the Experimental Conditions.....	64
A.2.1	Density Change in the Experimental Range.....	64
A.2.2	Viscosity Change in the Experimental Range.....	65
A.3	Plotted Results.....	66
A.3.1	Results at T=25 °C.....	66
A.3.2	Results at T=35 °C.....	70
A.3.3	Results at T=45 °C.....	74
A.3.4	Results at T=55 °C.....	78
A.3.5	Results for L=200 $\mu\text{m}$ .....	82



A.3.6	Results for $L=225\ \mu\text{m}$ .....	85
A.3.7	Results for $L=250\ \mu\text{m}$ .....	88
A.4	$\text{CO}_2$ Compressibility Calculation .....	91
A.5	Written Matlab Codes .....	94
A.5.1	Code for Data Acquisition .....	94
A.5.2	Code for Lorentzian Fitting .....	96
<b>Bibliography</b>	.....	<b>99</b>

## List of Tables

Table 1.1: Comparison of thermophysical properties of gases, SCFs and liquids [20] .....	4
Table 3.1: Pressure and temperature for measurements in air .....	26
Table 3.2: Measurements in room temperature in pressurized CO <sub>2</sub> .....	27
Table 3.3: Measurements at 35 °C in pressurized CO <sub>2</sub> .....	27
Table 3.4: Measurements at 45 °C in pressurized CO <sub>2</sub> .....	28
Table 3.5: Measurements at 55 °C in pressurized CO <sub>2</sub> .....	28
Table 4.1: Density and viscosity values at P=1 atm in air .....	29
Table 4.2: Resonance spectra obtained in air .....	29
Table A.1: Raw data for L=200 μm at room temperature .....	57
Table A.2: Raw data for L=200 μm at T=35 °C .....	58
Table A.3: Raw data for L=200 μm at T=45 °C .....	58
Table A.4: Raw data for L=200 μm at T=55 °C .....	59
Table A.5: Raw data for L=225 μm at room temperature .....	59
Table A.6: Raw data for L=225 μm at T=35 °C .....	60
Table A.7: Raw data for L=225 μm at T=45 °C .....	60
Table A.8: Raw data for L=225 μm at T=55 °C .....	61
Table A.9: Raw data for L=250 μm at room temperature .....	61
Table A.10: Raw data for L=250 μm at T=35 °C .....	62
Table A.11: Raw data for L=250 μm at T=45 °C .....	62
Table A.12: Raw data for L=250 μm at T=55 °C .....	63
Table A.13: Average $-\rho K_T$ values at experimental data points .....	93

## List of Figures

Figure 1.1: Representative Lorentzian fit to resonance spectrum .....	2
Figure 1.2: The pressure-temperature diagram of a pure substance .....	3
Figure 2.1: Fabrication flow: (i) Standard cleaning of <100> 525±25 μm thick 4” Si wafer (ii) Sputtering of 20 nm layer of Cr and (iii) 120 nm Au by RF-Magnetron (iv) Spin-coating with AZ 5412 photoresist and soft-baking (v) UV photolithography and the pattern development by AZ 400K remover (vi) The wafer is sliced into dice and Ni electroplating is conducted for each die (vii) Removal of photoresist by AZ 100 remover (viii) Au layer etching using Transene TFAC Ni-selective Au etchant (ix) Cr layer etching using MicroChrome TFE Cr etchant (x) Si substrate is wet etched using KOH solution and the free-standing multilayered cantilevers are achieved.....	12
Figure 2.2: The demonstration of patterns formed using positive and negative photoresists [35] .....	13
Figure 2.3: Schematic representation of electroplating process [36] .....	15
Figure 2.4: The mask drawing of a die showing the four edges for electrical connection during electroplating.....	15
Figure 2.5: A portion of fabricated microcantilevers that are ready for measurement .....	18
Figure 2.6: White precipitate occurred after gold etching. a. Cantilever focused b. Si substrate focused .....	19
Figure 2.7: Over-Si etched die (back view) a. Label focused b. Si substrate focused c. The die .....	20
Figure 3.1: LDV interferometry [40] .....	22
Figure 3.2: The schematic description of the measurement setup .....	22

Figure 3.3: Custom-made Teflon housing for immobilization of MCs and electromagnetic coil .....	23
Figure 3.4: The experimental setup. (a) Oscilloscope (b) Signal Generator (c) Preamplifier (d) CRT TV (e) LDV control unit (f) Pressure Vessel (g) LDV laser unit (h) Temperature and Pressure Indicators (i) Recirculator (j) Passive vibration isolation pads.....	24
Figure 3.5: A sample response curve and the Lorentzian fit with the parameters vacuum resonance frequency $f_0$ , damping parameter $\beta$ , resonance frequency $f_R$ and quality factor $Q$ .....	25
Figure 4.1: $f_R$ vs $T$ .....	30
Figure 4.2: $Q$ vs $T$ .....	30
Figure 4.3: $\beta$ vs $T$ .....	30
Figure 4.4: $f_R$ vs $\rho$ .....	30
Figure 4.5: $Q$ vs $\eta$ .....	31
Figure 4.6: $f_R$ vs $P$ at $T=25$ °C .....	33
Figure 4.7: $f_R$ vs $P$ at $T=35$ °C .....	33
Figure 4.8: $f_R$ vs $P$ at $T=45$ °C .....	33
Figure 4.9: $f_R$ vs $P$ at $T=55$ °C .....	33
Figure 4.10: Video capture of bubbling of $CO_2$ on microcantilevers at bubble point .....	34
Figure 4.11: $f_R$ and $-\rho K_T$ vs $P$ at $T=35$ °C.....	35
Figure 4.12: $f_R$ and $-\rho K_T$ vs $P$ at $T=45$ °C.....	35
Figure 4.13: $f_R$ and $-\rho K_T$ vs $P$ at $T=55$ °C.....	36
Figure 4.14: $-\rho K_T$ vs $P$ at all $T$ .....	36
Figure 4.15: $f_R$ vs $P$ for $L=200$ $\mu m$ .....	36
Figure 4.16: $f_R$ vs $P$ for $L=225$ $\mu m$ .....	36
Figure 4.17: $f_R$ vs $P$ for $L=250$ $\mu m$ .....	37

Figure 4.18: Real part of hydrodynamic function vs $\kappa^2 - \zeta^2$ [18] .....	37
Figure 4.19: $f_R$ vs $\rho$ at $T=25$ °C .....	38
Figure 4.20: $f_R$ vs $\rho$ at $T=35$ °C .....	38
Figure 4.21: $f_R$ vs $\rho$ at $T=45$ °C .....	39
Figure 4.22: $f_R$ vs $\rho$ at $T=55$ °C .....	39
Figure 4.23: $f_R$ vs $\rho$ at $T=25$ °C (gas) .....	40
Figure 4.24: $f_R$ vs $\rho$ at $T=35$ °C (gas) .....	40
Figure 4.25: $f_R$ vs $\rho$ at $T=45$ °C (gas) .....	40
Figure 4.26: $f_R$ vs $\rho$ at $T=55$ °C (gas) .....	40
Figure 4.27: $f_R$ vs $(\rho\eta)^{0.5}$ at $T=25$ °C .....	42
Figure 4.28: $f_R$ vs $(\rho\eta)^{0.5}$ at $T=35$ °C .....	42
Figure 4.29: $f_R$ vs $(\rho\eta)^{0.5}$ at $T=45$ °C .....	43
Figure 4.30: $f_R$ vs $(\rho\eta)^{0.5}$ at $T=55$ °C .....	43
Figure 4.31: $f_R$ vs $(\rho\eta)^{0.5}$ at $T=25$ °C (gas) .....	44
Figure 4.32: $f_R$ vs $(\rho\eta)^{0.5}$ at $T=35$ °C (gas) .....	44
Figure 4.33: $f_R$ vs $(\rho\eta)^{0.5}$ at $T=45$ °C (gas) .....	44
Figure 4.34: $f_R$ vs $(\rho\eta)^{0.5}$ at $T=55$ °C (gas) .....	44
Figure 4.35: $Q$ vs $P$ at $T=25$ °C .....	45
Figure 4.36: $Q$ vs $P$ at $T=35$ °C .....	45
Figure 4.37: $Q$ vs $P$ at $T=45$ °C .....	45
Figure 4.38: $Q$ vs $P$ at $T=55$ °C .....	45
Figure 4.39: $Q$ vs $\eta$ at $T=25$ °C .....	46
Figure 4.40: $Q$ vs $\eta$ at $T=35$ °C .....	46
Figure 4.41: $Q$ vs $\eta$ at $T=45$ °C .....	47
Figure 4.42: $Q$ vs $\eta$ at $T=55$ °C .....	47
Figure 4.43: $\beta$ vs $\eta^{0.5}$ at $T=25$ °C .....	48

Figure 4.44: $\beta$ vs $\eta^{0.5}$ at T=35 °C .....	48
Figure 4.45: $\beta$ vs $\eta^{0.5}$ at T=45 °C .....	48
Figure 4.46: $\beta$ vs $\eta^{0.5}$ at T=55 °C .....	48
Figure 4.47: $\beta$ vs $\eta^{0.5}$ at T=25 °C (gas) .....	49
Figure 4.48: $\beta$ vs $\eta^{0.5}$ at T=35 °C (gas) .....	49
Figure 4.49: $\beta$ vs $\eta^{0.5}$ at T=45 °C (gas) .....	50
Figure 4.50: $\beta$ vs $\eta^{0.5}$ at T=55 °C (gas) .....	50
Figure 5.1: Lids of the pressure vessel. a) Lathed front lid b) Back lid.....	53
Figure A.1: Density variation of CO <sub>2</sub> with respect to temperature and pressure.....	64
Figure A.2: Viscosity variation of CO <sub>2</sub> with respect to temperature and pressure .....	65
Figure A.3: $f_R$ vs P .....	66
Figure A.4: $f_R$ vs $\rho$ .....	66
Figure A.5: $f_R$ vs $\rho$ (liquid).....	67
Figure A.6: $f_R$ vs $\rho$ (gas).....	67
Figure A.7: $f_R$ vs $(\rho\eta)^{0.5}$ .....	67
Figure A.8: $f_R$ vs $(\rho\eta)^{0.5}$ (liquid).....	67
Figure A.9: $f_R$ vs $(\rho\eta)^{0.5}$ (gas).....	68
Figure A.10: Q vs P.....	68
Figure A.11: Q vs $\eta$ .....	68
Figure A.12: $\beta$ vs $\eta^{0.5}$ .....	69
Figure A.13: $\beta$ vs $\eta^{0.5}$ (liquid).....	69
Figure A.14: $\beta$ vs $\eta^{0.5}$ (gas).....	69
Figure A.15: $f_R$ vs P .....	70
Figure A.16: $f_R$ vs $\rho$ .....	70
Figure A.17: $f_R$ vs $\rho$ (sc, excluding drift).....	70
Figure A.18: $f_R$ vs $\rho$ (gas, ex. dr.).....	70

Figure A.19: $f_R$ vs $(\rho\eta)^{0.5}$ (ex. dr.).....	71
Figure A.20: $f_R$ vs $(\rho\eta)^{0.5}$ (sc, ex. dr.) .....	71
Figure A.21: $f_R$ vs $(\rho\eta)^{0.5}$ (gas, ex. dr.) .....	71
Figure A.22: Q vs P.....	72
Figure A.23: Q vs $\eta$ .....	72
Figure A.24: $\beta$ vs $\eta^{0.5}$ .....	72
Figure A.25: $\beta$ vs $\eta^{0.5}$ (sc, ex. dr.).....	72
Figure A.26: $\beta$ vs $\eta^{0.5}$ (gas, ex. dr.).....	73
Figure A.27: $f_R$ vs P .....	74
Figure A.28: $f_R$ vs $\rho$ .....	74
Figure A.29: $f_R$ vs $\rho$ (sc, ex. dr.).....	74
Figure A.30: $f_R$ vs $\rho$ (sc, ex. & after dr.) .....	74
Figure A.31: $f_R$ vs $\rho$ (gas, ex. dr.).....	75
Figure A.32: $f_R$ vs $(\rho\eta)^{0.5}$ (ex. dr.).....	75
Figure A.33: $f_R$ vs $(\rho\eta)^{0.5}$ (sc, ex. dr.) .....	75
Figure A.34: $f_R$ vs $(\rho\eta)^{0.5}$ (sc, ex. & af. dr.) .....	75
Figure A.35: $f_R$ vs $(\rho\eta)^{0.5}$ (gas, ex. dr.) .....	76
Figure A.36: Q vs P.....	76
Figure A.37: Q vs $\eta$ .....	76
Figure A.38: $\beta$ vs $\eta^{0.5}$ .....	77
Figure A.39: $\beta$ vs $\eta^{0.5}$ (sc, ex. dr.).....	77
Figure A.40: $\beta$ vs $\eta^{0.5}$ (sc, ex. & af. dr.) .....	77
Figure A.41: $\beta$ vs $\eta^{0.5}$ (gas, ex. dr.).....	77
Figure A.42: $f_R$ vs P .....	78
Figure A.43: $f_R$ vs $\rho$ .....	78
Figure A.44: $f_R$ vs $\rho$ (sc, ex. dr.).....	78

Figure A.45: $f_R$ vs $\rho$ (sc, ex. & af. dr.) .....	78
Figure A.46: $f_R$ vs $\rho$ (gas, ex. dr.).....	79
Figure A.47: $f_R$ vs $(\rho\eta)^{0.5}$ (ex. dr.).....	79
Figure A.48: $f_R$ vs $(\rho\eta)^{0.5}$ (sc, ex. dr.) .....	79
Figure A.49: $f_R$ vs $(\rho\eta)^{0.5}$ (sc, ex. & af. dr.) .....	79
Figure A.50: $f_R$ vs $(\rho\eta)^{0.5}$ (gas, ex. dr.) .....	80
Figure A.51: Q vs P.....	80
Figure A.52: Q vs $\eta$ .....	80
Figure A.53: $\beta$ vs $\eta^{0.5}$ .....	81
Figure A.54: $\beta$ vs $\eta^{0.5}$ (sc, ex. dr.).....	81
Figure A.55: $\beta$ vs $\eta^{0.5}$ (sc, ex. & af. dr.) .....	81
Figure A.56: $\beta$ vs $\eta^{0.5}$ (gas, ex. dr.).....	81
Figure A.57: $f_R$ vs P .....	82
Figure A.58: Q vs P.....	82
Figure A.59: $f_R$ vs $\rho$ .....	82
Figure A.60: Q vs $\eta$ .....	82
Figure A.61: $\beta$ vs $\eta^{0.5}$ .....	83
Figure A.62: $f_R$ vs $\rho$ (ex. dr.).....	83
Figure A.63: $f_R$ vs $\rho$ (liq. + sc, ex. dr.) .....	83
Figure A.64: $f_R$ vs $\rho$ (sc, ex. & af. dr.) .....	83
Figure A.65: $f_R$ vs $\rho$ (gas, ex. dr.).....	84
Figure A.66: $f_R$ vs $(\rho\eta)^{0.5}$ (ex. dr.).....	84
Figure A.67: $\beta$ vs $\eta^{0.5}$ (gas, ex. dr.) .....	84
Figure A.68: $f_R$ vs P .....	85
Figure A.69: Q vs P.....	85
Figure A.70: $f_R$ vs $\rho$ .....	85



Figure A.71: $Q$ vs $\eta$ .....	85
Figure A.72: $\beta$ vs $\eta^{0.5}$ .....	86
Figure A.73: $f_R$ vs $\rho$ (ex. dr.).....	86
Figure A.74: $f_R$ vs $\rho$ (liq. + sc, ex. dr.).....	86
Figure A.75: $f_R$ vs $\rho$ (sc, ex. & af. dr.) .....	86
Figure A.76: $f_R$ vs $\rho$ (gas, ex. dr.).....	87
Figure A.77: $f_R$ vs $(\rho\eta)^{0.5}$ (ex. dr.).....	87
Figure A.78: $\beta$ vs $\eta^{0.5}$ (gas, ex. dr.) .....	87
Figure A.79: $f_R$ vs $P$ .....	88
Figure A.80: $Q$ vs $P$ .....	88
Figure A.81: $f_R$ vs $\rho$ .....	88
Figure A.82: $Q$ vs $\eta$ .....	88
Figure A.83: $\beta$ vs $\eta^{0.5}$ .....	89
Figure A.84: $f_R$ vs $\rho$ (ex. dr.).....	89
Figure A.85: $f_R$ vs $\rho$ (liq. + sc, ex. dr.) .....	89
Figure A.86: $f_R$ vs $\rho$ (sc, ex. & af. dr.) .....	89
Figure A.87: $f_R$ vs $\rho$ (gas, ex. dr.).....	90
Figure A.88: $f_R$ vs $(\rho\eta)^{0.5}$ (ex. dr.).....	90
Figure A.89: $\beta$ vs $\eta^{0.5}$ (gas, ex. dr.) .....	90
Figure A.90: $P$ vs $\rho$ at $T=35$ °C.....	91
Figure A.91: $P$ vs $\rho$ at $T=45$ °C.....	92
Figure A.92: $P$ vs $\rho$ at $T=55$ °C.....	92

## Nomenclature

$f_R, f_{Rvac}$	resonance frequency, vacuum ~
$Q$	quality factor
$g$	resonance half-line width
$A_{max}$	maximum amplitude of oscillation
$FFT$	Fast Fourier Transform
$sc, SCF$	supercritical, supercritical fluid
$T, T_c$	temperature, critical temperature
$P, P_c$	pressure, critical pressure
$l, L$	length
$b, w$	width
$\Gamma, \Gamma_r, \Gamma_i$	hydrodynamic function, reel part of ~, imaginary part of ~
$Re$	Reynolds number
$AFM$	Atomic Force Microscopy
$\mu$	mass per unit length
$k$	stiffness
$\omega_R, \omega_{Rvac}$	radial (angular) resonance frequency, vacuum ~
$\rho$	density
$\rho_c$	density of cantilever
$\eta$	viscosity
$\beta$	damping parameter (coefficient)
$PSD$	Position Sensitive Detector
$E$	elasticity (Young's) modulus
$PZT$	piezoelectric
$LDV$	Laser Doppler Vibrometer

<i>MEMS</i>	Micro-electro-mechanical systems
$\lambda$	wavelength
<i>QCM</i>	Quartz Crystal Microbalance
<i>DI</i>	deionized
<i>RF</i>	Radio Frequency
<i>UV</i>	Ultraviolet
$m^*$	effective mass
$t$	thickness
$n$	beam geometric factor for $f_R$ calculation
$K_T$	isothermal compressibility
$\delta$	viscous skin depth

---

## Chapter 1

### 1 Introduction

#### 1.1 Overview

##### 1.1.1 Microcantilever Uses and Operation in Fluids

Micromechanical resonators have been extensively studied in recent years because of their potential for high-sensitive, low cost, compact device applications, such as mass sensors [1, 2], force sensors [3], viscometers and densitometers [4-12], chemical [2, 13, 14] and biological [1] sensors, explosive detectors [2], devices for mechanical characterization (e.g. for determining Young's modulus) [15] and for studying microscale phenomena (e.g. Knudsen effect) [16]. The dynamics of microcantilevers in fluids are important in the atomic force microscopy in biological buffers [5], naval architectural design [17] and the design of aforementioned viscometers and densitometers. In the operation of microcantilevers in a fluid, viscosity and density of the fluid are crucial parameters since the hydrodynamic length scale of the microcantilevers are comparable to the viscous penetration depth in the fluid [18].

The behavior of the microcantilevers immersed in fluids is mostly investigated by the changes in the resonance spectra, i.e. the shifts in the resonance frequency,  $f_R$ , and the quality factor,  $Q$ .  $f_R$  corresponds to the frequency at which the maximum amplitude of oscillation is achieved and the  $Q$  is the measure of sharpness of the resonance peak formulated as  $Q=f_R/2g$ , in which the frequencies  $f_{R+g}$  and  $f_{R-g}$  above and below  $f_R$  at which the amplitude is equal to  $A_{\max}/2^{1/2}$ , where  $A_{\max}$  is the maximum amplitude of oscillation achieved at  $f_R$  [10], as shown in Figure 1.1. The resonance spectra, i.e. amplitude versus frequency, can be extracted in a discrete manner by first a frequency

sweep and then a Lorentzian function fit that can be found elsewhere or in a continuous manner by Fast Fourier Transform (FFT) as power or thermal spectra.

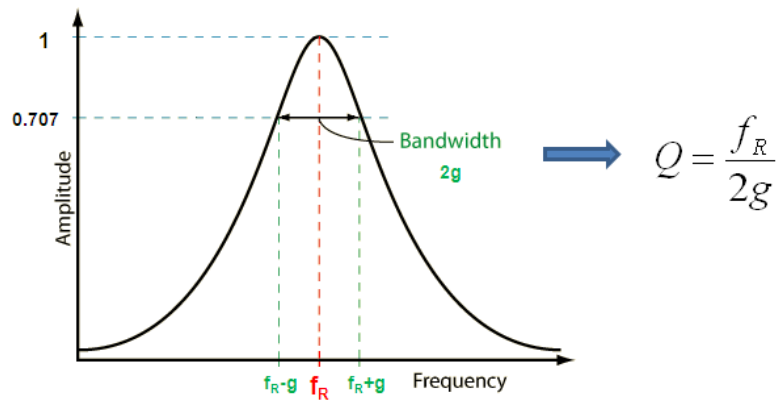


**Figure 1.1:** Representative Lorentzian fit to resonance spectrum

When a microcantilever is placed in a fluid (liquid or gas), the resonance frequency and quality factor decreases with increasing density and viscosity of the fluid. This phenomenon can be explained by two naive approximations where the effects of density and viscosity are assumed to be decoupled. First, the resonance frequency decreases with increasing density due to added mass, a phenomenon which is considered as inertial effect. Second, the quality factor decreases with increasing viscosity, i.e. the broadening of the resonance peaks, because of the shearing motion at the tip of the microcantilever which acts as a damping to the oscillations, another phenomenon which is known as dissipative effects [10]. However, in the actual case, the effects of density and viscosity on the dynamics of microcantilevers are coupled and the complex behavior is described by the hydrodynamic function by which the inertial and dissipative effects are quantified [4].

### 1.1.2 Supercritical CO<sub>2</sub> (scCO<sub>2</sub>)

A supercritical fluid is any substance at a temperature above its critical temperature ( $T_c$ ) and critical pressure ( $P_c$ ). The general pressure ( $P$ ) versus temperature ( $T$ ) diagram of supercritical fluids is shown in Figure 1.2 [19].

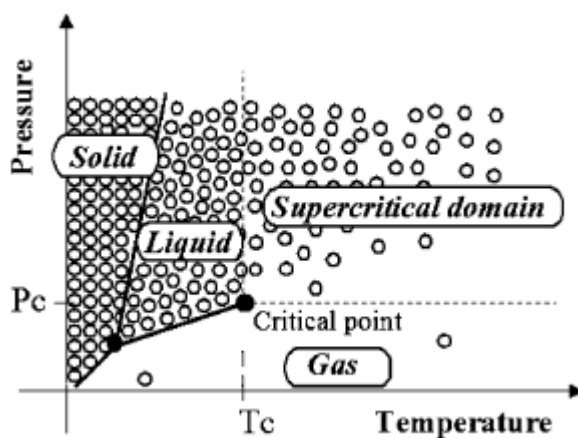


**Figure 1.2:** The pressure-temperature diagram of a pure substance

As seen in Figure 1.2, the phase boundaries separate the conventional phases such as solid, liquid and gas, however, there are no phase boundaries in the supercritical domain. This implies that only a homogeneous phase exists in the supercritical domain regardless of temperature and pressure.

The thermophysical properties of supercritical fluids such as density and viscosity can be altered in a very wide range of pressure and temperature. Moreover, these properties deviate dramatically in the proximity of critical point by infinitesimal pressure and temperature changes. This features makes supercritical fluids unique compared to conventional fluids. In Table 1.1, there is a comparison among thermophysical properties of the gases, liquid and supercritical fluids (SCFs).

**Table 1.1:** Comparison of thermophysical properties of gases, SCFs and liquids [20]

Physical property	Gases	Supercritical fluids	Liquids
Density (g/ml)	0.001	0.2–1.0	0.6–1.6
Dynamic viscosity (Pa·s)	$10^{-5}$	$10^{-4}$	$10^{-3}$
Diffusivity ( $\text{cm}^2/\text{s}$ )	$10^{-1}$	$10^{-3}$	$10^{-5}$

As seen in Table 1.1, the supercritical fluids have liquid-like density, gas-like viscosity and higher diffusivity than liquids.

## 1.2 Literature Review

Early theoretical studies by Sader et al. are aimed to correlate the resonance frequency and quality factor of cantilever beams to the density and viscosity of fluids in which they are immersed. The fundamental restrictions on the model developed are that the cantilever must be an isotropic linearly elastic solid, the amplitude of vibration must be small, the fluid must be incompressible, and the length of the beam ( $l$ ) must greatly exceed its nominal width ( $b$ ), i.e.  $l/b \geq 10$ . The flow around the cantilever is described by the hydrodynamic function ( $\Gamma$ ) which is a highly complex function of Reynolds number ( $Re$ ) and geometry of cross section of the beam.  $\Gamma$  is completely known for cylindrical cantilevers and it is derived for rectangular cantilevers by using a polynomial fit function in a  $Re$  range of  $[10^{-6}, 10^4]$  which is extracted from the asymptotic behavior of the cylindrical hydrodynamic function. The hydrodynamic function is then used to calculate the force in the equation of motion of the cantilevers which subsequently leads to determination of resonance frequency and quality factor of the cantilever in fluid [21].

The above theoretical results are experimentally validated by two studies of Sader et al. In the first study [4], the fundamental flexural mode frequency responses of arbitrarily

---

excited (thermal excitation) commercial (Park Scientific Instruments) single-crystal Si AFM microcantilevers of known linear mass density ( $\mu$ , i.e. mass per unit length of the beam) and stiffness ( $k$ ) in fluids like air, acetone,  $\text{CCl}_4$ , water and 1-butanol at 27 °C and 1 atm are found to agree well with the theoretical calculations. In the second study [6], a calibration procedure is described to determine the linear mass density and vacuum resonant frequency from a single measurement of the resonant frequency and quality factor of commercial microcantilevers in a reference fluid such as air. Moreover, a simple method for calculation of density and viscosity is developed. These equations are given below in Equations 1.1 and 1.2 as

$$\omega_R = \frac{\omega_{vac}}{\sqrt{1 + \frac{\pi\rho b^2}{4\mu} \Gamma_r(\omega_R)}} \quad (1.1)$$

$$Q = \frac{\frac{4\mu}{\pi\rho b^2} + \Gamma_r(\omega_R)}{\Gamma_i(\omega_R)} \quad (1.2)$$

where  $\Gamma_r$  and  $\Gamma_i$  are, respectively, the real and imaginary components of a hydrodynamic function  $\Gamma(\omega)$ ,  $\omega_{vac}$  and  $\omega_R$  are, respectively, radial resonant frequencies in vacuum and fluid for the 1<sup>st</sup> mode,  $\rho$  is the density of the fluid,  $b$  is the width of the cantilever and  $\mu$  is the mass per unit of the cantilever; for a rectangular cantilever  $\mu = \rho_c b h$ , where  $\rho_c$  is the density of the cantilever and  $h$  is the thickness.  $\Gamma_r$  corresponds to added mass due to fluid moving along with the cantilever during its motion and  $\Gamma_i$  to the viscous drag [7]. For a measured resonance spectra, the only unknowns in these equations are the density and viscosity of the fluid. Thus, the density and viscosity of the fluid can be achieved by the simultaneous numeric solution of these equations. In addition, experiments in gases like



---

air, CO<sub>2</sub>, Ar, He and H<sub>2</sub> and liquids like acetone, CCl<sub>4</sub>, water and 1-butanol at 27 °C and 1 atm indicate very high accuracy in both density and viscosity measurement.

The experimental results of Sader et al. [6] are used by Schilowitz et al. [5] to develop a simple method which is based on the idea that damping coefficient ( $\beta$ ) squared must be linearly related to the viscosity ( $\eta$ ) for which the derivation is presented in an earlier paper by the same group [22]. The Sader's results are shown to fit well and a simple calibration procedure is explained. For the calibration, resonance spectra for commercial (Veeco) piezoelectrically actuated Si microcantilevers are measured optically (Position Sensitive Detector, PSD) in two fluids of known viscosities (for example air at room conditions and a viscous hydrocarbon) to have two calibration points in  $\beta$ - $\eta^{0.5}$  plane covering a wide range of viscosity. Good results in viscosity calculation for hexadecane and dodecane at room conditions are obtained in the experiments. It is also shown that the internal friction damping term is negligible for high viscous liquids as well as low viscous gases since the overall damping is totally due to fluid friction.

Goodwin et al. study the density and viscosity of fluids encountered mainly in petroleum industry [10]. The aim is to fabricate densimeter/viscometer for the simultaneous measurement of density and viscosity that can operate temperatures below 473 K and pressures up to 200 MPa and provide densities and viscosities with uncertainties of 1% and 10%, respectively. Experiments using a singly clamped Si plate fabricated by MEMS technology are conducted in methylbenzene, octane, water, 1-propene, 1,1,2,3,3,3-hexafluoro-oxidized-polyimide, polymethylsiloxane, nitrogen, argon, methane between temperatures 313 K and 423 K and pressures in the range 0.1 MPa and 68 MPa utilizing a stirred pressure chamber with temperature control [10, 23-25]. The phases at these conditions are gases and liquids where the density covers the range 11 kg/m<sup>3</sup> to 1834 kg/m<sup>3</sup> and the viscosity varies from 11  $\mu$ Pa·s to 275 mPa·s. The actuation is electromagnetic actuation and the detection is provided by strain gauges. The calibration is

based on the measurements in gases at low pressure methylbenzene and argon. A model is developed which decouples correlations for density and viscosity so that the density is determined solely from the resonance frequency and another independent equation is introduced for the product of density and viscosity. The formulations are

$$\rho_f = \frac{C_1 E v_n^5 d^3}{24(1 - \sigma^2) a^5 (2\pi f_{r,f})^2} - \frac{C_2 \rho_s d v_n}{2a} \quad (1.3)$$

$$\eta_f = \frac{C_3}{\rho_f f_{r,f}^3} \left( \frac{2g_f}{f_{r,f}} - \frac{2g_{(P=0)}}{f_{r(P=0)}} \right)^2 \quad (1.4)$$

where  $\rho_f$  is the fluid density,  $C_1$ ,  $C_2$  and  $C_3$  are parameters for plate material properties extracted from calibration in the absence of direct measurement of Young's modulus  $E$ , Poisson's ratio  $\sigma$ , plate material density  $\rho_s$ ,  $v_n$  is the eigenvalue of the  $n^{\text{th}}$  mode (e.g.,  $v_1=3.927$ ),  $d$  is the plate thickness,  $a$  is the plate length,  $f_{r,f}$  is the resonance frequency of the plate immersed in fluid,  $\eta_f$  is the fluid viscosity,  $g_f$  is the resonance half-line width (see Figure 1.1),  $g_{(P=0)}$  is vacuum resonance half-line width and  $f_{r(P=0)}$  is the resonance frequency in vacuum. In principle, it is stated that the formulations are based on naïve approximations which assume inviscid flow of an incompressible Newtonian fluid. Despite these simplifications, the average errors for density and viscosity calculations are 2% and 30%, respectively [24].

Many other studies are also aimed to measure the density and viscosity using microcantilevers. Shih et al. fabricated a piezoelectric (PZT) coated stainless steel cantilever and performed experiments in water, glycerol and water-glycerol mixtures. The actuation is provided by the driving electrode coating while the detection is provided by the piezoelectric layer. It is seen that the resonance frequency and quality factor decreased

---

with increasing glycerol content. A model to predict the density and viscosity of the fluid using the resonance frequency and quality factor is derived based on an oscillating sphere-spring-intrinsic (cantilever) damper system as described by Landau and Lifshitz [26]. Measurement results indicate that the model predicts the density and viscosity in a good fashion [27]. Belmiloud et al. focus on viscometry in the range of 0.02 Pa·s and 20 Pa·s using metal-coated microcantilevers where the actuation method is electromagnetic and the detection method is optical. To widen the measurement range, the entire frequency spectrum of a vibrating microcantilever is used instead of focusing to the shifts in resonance frequency and quality factors. This is based on the idea that the response spectrum is unique for a given geometry and fluid viscosity. Experiments at room temperature and pressure using Newtonian fluids in a wide range of viscosities as well as Maxwellian fluids like EHDT-silicone gel indicate that the microcantilevers can be used as microrheometers that can measure viscosity, density also elasticity [28]. Both ends fixed aluminum-coated Si microcantilevers are used by Etchart et al. as density-viscosity sensors in liquids like pentane and dichloromethane where the density changes between 620 kg/m<sup>3</sup> and 1620 kg/m<sup>3</sup> and viscosity varies in the range from  $2.2 \times 10^{-4}$  Pa·s to 0.11 Pa·s [29]. The cantilevers are actuated electromagnetically and the deflections are detected either by strain gauges or Laser Doppler vibrometer (LDV). Previously mentioned sphere in liquid-spring-damper system of Landau and Lifshitz is used to derive equations for density and viscosity calculation. Errors up to 40 % are encountered showing that the model must be modified. It is also presented that the resonant frequency and quality factor measurements are not strongly affected by the fluid flow up to about 1 ml/min.

The theory behind frequency response of microcantilevers in compressible fluids is a new area in MEMS research which can expand the range of functionality of the devices produced. Apart from the theoretical studies published by Sader et al. [18, 30], there are no experimental validations at the moment. In these studies, it is shown that compressibility

---

becomes increasingly important as the mode number rises. In general the flow around the cantilever can be considered as incompressible provided that acoustic wavelength, i.e.  $\lambda_{sound} \approx 1.425c / [(2n - 1)^2 f_{vac,1}]$  where  $c$  is the speed of sound,  $n$  is the mode number and  $f_{vac,1}$  is the vacuum resonant frequency of 1<sup>st</sup> mode, greatly exceeds the dominant length scale of the flow. For practical cantilevers with high length/width and width/thickness ratios operating at low mode numbers, the flow is approximately incompressible, two dimensional and its dominant length scale is the beam width. As the mode number or the compressibility increases the acoustic wavelength eventually becomes comparable the spatial wavelength of the beam. The point at which these wavelengths become equal is called the coincidence point where energy starts to be carried away in the form of sound waves.

In the literature, there is no study related to the operation of microcantilevers in supercritical CO<sub>2</sub> except the work of Otake et al. [31] carried out by using Quartz Crystal Microbalance (QCM). The experiments are performed at pressures up to 15 MPa at 40 °C with He, N<sub>2</sub> and CO<sub>2</sub> using silver-coated QCM. A large frequency decrease is observed for CO<sub>2</sub> near the critical point. This is attributed to the rapid increase of the weight of physically adsorbed CO<sub>2</sub> described by Freundlich isotherm.

### 1.3 Statement of the Problem

As stated in the literature review section, there is not any previous study investigating the frequency response of microcantilevers in supercritical CO<sub>2</sub>. In this study, we try to investigate the resonance spectra shifts, i.e. resonance frequency and quality factor changes, of microcantilevers operating in pressurized CO<sub>2</sub> upon the density and viscosity changes. The ultimate goal is to achieve a sensor that will detect both density and viscosity of fluids in a wide pressure and temperature range. We fabricate multilayered

---

(Cr, Au and Ni layers from bottom to top), singly clamped microcantilevers with dimensions of width 20  $\mu\text{m}$ , thickness 1  $\mu\text{m}$  and lengths 200  $\mu\text{m}$ , 225  $\mu\text{m}$  and 250  $\mu\text{m}$ . The experimental conditions are pressures from 1 atm to 200 atm at temperatures of 25  $^{\circ}\text{C}$ , 35  $^{\circ}\text{C}$ , 45  $^{\circ}\text{C}$  and 55  $^{\circ}\text{C}$ . The actuation method is AC electromagnetic actuation provided by electromagnetic coil and the detection method is optical detection using Laser Doppler Vibrometer (LDV).

#### **1.4 Outline**

This thesis is composed of five chapters.

In Chapter 2, the device fabrication processes are explained in steps with detail, problems encountered during fabrication, e.g. white precipitate occurring after Au etching, and their ways of elimination are discussed.

In Chapter 3, the experimental setup is presented with working principles of some equipment like LDV, the measurement procedure at high pressures is given and a representative Lorentzian fit to acquired data is shown.

In Chapter 4, the results obtained in air and  $\text{CO}_2$  are presented in graphical form, bubbling observed at phase transition is shown and relationships between the resonance spectra and thermophysical data are investigated, e.g. resonance frequency versus density and damping parameter versus viscosity.

In Chapter 5, the findings in this study are summarized, the methods to eliminate experimental errors and increase the efficiency of experiments are discussed and the future work with suggestions is presented.

---

## Chapter 2

### 2 Device Fabrication

#### 2.1 Fabrication Flow

The microcantilevers used in this study are produced using conventional microfabrication methods, previously explained by Ocakli [32], Ozturk [33] and Kilic [34]. The fabrication flow is shown in Figure 2.1. The steps of fabrication are namely Si wafer preparation, seed layer (Cr & Au) layer formation, mold-pattern preparation (UV Photolithography), pattern development, slicing wafer into dice, structural layer formation (Ni electroplating), photoresist removal, wet-etching of Au and Cr layers and wet-etching of Si substrate. These steps will be explained in detail in the remainder of this chapter.

##### 2.1.1 Substrate Preparation

Due to small dimensions studied, removal of dust and residual particles is an initial and important step in the fabrication. Therefore, Si wafer of thickness  $525 \pm 25 \mu\text{m}$  and of resistivity  $0.1\text{-}0.5 \Omega\text{cm}$  is cleaned using acetone, isopropyl alcohol, deionized (DI) water and dried using  $\text{N}_2$ .

##### 2.1.2 Seed Layer Formation

The structural layer is formed by electroplating which requires a high electrically conductive substrate surface. To increase the conductivity, a thin layer of Au is eminent.

However, adhesion in Au-Si interface is not strong and an adhesion promoter, Cr layer, is needed. Utilizing a RF-Magnetron sputtering system, Cr layer of 10-20 nm and Au layer of 100-120 nm are deposited on Si wafer.

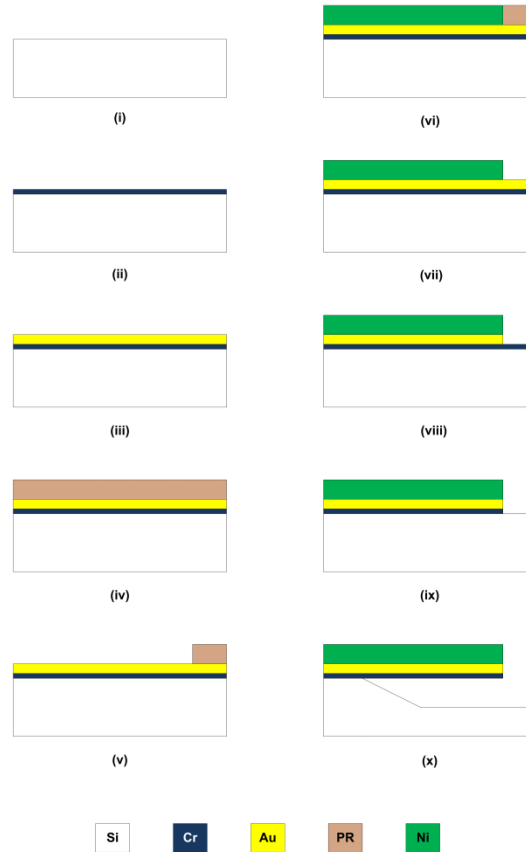


**Figure 2.1:** Fabrication flow: (i) Standard cleaning of  $\langle 100 \rangle$   $525 \pm 25$   $\mu\text{m}$  thick 4" Si wafer (ii) Sputtering of 20 nm layer of Cr and (iii) 120 nm Au by RF-Magnetron (iv) Spin-coating with AZ 5412 photoresist and soft-baking (v) UV photolithography and the pattern development by AZ 400K remover (vi) The wafer is sliced into dice and Ni electroplating is conducted for each die (vii) Removal of photoresist by AZ 100 remover (viii) Au layer etching using Transene TFAC Ni-selective Au etchant (ix) Cr layer etching using MicroChrome TFE Cr etchant (x) Si substrate is wet etched using KOH solution and the free-standing multilayered cantilevers are achieved.

### 2.1.3 Mold-pattern preparation

UV Photolithography is used to define the mold-pattern that is to be filled as microcantilever structures. First, a UV-sensitive mold material, photoresist solution (AZ 5412), is spin-coated on the wafer. Next, the wafer is soft-baked at 110 °C for 10 minutes to have better adhesion and remove excess solvent. Then, UV light is exposed on the wafer through the mask that is drawn using L-Edit software. Last, the openings for microcantilever material electroplating are obtained by dissolving the exposed regions of photoresist using AZ 400K developer. The unexposed regions are soluble since there is no cross-linking initiated in the polymeric photoresist material upon exposure. This kind of photoresists is classified as positive, and other type is negative photoresist in which the intermolecular bonds are strengthened if exposed. Figure 2.2 explains the difference in patterns formed using positive and negative photoresists.

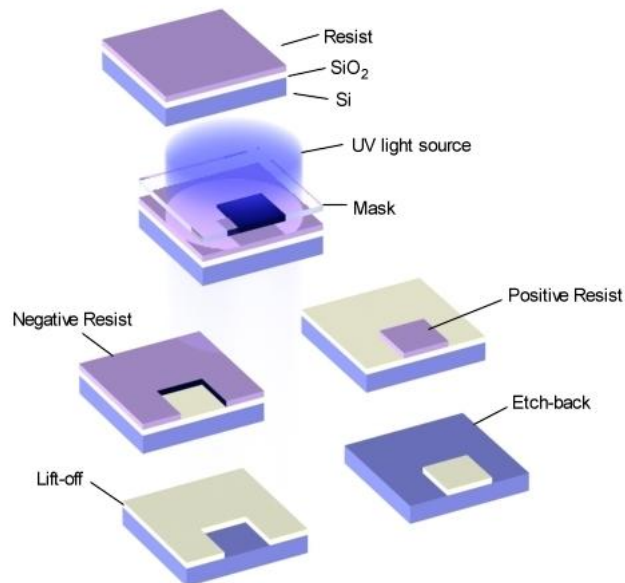


**Figure 2.2:** The demonstration of patterns formed using positive and negative photoresists [35]



---

The critical issues that specify the quality of pattern definition are the thickness of the photoresist, exposure time, development time and rate. These parameters are improved by study of Ocakli where a full recipe is given [32]. For example, it is proven that a minimum photoresist thickness of 1.4-1.6  $\mu\text{m}$  is needed in order to obtain 1  $\mu\text{m}$  thick microcantilevers.

#### 2.1.4 Structural layer formation

After the pattern development, the whole wafer is sliced into dice and structural layer is formed via Ni electroplating over Au surface on each die. Ni is used as the structural layer due to its high resistance to oxidative and corrosive agents and ferromagnetic behavior, i.e. availability to be magnetically actuated.

Electroplating is an electrochemical reaction in which the cathode is the die with a conducting layer and the photoresist on it, the anode is the Ni bar and the analyte is the nickel sulfamate solution consisting of 40 g/l  $\text{H}_3\text{BO}_3$ , 600 g/l  $\text{Ni}(\text{SO}_3\text{NH}_2)_2 \cdot 4\text{H}_2\text{O}$  and 10g/l  $\text{NiCl}_2 \cdot 6\text{H}_2\text{O}$ . The process is shown in Figure 2.3.

When the power is turned on, the positive ions in the solution are attracted to the cathode, and the  $\text{Ni}^{2+}$  ions that reach the cathode gain electrons and form a Ni layer on the cathode. Simultaneously, another reaction occurs at the anode, to produce ions and electrons for power supply.

For electroplating, nickel sulfamate solutions are preferred because internal stress in the Ni deposits is very low preventing the stiction problem encountered after Si substrate etching. Boric acid in the solution buffers pH variations and nickel chloride increases the conductivity of the analyte. Since an insoluble anode is used, nickel sulfamate is the source of nickel serving as well as conductive electrolyte for carrying nickel ions from anode to

cathode. The pH of the solution is about 4.5 and must be kept at that value by adding nickel carbamate.

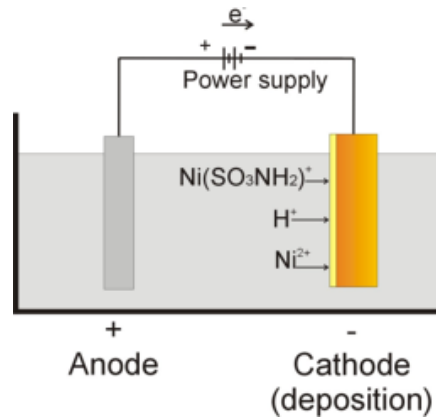


**Figure 2.3:** Schematic representation of electroplating process [36]

The crucial parameters for controlling the thickness and surface roughness of electroplating are the current density, temperature and duration of the reaction. The temperature is kept constant at 45 °C during electroplating to achieve the highest Young's modulus according to Luo et al. [37]. The electrical contact on the die is established along the four edges of the die, as shown in Figure 2.4, and the solution is continuously stirred during the reaction to achieve a homogeneous electroplating.

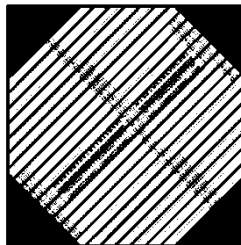


**Figure 2.4:** The mask drawing of a die showing the four edges for electrical connection during electroplating

---

The current density is held at  $10 \text{ mA/cm}^2$  instead of  $40 \text{ mA/cm}^2$  used in the work of Kilic [34] to eliminate internal stress gradient along the length of the cantilever which could possibly cause stiction problem. This decrease in current density increased the duration for  $0.85\text{-}0.95 \text{ }\mu\text{m}$  thick electrodeposition to 25 minutes compared to previous work by Ocakli [32].

### 2.1.5 Wet-etching of Au and Cr layers

After the microcantilevers are formed by electroplating, photoresist is removed using AZ 100 remover. In order to release the cantilevers to be actuated, the Au and Cr layers are etched. Au layer is etched for 1-1.2 minutes using 1:3 Transene TFAC Ni-selective Au etchant-water solution. Au layer is time-etched in order to preserve the Au layer underneath. Then, Cr layer is etched for 30-45 seconds using 1:3 MicroChrome TFE Cr etchant-water solution. In previous works of Ocakli and Kilic [32, 34], the Cr layer underneath is completely removed, however in this study, Cr layer is also preserved. Because it is experimentally validated that wider and longer microcantilevers can be produced only by preserving the underneath Au and Cr layers.

Next, cantilevers are completely released by anisotropic etching of Si substrate using 45% KOH-water solution at  $55 \text{ }^\circ\text{C}$  for 23 hours resulting in an etch depth of  $150 \text{ }\mu\text{m}$ . This depth is sufficient to eliminate the squeezed film damping effects [38]. The temperature and concentration are optimized to overcome the stiction problem and achieve minimum surface roughness required for optical detection. Unlike early works by Ocakli and Kilic [32, 34], a higher concentration (45% to 35%) and a lower temperature ( $55 \text{ }^\circ\text{C}$  to  $70\text{-}65 \text{ }^\circ\text{C}$ ) are employed in Si etch. This is because the microcantilever widths and lengths are larger in this study increasing the possibility of stiction. Comparing the etch times, the

---

total etching time is increased from 30-60 minutes to 23 hours implying the dominance of energetic character of the reaction over the concentration of the solute.

### 2.1.6 Final cleaning

A common practice in the microfabrication is to find ways to eliminate the stiction problem during the drying of the die after the Si etch. One of them is through the solvent exchange of water by acetone. The idea is that the surface stress of the water is higher than that of acetone. For that reason, it is more likely for cantilevers to stick to Si substrate during the evaporation of water compared to evaporation of acetone. The solvent exchange is done through first rinsing of the die in water for 10 minutes, next adding acetone to water for 50 % acetone-water solution and further waiting for 10 minutes, last rinsing of the die in acetone for 10 minutes. This procedure is now currently employed in the practice of microfabrication orientation.

The die must be RCA1 cleaned to remove any organic residues. RCA1 cleaning involves first the treatment of the dice with a 2:3:10  $\text{NH}_4\text{OH}:\text{H}_2\text{O}_2:\text{DI}$  water at 70 °C for 10 minutes, next rinsing of the die with DI water and last drying the die on a heater for a few seconds.

After this step, the microcantilevers are ready for measurements. Figure 2.5 shows a portion of fabricated microcantilevers.

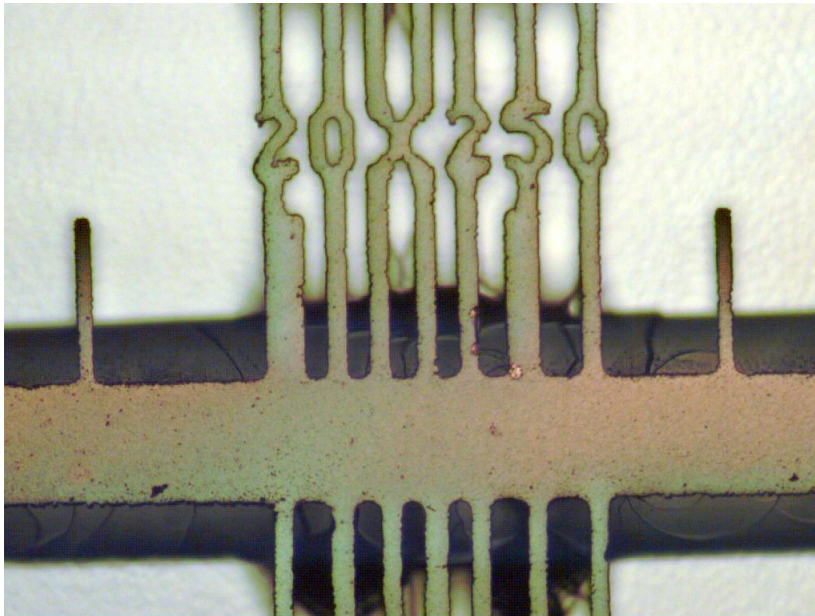


**Figure 2.5:** A portion of fabricated microcantilevers which are ready for measurement

## 2.2 Encountered problems

The fabrication is done using recipes given by Ocakli and Ozturk [32, 33], however some problems were encountered and these problems are solved accordingly.

### 2.2.1 White precipitate occurring after Au etchant

When using the gold etchant (formulation code GE8148), a white precipitate has been observed and when the precipitate has been removed, damage (i.e. corrosion) of the underlying surface of the structural material (i.e. nickel) has been observed as shown in Figure 2.6.

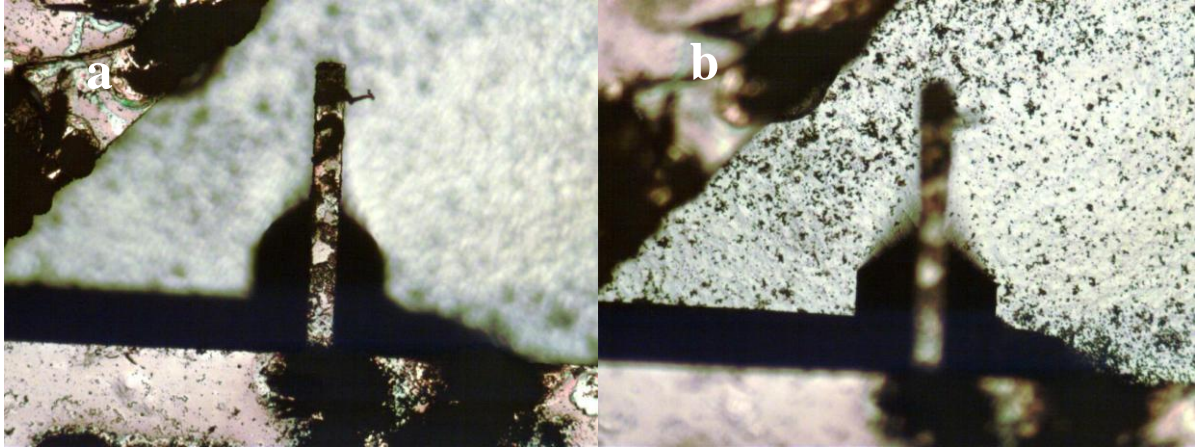


**Figure 2.6:** White precipitate occurred after gold etching. a. Cantilever focused b. Si substrate focused

There are some explanations for the occurrence of the white precipitate. The primary source may be the reaction between the remnants of Cr layer that interact with the etching solution to form a precipitate  $\text{CrI}_2$ . The secondary source may be the reaction between the gold and the etchant to form  $\text{AuI}$ . The corrosion may come about from a localized difference in concentration of Au etchant [39].

In order to eliminate forming of the white precipitate, some developments are suggested. The temperature of the gold etchant solution is increased to  $35\text{ }^\circ\text{C}$  from room temperature and the stirring rate is increased during the etching. High temperature increased the diffusion rate of the etchant and the etch products in the gap between the cantilever bottom surface and Si substrate and a high mixing rate prevented the overconcentration of the etchant. These improvements are observed to work.

### 2.2.2 Over-etching of Si substrate

Since the lengths and widths of the microcantilevers used in this study are larger than those of previous works by Ocakli and Kilic [32, 34], Si substrate must be etched much deeper to release the cantilevers. It is seen that 150  $\mu\text{m}$  deep Si etch using 45% KOH-water solution takes 23 hours at 55  $^{\circ}\text{C}$ .

For one run, the temperature is not set by the heater due to some error and after the overnight process, it is seen that Si substrate is etched almost completely remaining a frame of anchor and cantilevers as seen in Figure 2.7c.

Apart from the implication of the importance of temperature control during Si etch, the back of the remaining frame gives insight about how the Au and Cr etchants behave. In Figure 2.7a, the pattern in the label shows that the edges are etched uniformly implying the accuracy of the recipes employed.

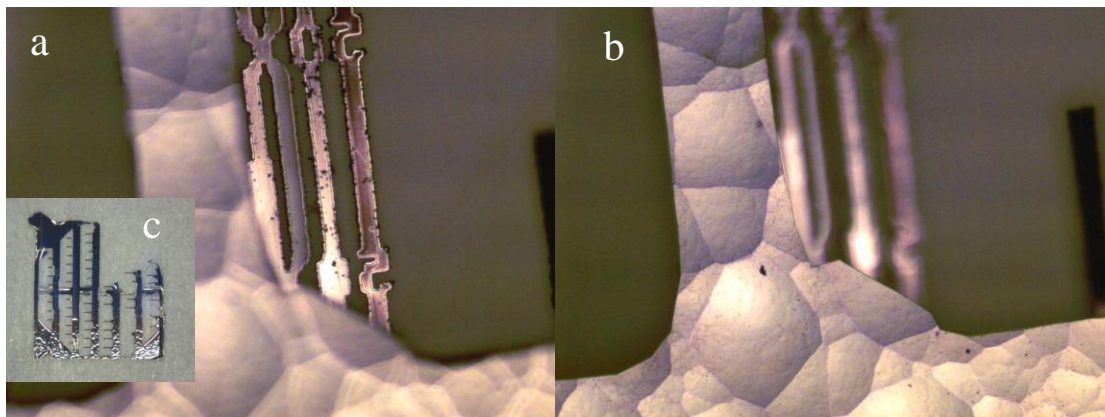


**Figure 2.7:** Over-Si etched die (back view) a. Label focused b. Si substrate focused c. The die

---

## Chapter 3

### 3 Measurement Setup and Procedure

#### 3.1 Interferometry and Measurement Setup

The resonance frequency and quality factor of the microcantilevers are measured using Laser Doppler Vibrometer (LDV, Polytec OFV-2500 with bandwidth of 0.5 Hz - 1.5 MHz ). LDV is a non-contact, interferometry-based velocity and displacement measuring technique used to detect vibrations. Laser Doppler Vibrometry uses the Doppler effect to measure vibrations. When light is scattered from an oscillating object, its frequency changes. Within the vibrometer a high precision interferometer detects the minute frequency shifts of the backscattered laser light. To achieve this, the interferometer splits the light into two parts: the so-called reference beam is pointed directly to the photodetector, while the measurement beam is focused on the test object. The moving object scatters the light back changing its frequency and phase. The characteristics of the motion are completely contained in the backscattered light. The superposition of this light and the reference beam creates a modulated detector output signal revealing the Doppler shift in frequency. Signal processing and analysis provides the vibrational velocity and displacement of the test object. The interferometry principle is shown schematically in Figure 3.1.



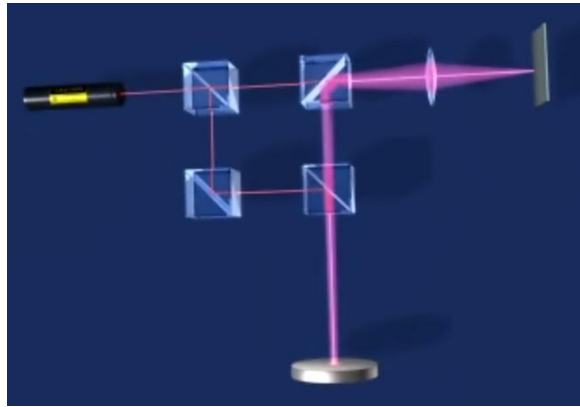


**Figure 3.1:** LDV interferometry [40]

The schematic description of the experimental setup is shown in Figure 3.2.

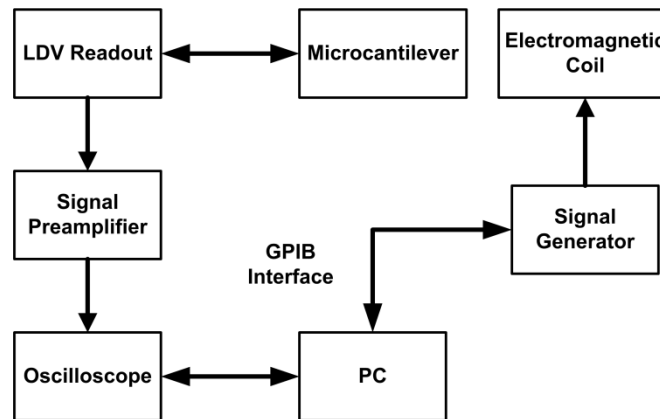


**Figure 3.2:** The schematic description of the measurement setup

In order to eliminate mechanical noises, a vibration-free tabletop is prepared by using 4 Thorlabs PWA071 Passive Isolation Mounts placed under a granite block. On top of the block, the Polytech OFV-2500 LDV and a 50 ml TharSFC 05424-4 view cell are fixed on a 30 cm x 45 cm breadboard. The LDV built-in camera is connected to a 15" screen CRT TV. Pure CO<sub>2</sub> is supplied from Messer Aligaz with an indicated purity of

99.9% by volume and pumped using a TELEDYNE ISCO D Series Pump. A custom-made Teflon housing that fits the view cell is used to stabilize the MCs and the electromagnetic actuator which consisted of a coil made from Cu wire, as shown in Figure 3.3.

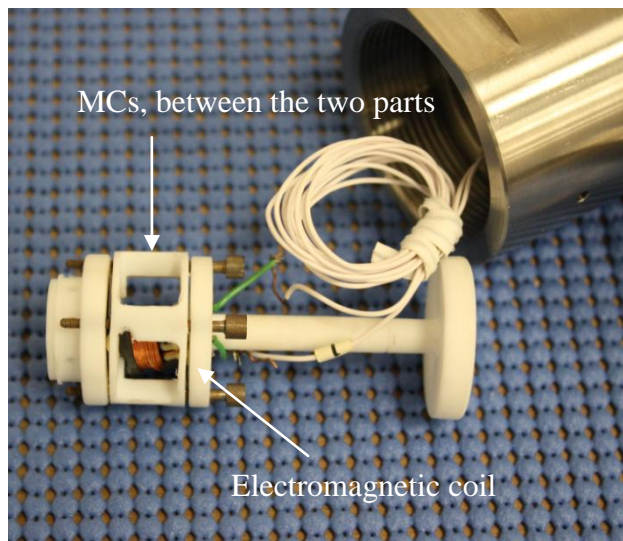


**Figure 3.3:** Custom-made Teflon housing for immobilization of MCs and electromagnetic coil

The electrical connection for actuation in the pressure vessel is achieved by using insulated CONAX Technologies TG24T gland assemblies. All valves and connections were Swagelok. Throughout the operation, no flow is allowed and the temperature in the vessel is held constant by circulating fluid through tubing wrapped around the vessel using a Polyscience recirculator. AC actuation of 10 V is provided by Agilent 33220A Function Generator and the resonance spectrum obtained from LDV is amplified and filtered by Stanford Research SR560 Preamplifier and visualized by Tektronix TDS 654C Oscilloscope. The operation of the signal generator and the data acquisition from the oscilloscope are achieved using Instrument Control Toolbox in MATLAB via Keithley KUSB-488A GPIB-USB interface.

The overall experimental setup is shown in Figure 3.4.

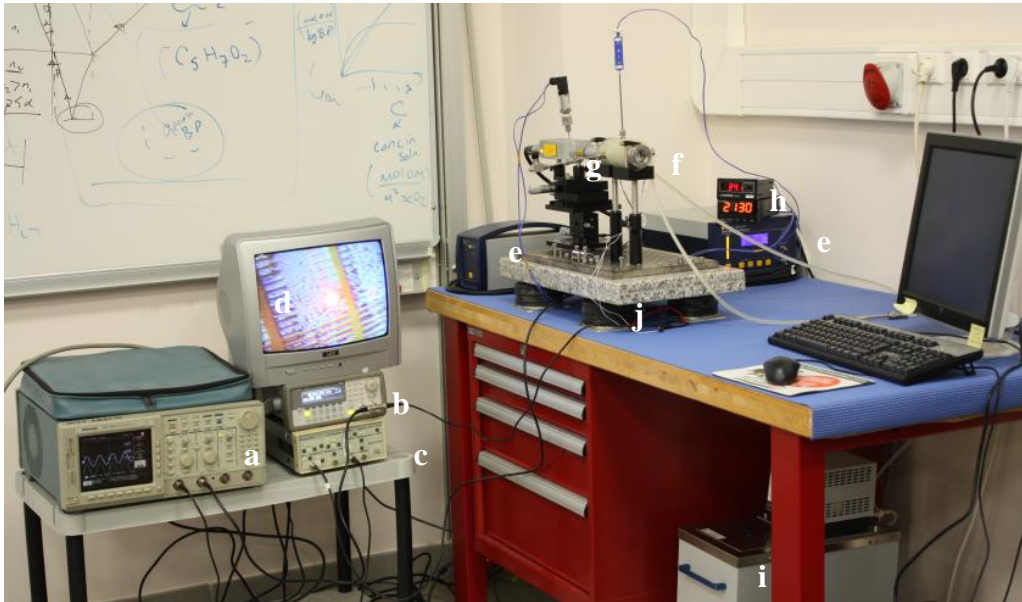


**Figure 3.4:** The experimental setup. (a) Oscilloscope (b) Signal Generator (c) Preamplifier (d) CRT TV (e) LDV control unit (f) Pressure Vessel (g) LDV laser unit (h) Temperature and Pressure Indicators (i) Recirculator (j) Passive vibration isolation pads

The behavior of the microcantilevers immersed in fluids is mostly investigated by the shifts in the resonance frequency,  $f_R$ , and the quality factor,  $Q$ .  $f_R$  corresponds to the frequency at which the maximum amplitude of oscillation is achieved and the  $Q$  is the measure of sharpness of the resonance peak formulated as  $Q=f_R/2g$ , in which the frequencies  $f_{R+g}$  and  $f_{R-g}$  above and below  $f_R$  at which the amplitude is equal to  $A_{\max}/2^{1/2}$ , where  $A_{\max}$  is the maximum amplitude of oscillation achieved at  $f_R$ . The amplitude versus frequency data can be extracted in a discrete manner by first a frequency sweep, recording peak-to-peak voltage data and then a Lorentzian function fit that can be found elsewhere or in a continuous manner by Fast Fourier Transform (FFT) as power or thermal spectra. A

representative Lorentzian function fit to the resonance spectra of the fundamental flexural mode of vibration with normalized amplitude using MATLAB can be seen in Figure 3.5.

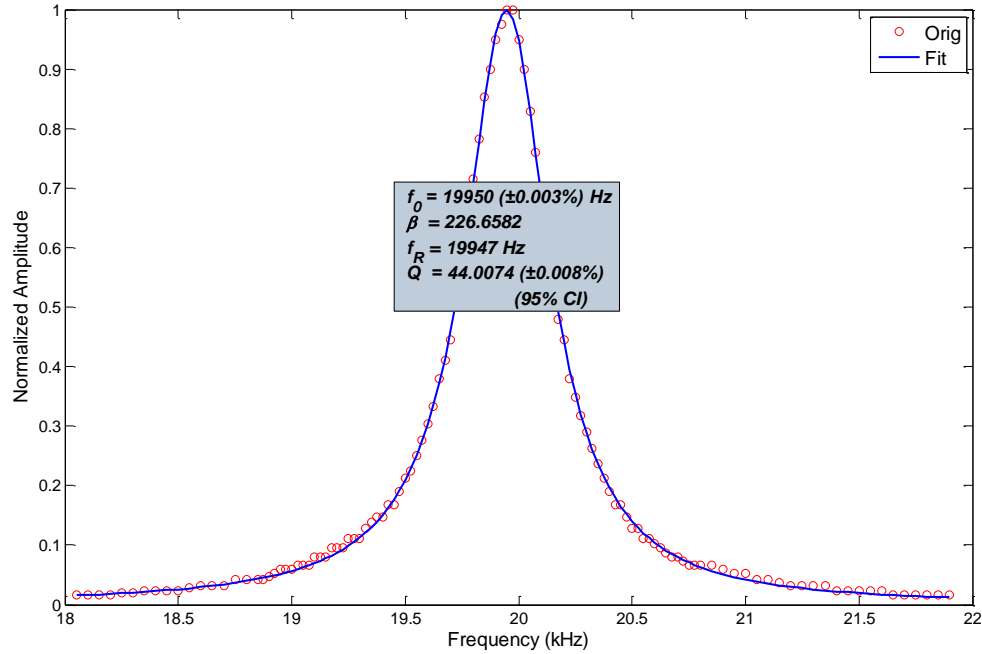


**Figure 3.5:** A sample response curve and the Lorentzian fit with the parameters vacuum resonance frequency  $f_0$ , damping parameter  $\beta$ , resonance frequency  $f_R$  and quality factor  $Q$

### 3.2 Experimental Conditions

In this study, three types of cantilevers of width  $20 \mu\text{m}$  and lengths ( $L$ )  $200 \mu\text{m}$ ,  $225 \mu\text{m}$  and  $250 \mu\text{m}$  are used. The experimental conditions, i.e. temperature ( $T$ ) and pressure ( $P$ ), are such given in the following tables.

---

### 3.2.1 Measurements in Air

Measurements in air are done to get the almost-vacuum frequencies of the microcantilevers.

**Table 3.1:** Pressure and temperature for measurements in air

<b>P=1 atm</b>	<b>T (°C)</b>
	25
	35
	45
	55

### 3.2.2 Measurements in Pressurized CO<sub>2</sub>

#### 3.2.2.1 Measurements at room temperature:

During the measurements at room temperature, temperature is not controlled. Despite the absence of temperature control, the deviation in temperature is small.

**Table 3.2:** Measurements in room temperature in pressurized CO<sub>2</sub>

L=200 $\mu\text{m}$		L=225 $\mu\text{m}$		L=250 $\mu\text{m}$	
P (atm)	T ( $^{\circ}\text{C}$ )	P (atm)	T ( $^{\circ}\text{C}$ )	P (atm)	T ( $^{\circ}\text{C}$ )
8.84	26.9	8.91	26.9	8.98	26.9
15.71	26.6	15.65	26.5	15.51	26.4
22.18	26.1	22.24	26.2	22.38	26.3
29.25	26.0	29.18	25.9	29.12	25.7
48.50	25.4	48.57	25.4	48.71	25.6
64.76	25.5	64.56	25.3	64.56	25.3
72.86	25.6	72.72	25.6	72.93	25.7
80.75	25.2	81.02	25.2	81.02	25.2
92.52	25.3	92.52	25.3	92.31	25.2
115.44	25.6	116.12	25.6	115.10	25.5
137.89	26.1	138.57	26.1	139.12	26.3

**3.2.2.2 Measurements at 35  $^{\circ}\text{C}$ :****Table 3.3:** Measurements at 35  $^{\circ}\text{C}$  in pressurized CO<sub>2</sub>

L=200 $\mu\text{m}$		L=225 $\mu\text{m}$		L=250 $\mu\text{m}$	
P (atm)	T ( $^{\circ}\text{C}$ )	P (atm)	T ( $^{\circ}\text{C}$ )	P (atm)	T ( $^{\circ}\text{C}$ )
8.50	35.0	8.44	34.9	8.44	34.9
14.97	35.0	14.90	35.0	14.83	35.0
21.97	34.8	21.97	34.8	21.84	35.0
28.78	35.0	28.57	35.0	28.37	35.0
49.46	35.0	49.52	35.0	49.39	35.0
68.84	35.1	68.84	35.1	68.84	35.1
80.68	35.2	80.68	35.2	80.54	35.0
91.22	35.2	91.36	35.2	91.22	35.2
107.89	35.2	107.76	35.1	107.55	35.1
125.31	35.2	125.58	35.2	126.26	35.2
144.49	35.1	144.83	35.1	144.69	35.0
161.09	35.2	161.36	35.2	163.33	35.1

### 3.2.2.3 Measurements at 45 °C:

**Table 3.4:** Measurements at 45 °C in pressurized CO<sub>2</sub>

L=200 μm		L=225 μm		L=250 μm	
P (atm)	T (°C)	P (atm)	T (°C)	P (atm)	T (°C)
9.12	45.1	9.05	45.0	8.91	45.0
29.18	44.9	29.18	44.9	29.18	44.9
49.39	44.8	49.39	45.0	49.39	45.0
69.73	45.2	69.73	45.2	69.73	45.2
83.40	45.0	83.33	45.0	83.61	45.0
98.78	45.1	98.78	45.1	98.71	45.1
110.07	45.0	110.07	44.9	110.34	45.1
133.40	45.4	132.93	45.3	132.52	45.2
152.65	45.1	152.86	45.1	153.88	45.1
176.26	45.2	173.27	45.0	178.10	45.1
202.18	45.1	202.18	45.1	203.40	45.2

### 3.2.2.4 Measurements at 55 °C:

**Table 3.5:** Measurements at 55 °C in pressurized CO<sub>2</sub>

L=200 μm		L=225 μm		L=250 μm	
P (atm)	T (°C)	P (atm)	T (°C)	P (atm)	T (°C)
9.86	55.0	9.80	54.9	9.73	54.9
29.93	55.1	29.93	55.1	29.86	55.2
49.73	55.0	49.66	54.9	49.66	54.9
69.59	55.1	69.59	55.1	69.46	55.1
86.46	54.9	86.46	54.9	86.39	55.0
104.56	55.2	104.42	55.1	104.42	55.1
124.42	54.9	124.42	54.9	124.42	54.9
145.31	55.1	145.31	55.1	145.51	55.1
170.14	55.1	169.86	55.1	169.66	55.0
192.93	55.1	192.79	55.1	192.86	55.0
214.56	55.0	215.03	55.0	215.37	54.9

---

## Chapter 4

### 4 Results and Discussion

#### 4.1 Measurements in Air at P=1 atm

The density and viscosity of air at P=1 atm is given in Table 4.1.

**Table 4.1:** Density and viscosity values at P=1 atm in air

T (°C)	$\rho$ (kg/m <sup>3</sup> )	$\eta$ (kg/ms)
25	1.19	1.81E-05
35	1.15	1.86E-05
45	1.11	1.90E-05
55	1.08	1.95E-05

The resonance spectra results in air is given in Table 4.2.

**Table 4.2:** Resonance spectra obtained in air

L=200 $\mu\text{m}$			L=225 $\mu\text{m}$			L=250 $\mu\text{m}$		
$f_R$ (Hz)	Q	$\beta$	$f_R$ (Hz)	Q	$\beta$	$f_R$ (Hz)	Q	$\beta$
20567	113.16	90.87	15793	96.55	81.78	13554	85.39	79.36
20501	94.41	108.57	15745	92.43	85.17	13518	82.01	82.42
20429	93.63	109.10	15701	87.87	89.34	13480	75.89	88.81
20360	96.69	105.29	15652	83.42	93.82	13441	71.39	94.14

The results are analyzed graphically.



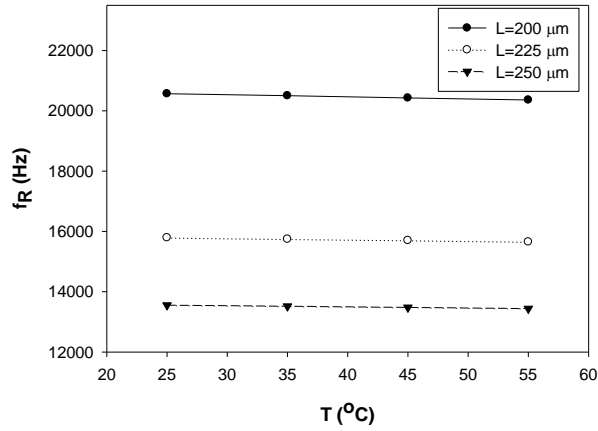


Figure 4.1:  $f_R$  vs  $T$

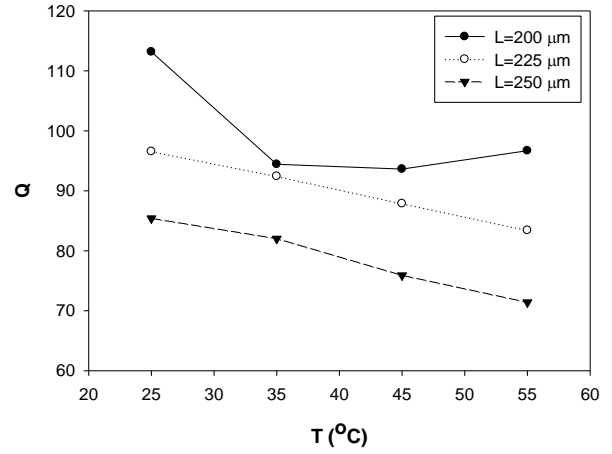


Figure 4.2:  $Q$  vs  $T$

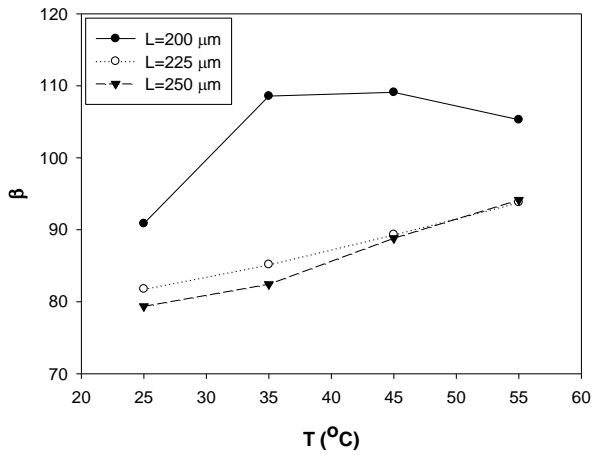


Figure 4.3:  $\beta$  vs  $T$

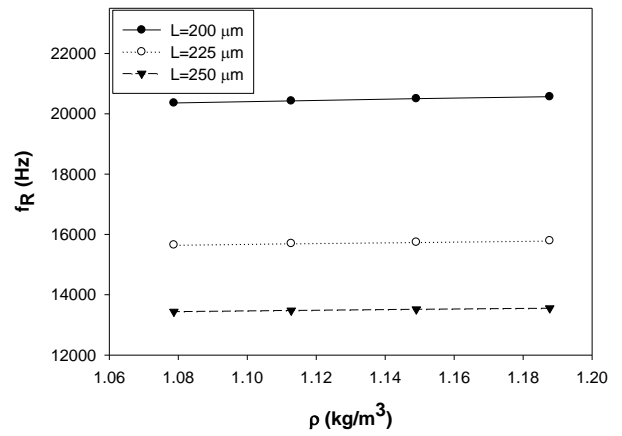
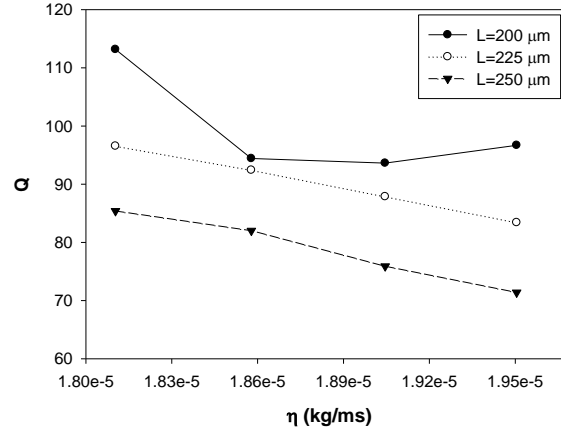


Figure 4.4:  $f_R$  vs  $\rho$



**Figure 4.5:** Q vs  $\eta$

As seen in Figure 4.1-5,  $f_R$  and Q decrease slightly whereas damping parameter,  $\beta$ , increases as temperature increases.

It is interesting that  $f_R$  decreases with decreasing density as temperature increases. In the incompressible region, i.e. low pressure region, it is well known that the density acts as added mass decreasing  $f_R$  [10], so we expect  $f_R$  to increase with decreasing density. In that case, the reason why  $f_R$  decreases may be that the length of the cantilever, i.e. the dominant dimension, increases by thermal expansion. This is evident from dependence of resonance frequency on stiffness which is inversely proportional to the length of the cantilever. The resonance frequency is defined as

$$f_R = \frac{1}{2\pi} \sqrt{\frac{k}{m^*}} \quad (4.1)$$

where  $k = \frac{Ewt^3}{4l^3}$  is the stiffness and  $m^* = n(\rho wlt)$  is the effective mass of the cantilever beam for which  $n$  ( $0 < n < 1$ ) depending on the geometry,  $\rho$  is the density and  $w$ ,  $t$  and  $l$  are width, thickness and length of cantilever, respectively.

---

On the other hand,  $Q$  decrease and  $\beta$  increase are expected results. Because the viscosity increases with temperature, the shearing motion at the tip of the cantilever damps the oscillations which results in broadening of the resonance peaks, i.e. decrease in  $Q$ , and increase in damping, i.e. high  $\beta$  values.

The curved behavior of  $Q$  and  $\beta$  plots for  $L=200\ \mu\text{m}$  cantilevers is not expected and it is possibly due to some experimental errors such as nonlinearities in the cantilever, non-equilibrium of temperature at the time of measurements, LDV spot focusing problems.

The air measurement results are accepted as the vacuum resonance spectra values for comparison with high pressure  $\text{CO}_2$  results.

## 4.2 Measurements in Pressurized $\text{CO}_2$

In this section, the results will be analyzed in the subsections according to the relationships investigated which are

- $f_R$  vs  $P$
- $f_R$  vs  $\rho$
- $f_R$  vs  $(\rho\eta)^{0.5}$
- $Q$  vs  $P$
- $Q$  vs  $\eta$
- $\beta$  vs  $\eta^{0.5}$

4.2.1  $f_R$  vs P

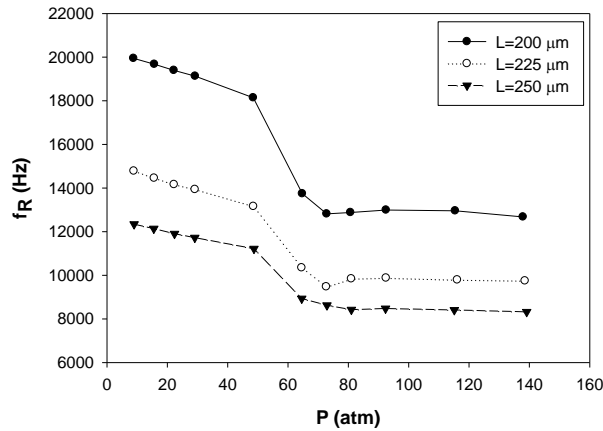


Figure 4.6:  $f_R$  vs P at  $T=25\text{ }^\circ\text{C}$

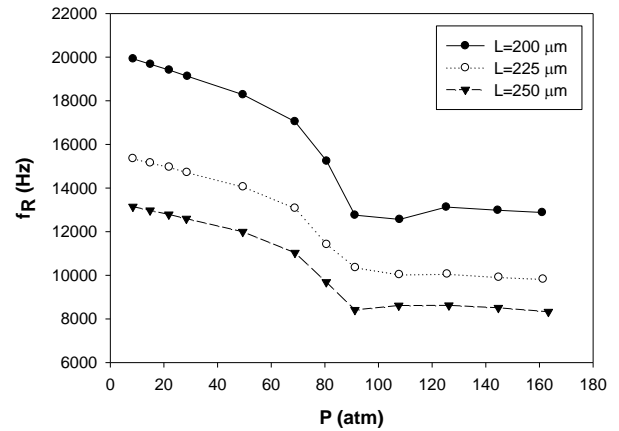


Figure 4.7:  $f_R$  vs P at  $T=35\text{ }^\circ\text{C}$

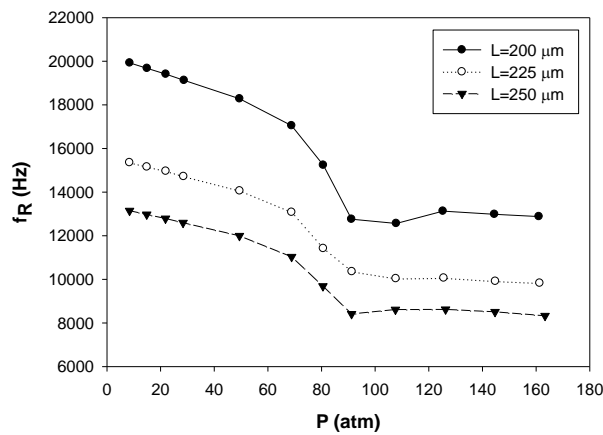


Figure 4.8:  $f_R$  vs P at  $T=45\text{ }^\circ\text{C}$

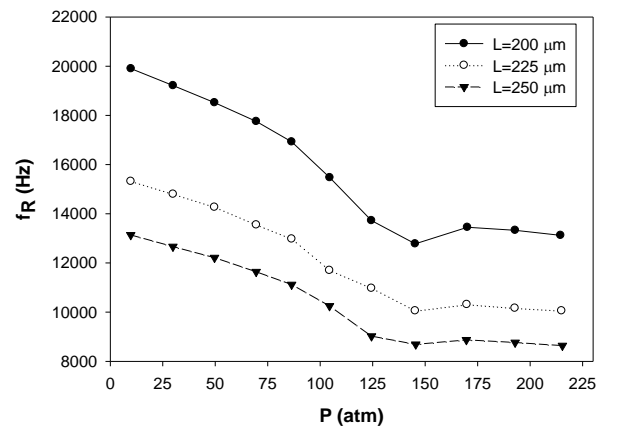


Figure 4.9:  $f_R$  vs P at  $T=55\text{ }^\circ\text{C}$

The trend is common in all temperatures for all cantilevers, i.e. the resonance frequency apparently decreases up to some point and then it slightly decreases. The phase transition accounts for this trend since the density and viscosity of the medium suddenly

changes which in turn affects the hydrodynamics around the oscillating microcantilever. In addition to that, the phase transition is manifested itself in increasing order from longer to shorter cantilevers. This is due to higher sensitivity of shorter cantilevers to pressure which is obvious when the increased pressure is assumed as the added mass, as shown in Equation 4.2 [41].

$$\frac{\Delta f}{f} \cong -\frac{1}{2} \frac{\Delta m}{m} \quad (4.2)$$

For  $T=25\text{ }^{\circ}\text{C}$ , the phase transition is from gas to liquid phase and for other temperatures, it is from gas to supercritical phase. The deep points in  $T=25\text{ }^{\circ}\text{C}$  correspond to region around bubble point pressure for which it is observed that the bubble formation creates additional damping and decreases the resonance frequency. The bubble formation is due to heating by the LDV laser at the bubble point pressure. Figure 4.10 shows a video capture of the bubble formation at  $T=25\text{ }^{\circ}\text{C}$  and  $P=64\text{ atm}$ .

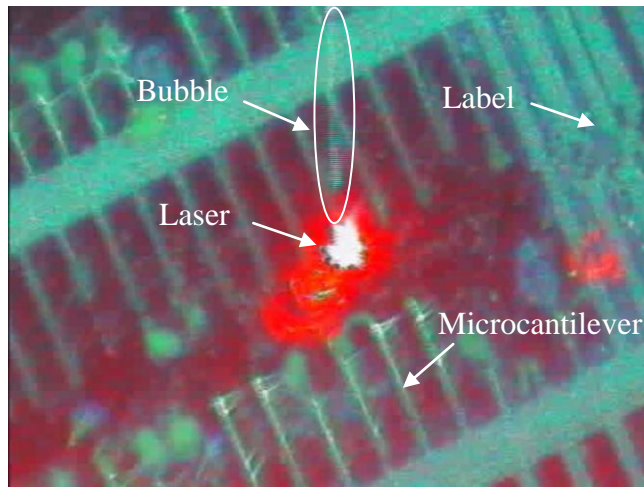


**Figure 4.10:** Video capture of bubbling of  $\text{CO}_2$  on microcantilevers at bubble point

For the other temperatures, the points around the deep are not deterministic because drifts in resonance frequencies are observed in subsequent measurements. For example,  $f_R$  of  $L=225 \mu\text{m}$  cantilever at  $T=35 \text{ }^\circ\text{C}$  are measured as 11417 Hz, 11369 Hz and 11322 Hz at  $P=80.68 \text{ atm}$  and 10355 Hz, 10131 Hz and 10074 Hz at  $P=91.36 \text{ atm}$ . For analysis, the first measurement result is used as the resonance frequency. The reason for the drift around the deep points is investigated and it is found that the increase in compressibility of  $\text{scCO}_2$  may play a role. The points where drift occurs at a temperature forms a band which can be represented with the compressibility as shown in Figure 4.11-14.

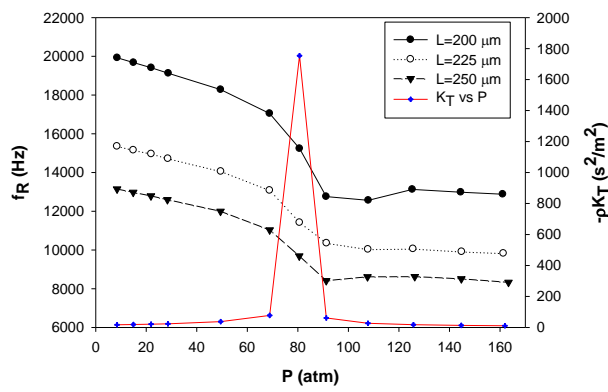


**Figure 4.11:**  $f_R$  and  $-\rho K_T$  vs  $P$  at  $T=35 \text{ }^\circ\text{C}$

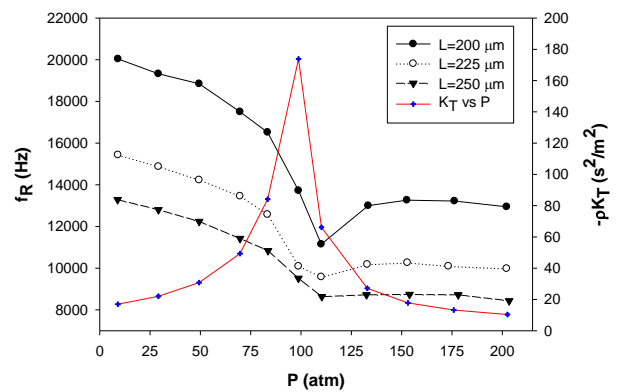


**Figure 4.12:**  $f_R$  and  $-\rho K_T$  vs  $P$  at  $T=45 \text{ }^\circ\text{C}$

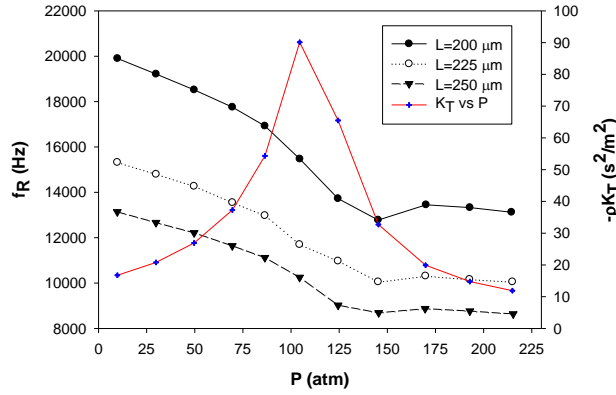


Figure 4.13:  $f_R$  and  $-\rho K_T$  vs  $P$  at  $T=55\text{ }^\circ\text{C}$

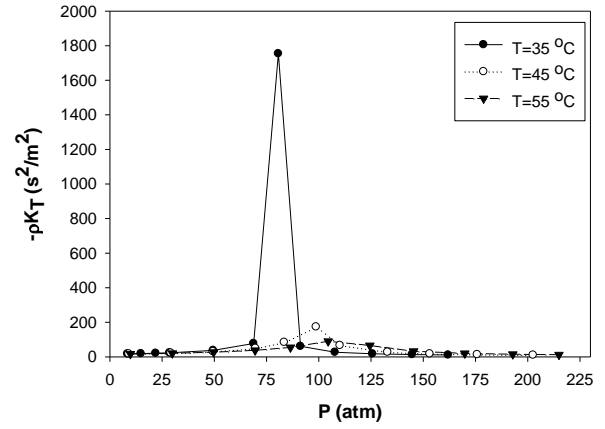


Figure 4.14:  $-\rho K_T$  vs  $P$  at all  $T$

As seen above, the drift occurs around the maxima of the isothermal compressibility multiplied by density (proposed as “denormalized compressibility”) which is defined as  $-\rho K_T = \left(\frac{\partial \rho}{\partial P}\right)_T$  for which the calculation and raw data is given in Appendix section A.4. It is also seen that since the denormalized compressibility decreases with increasing temperature, the transition becomes softer as shown in Figure 4.15-17.

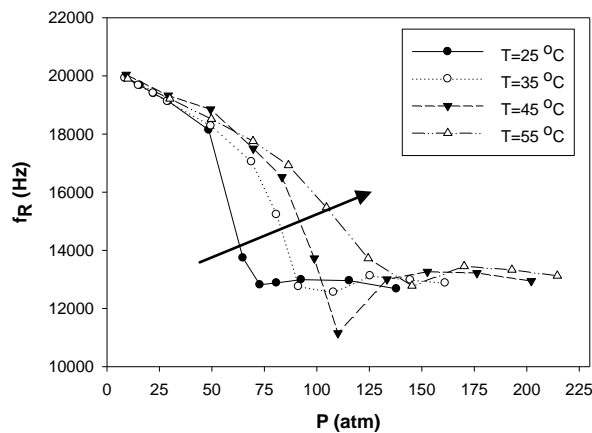


Figure 4.15:  $f_R$  vs  $P$  for  $L=200\text{ }\mu\text{m}$

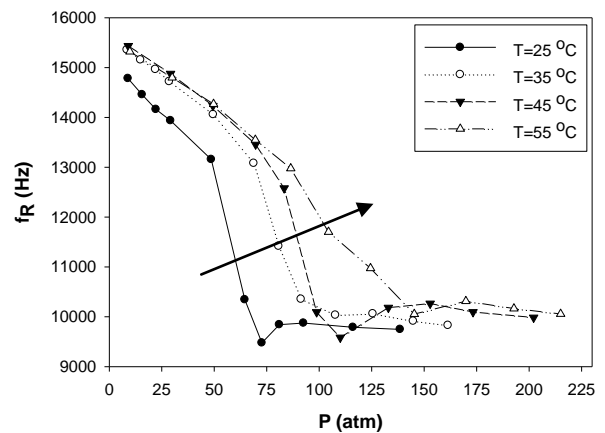
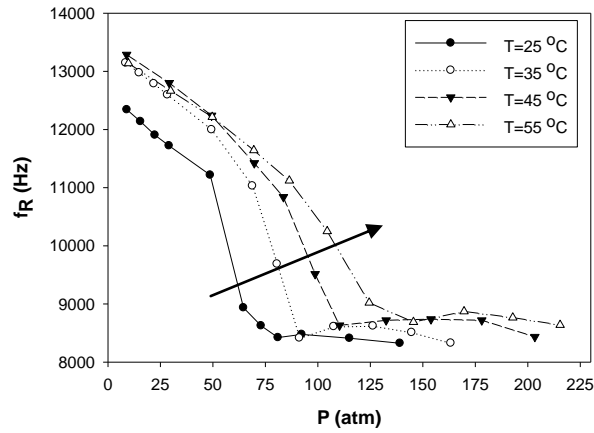


Figure 4.16:  $f_R$  vs  $P$  for  $L=225\text{ }\mu\text{m}$



**Figure 4.17:**  $f_R$  vs  $P$  for  $L=250 \mu\text{m}$

Moreover, the maximum of the denormalized compressibility shifts to a higher pressure and the curve broadens.

This occurrence of drifts may be explained using the theory developed by Sader et al. [18]. A representative plot of real part of the hydrodynamic function versus a dimensionless parameter is shown in Figure 4.18.

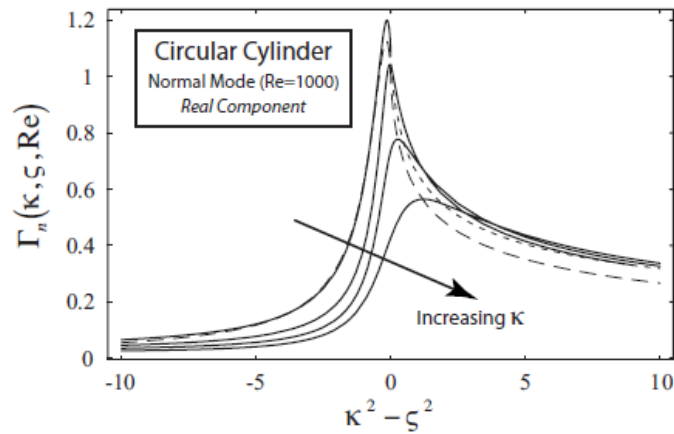


**Figure 4.18:** Real part of hydrodynamic function vs  $\kappa^2 - \zeta^2$  [18]



In Figure 4.18, the  $\kappa$  parameter is the normalized mode number and  $\zeta$  is a dimensionless variable which is proportional to the compressibility. In the plot  $\kappa=0, 2, 3, 4, 5$  values are used as depicted by the arrow. Most operations using MEMS are in the  $\zeta < \kappa$  region, so the left half plane is the working plane. In that region, at a constant  $\kappa$ , a decrease in  $\zeta$  corresponds to an increase in  $\Gamma$ . The resonance frequency is shown to be inversely proportional to the real part of the hydrodynamic function in previous works by Sader et al. [6, 18, 30]. Thus, resonance frequency is expected to decrease with decreased compressibility. This result is validated in our case by the drifts around the deep points. Since the LDV laser continually heats up the microcantilever, a situation that is shown in an aforementioned video capture (see Figure 4.10), the denormalized compressibility of  $\text{CO}_2$  around the cantilever decreases resulting subsequent decreases in resonance frequencies upon continuous subjection to LDV laser.

4.2.2  $f_R$  vs  $\rho$

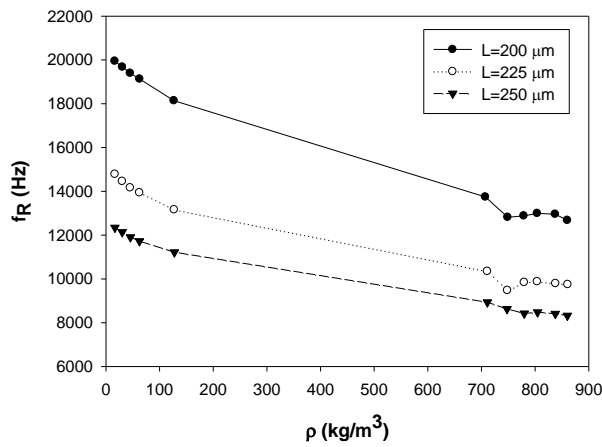


Figure 4.19:  $f_R$  vs  $\rho$  at  $T=25^\circ\text{C}$

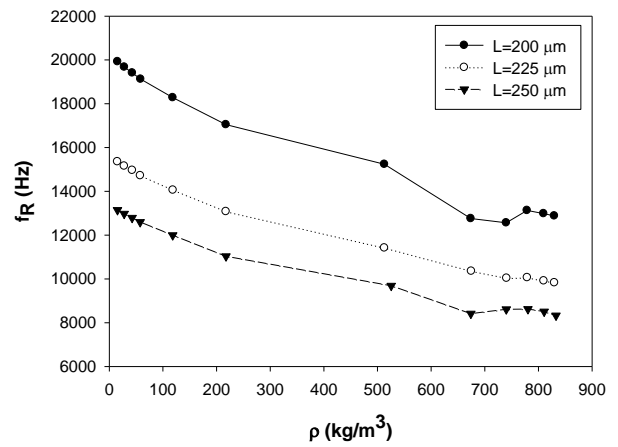
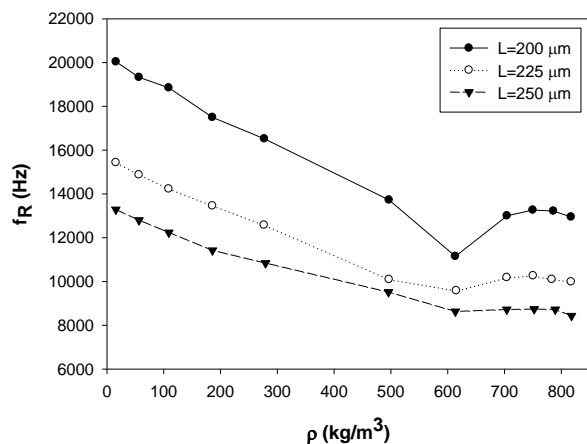
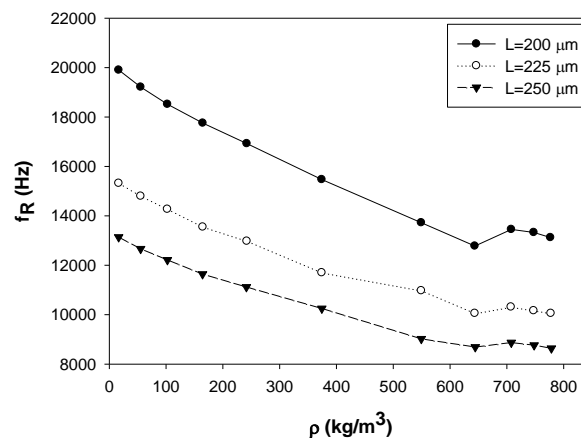


Figure 4.20:  $f_R$  vs  $\rho$  at  $T=35^\circ\text{C}$



**Figure 4.21:**  $f_R$  vs  $\rho$  at  $T=45$  °C



**Figure 4.22:**  $f_R$  vs  $\rho$  at  $T=55$  °C

As seen from the Figure 4.19-22,  $f_R$  decreases when density increases at all temperatures for all cantilevers. The decrease is larger in gas phase compared to that in liquid ( $T=25$  °C) and supercritical phase ( $T=35$  °C,  $45$  °C,  $55$  °C). This is due to the larger density variations throughout the gas phase in contrast to those in liquid and supercritical phase. The resonance frequency decrease with increasing density can be explained by the increase in added mass around the microcantilever. The dominance of density increase in the resonance frequency decrease is obvious since the increases in density up to liquid and supercritical phases are 133, 173, 129 and 115 folds whereas the increases in viscosity in the same region are 35 %, 51 %, 28% and 20% for  $T=25$  °C,  $T=35$  °C,  $T=45$  °C and  $T=55$  °C, respectively. This suggests that the effects of density and viscosity can be decomposed by the microcantilevers in a good fashion in the gas phase. Moreover, the variation in the gas is found to be linear with  $R^2$  values greater than 0.97 for all cases as shown in Figure 4.23-26. Furthermore, the slopes decreases as the cantilever length increases implying that the sensitivity of shorter cantilevers are higher compared to longer cantilevers as explained

on page 33. This linear change is not observed in liquid and supercritical phase which are given in Appendix section A.3.

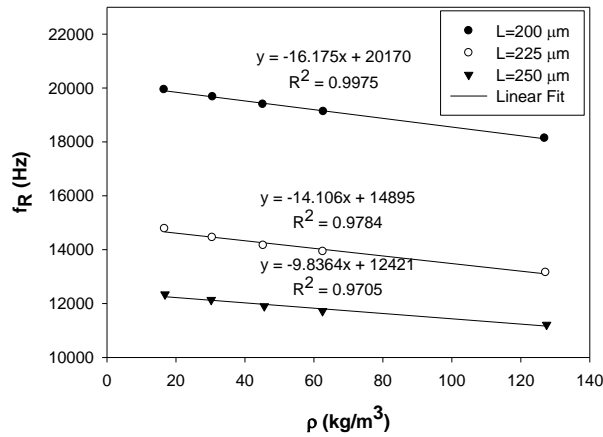


**Figure 4.23:**  $f_R$  vs  $\rho$  at  $T=25$  °C (gas)

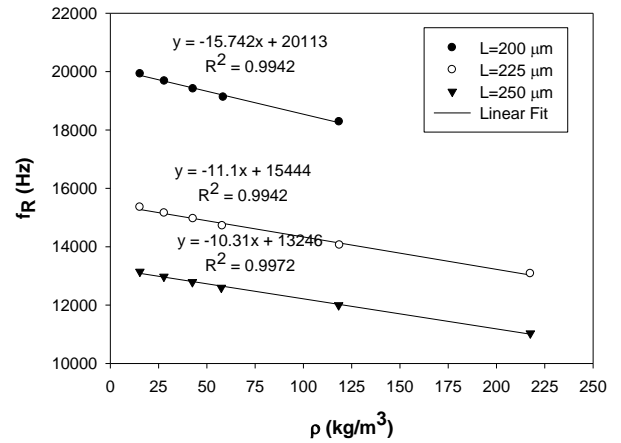


**Figure 4.24:**  $f_R$  vs  $\rho$  at  $T=35$  °C (gas)

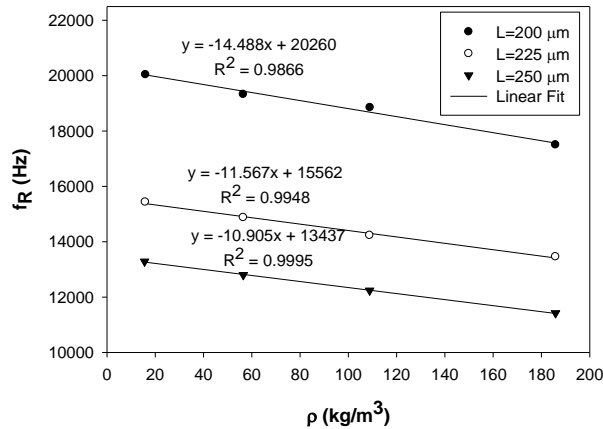


**Figure 4.25:**  $f_R$  vs  $\rho$  at  $T=45$  °C (gas)

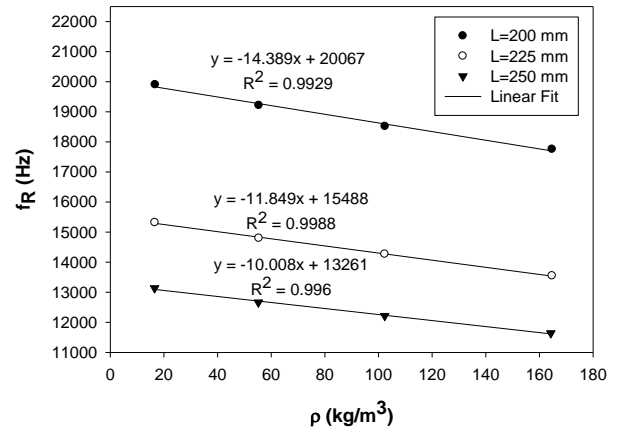


**Figure 4.26:**  $f_R$  vs  $\rho$  at  $T=55$  °C (gas)

This linear change can be useful in the calculation of density of  $\text{CO}_2$  in the gas phase through a calibration procedure. The calibration involves the determination of

---

resonance frequencies at the lowest and highest density values known and then the linear fit. Moreover, the  $f_{\text{Rvac}}$  values can be calculated by extrapolation with average percent errors of 1.50, 2.35, 2.93 for  $L=200 \mu\text{m}$ ,  $L=225 \mu\text{m}$  and  $L=250 \mu\text{m}$  cantilevers, respectively. The reason why error increases with increasing length lies in the sensitivity decrease by length increase.

According to by Goodwin et al. [10], the dependence of resonance frequency on density, i.e. naïvely added mass, is due to the large surface-to-volume ratio ( $\sim 10^6$ ) and small mass of the cantilevers ( $\sim 50 \text{ ng}$ ). This phenomenon can be explained by the boundary layer thickness. When the microcantilever oscillates, a boundary layer, i.e. viscous skin depth, where main flow phenomenon takes place, is formed by viscous forces. Assuming incompressible flow, the thickness of the boundary layer,  $\delta$ , is calculated by

$$\delta = \left( \frac{\eta}{\rho \pi f} \right)^{1/2} \quad (4.3)$$

where  $f$  is the resonance frequency. The calculation of the boundary layer thickness enables the calculation of the mass of fluid pocket flowing around the cantilever assuming the thickness is constant in each dimension. Analyzing the boundary layer thicknesses in our case using the data where compressibility is insignificant (i.e. ignoring the drift region), it is observed that the boundary layer thicknesses decrease greatly up to drift (from  $\sim 4.4 \mu\text{m}$  to  $\sim 1.3 \mu\text{m}$ , averaged for all cantilevers at all temperatures), then it tends to increase (to  $\sim 1.7 \mu\text{m}$ ) as pressure is increased in the supercritical region. Investigation of the corresponding mass of fluid pocket reveals a nanogram resolution with an average of 4 ng which is about 10% mass of the cantilever. In addition, the boundary layer thickness also helps in determining the safe distance between two microcantilevers ensuring that the motions of fluid around each of them are not coupled.

For such small boundary layer thicknesses, the surface roughness has important effects on the fluid motion. When the dimensions of the molecule are much less than those of the surface roughness, molecules are trapped on the surface on the microcantilever and they act as both an additional mass and a viscous load [42]. In our study, the dimensions of CO<sub>2</sub> molecules are on the order of 10<sup>-10</sup> m [43] and the surface roughness is about 10<sup>-7</sup> m. Thus, the CO<sub>2</sub> molecules trapped on the cantilever surface enhance the added mass and render the microcantilever more sensitive to fluid density.

#### 4.2.3 $f_R$ vs $(\rho\eta)^{0.5}$

In the study by McHale et al. [44], it is proposed that the resonance frequency must change linearly with the square root of density-viscosity product. This relationship is investigated in our study as shown in Figure 4.27-30.

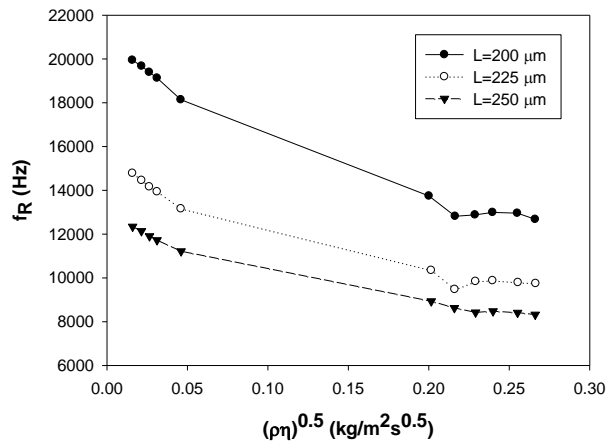


**Figure 4.27:**  $f_R$  vs  $(\rho\eta)^{0.5}$  at T=25 °C

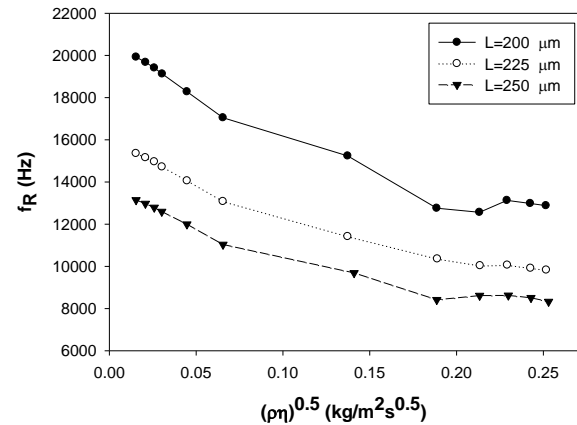


**Figure 4.28:**  $f_R$  vs  $(\rho\eta)^{0.5}$  at T=35 °C

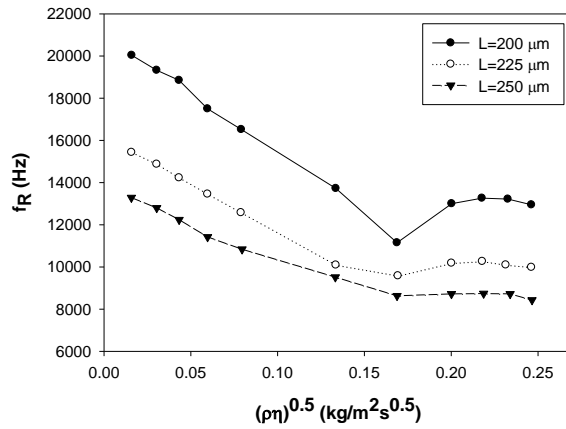


**Figure 4.29:**  $f_R$  vs  $(\rho\eta)^{0.5}$  at  $T=45$  °C

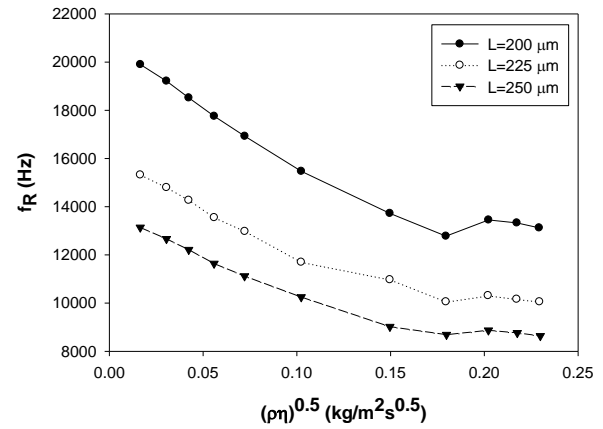


**Figure 4.30:**  $f_R$  vs  $(\rho\eta)^{0.5}$  at  $T=55$  °C

It is seen that the trend is similar to that of  $f_R$  vs  $P$  and  $f_R$  vs  $\rho$ . The variations in liquid and supercritical phases are not linear as shown in Appendix section A.3, however the linear relationship is validated with a good accuracy in the gas phase as shown in Figure 4.31-34. This result can be combined with the linearity of resonance frequency versus density in the gas phase as shown in Figure 4.23-26 and enables the calculation of viscosity with an error less than 1 % using the aforementioned calibration procedure. The reason why both  $f_R$  vs  $\rho$  and  $f_R$  vs  $(\rho\eta)^{0.5}$  plots behave linearly in the gas phase region lies in the linearity of  $\rho$  vs  $\eta$  in the gas phase  $\text{CO}_2$ . In addition, the decreases in slopes with increasing lengths of cantilevers again indicate the higher sensitivity of shorter cantilevers.

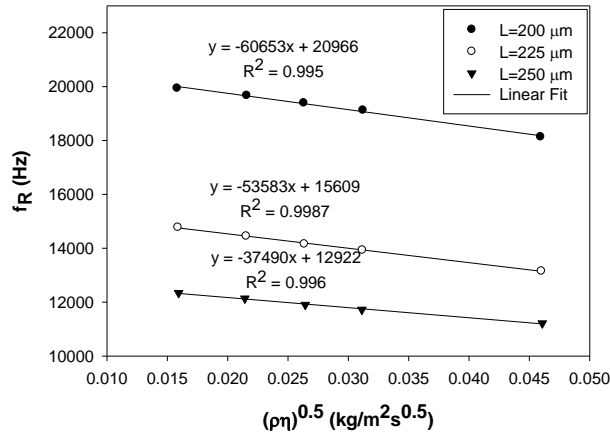


Figure 4.31:  $f_R$  vs  $(\rho\eta)^{0.5}$  at  $T=25$  °C (gas)

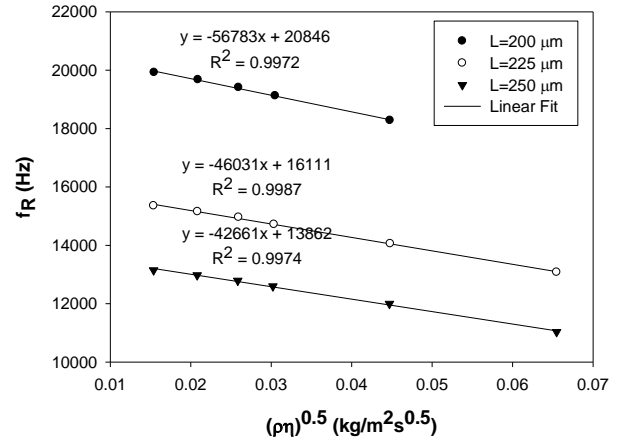


Figure 4.32:  $f_R$  vs  $(\rho\eta)^{0.5}$  at  $T=35$  °C (gas)

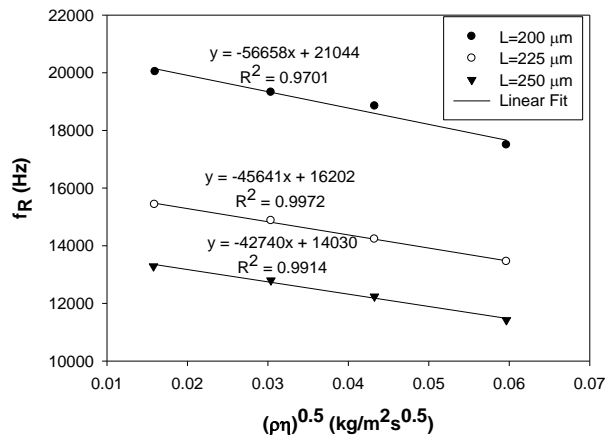


Figure 4.33:  $f_R$  vs  $(\rho\eta)^{0.5}$  at  $T=45$  °C (gas)

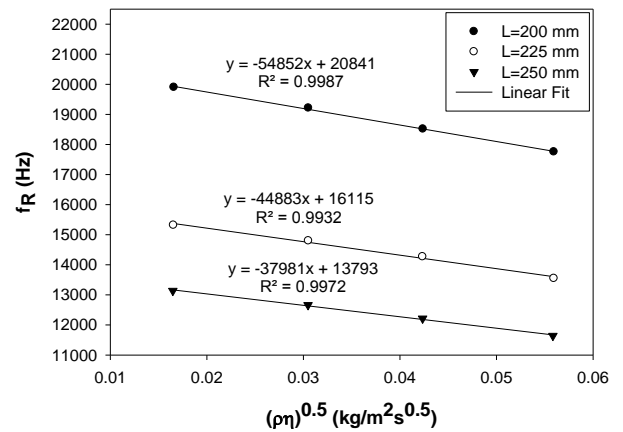
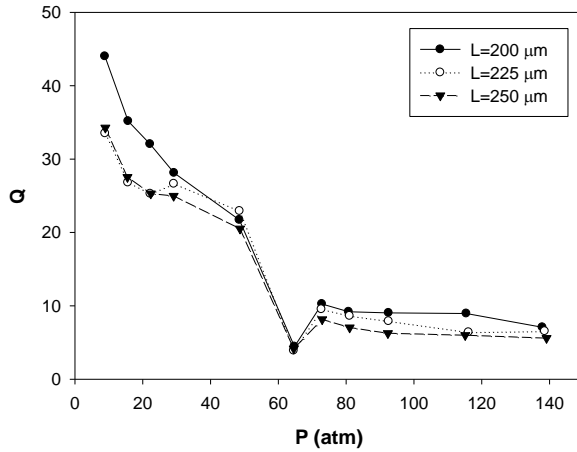


Figure 4.34:  $f_R$  vs  $(\rho\eta)^{0.5}$  at  $T=55$  °C (gas)

#### 4.2.4 Q vs P

A relation between the quality factor, Q, and pressure is investigated. The results are plotted in Figure 4.35-38.



**Figure 4.35:** Q vs P at T=25 °C

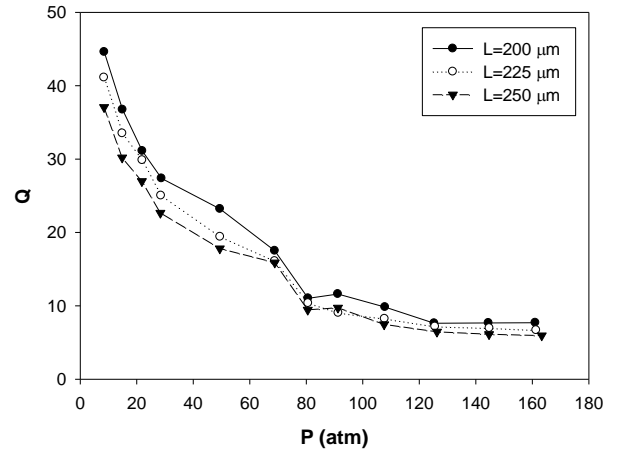


**Figure 4.36:** Q vs P at T=35 °C

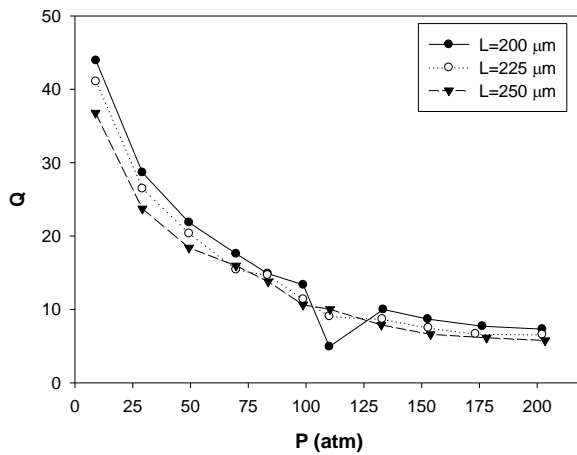


**Figure 4.37:** Q vs P at T=45 °C

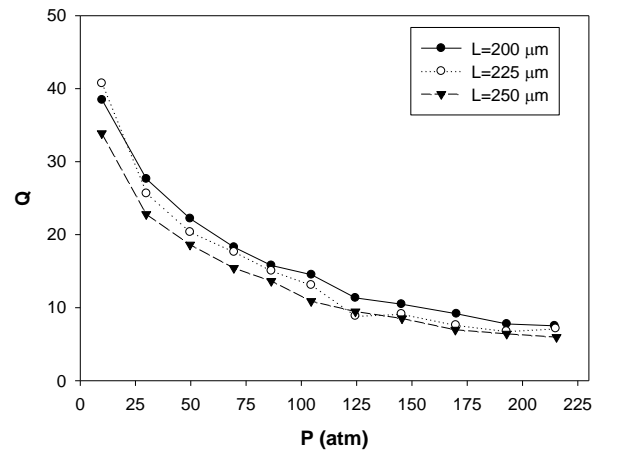


**Figure 4.38:** Q vs P at T=55 °C

There seems a quadratic relationship between quality factor and pressure. At T=25 °C, quality factor attains its deep around the phase transition region. As the temperature increases, this deep vanishes gradually as the curves become smoother. This is possibly due to the effect of decreased compressibility. The decrease in quality factor upon increase in pressure can be explained by the increase in viscosity. Because the viscosity increases,



the shearing motion creates more damping at the tip cantilever broadening the amplitude versus resonance curves. Moreover, the quality factor values decrease as the length increases, which may be related to the sensitivity of the cantilevers [45]. However, the trend is not so clear. This is because there are always problems in acquiring the quality factor values during the measurements. A more convenient way to acquire the resonance spectra values, i.e. resonance frequency and quality factor, must be used such as noise-free power spectrum instead of conventional frequency sweep followed by Lorentzian fitting.

#### 4.2.5 Q vs $\eta$

A relation between the quality factor and viscosity is investigated according to Tamika et al. and Etchart et al. [29, 46] as shown in Figure 4.39-42.

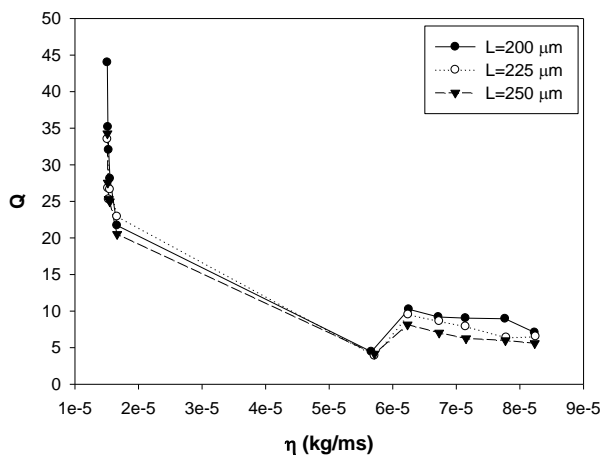


Figure 4.39: Q vs  $\eta$  at T=25 °C

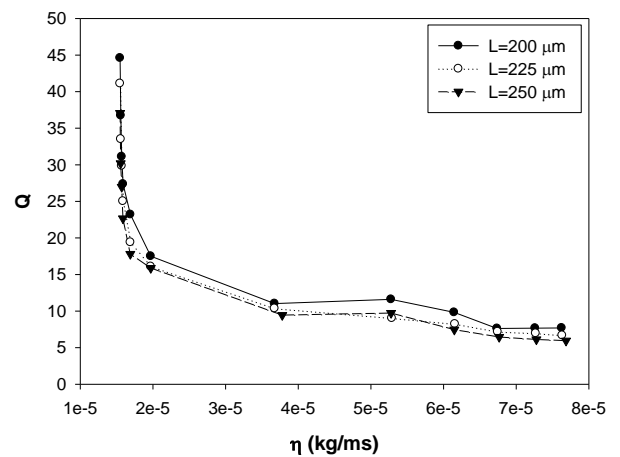
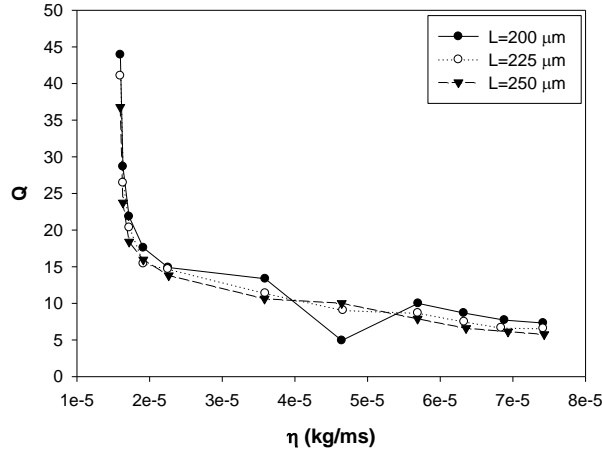
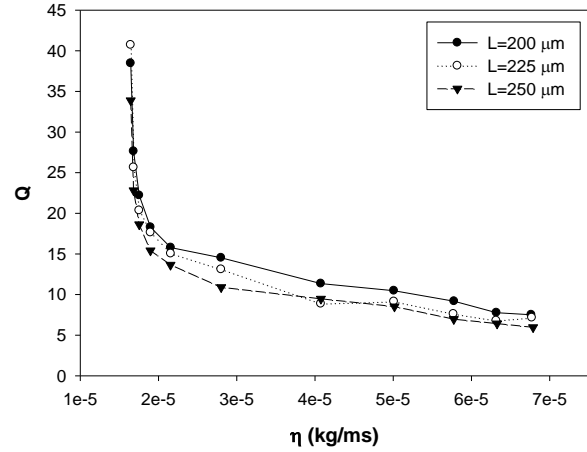


Figure 4.40: Q vs  $\eta$  at T=35 °C



**Figure 4.41:**  $Q$  vs  $\eta$  at  $T=45$  °C



**Figure 4.42:**  $Q$  vs  $\eta$  at  $T=55$  °C

It is seen that in the gas phase the quality factor values change abruptly with an infinitesimal viscosity change. A somewhat quadratic relationship in the phase transition region is followed by almost linear behavior at higher pressures. The deep in Figure 4.39 is due to bubbling at the phase transition. Thus, it can be said that there are three trends: first, a drastic decrease in quality vector at nearly constant viscosity in the gas phase, next, a quadratic relationship in the phase transition (except the  $T=25$  °C case), and finally a linear relationship. Virtually no difference is observed at different temperatures for the same cantilever quality factor response with respect to viscosity as shown in Appendix section A.3.

#### 4.2.6 $\beta$ vs $\eta^{0.5}$

In the study by Schilowitz et al. [5], it is proposed that there must be a linear relationship between the damping parameter and square root of viscosity. This relationship is investigated in our study.

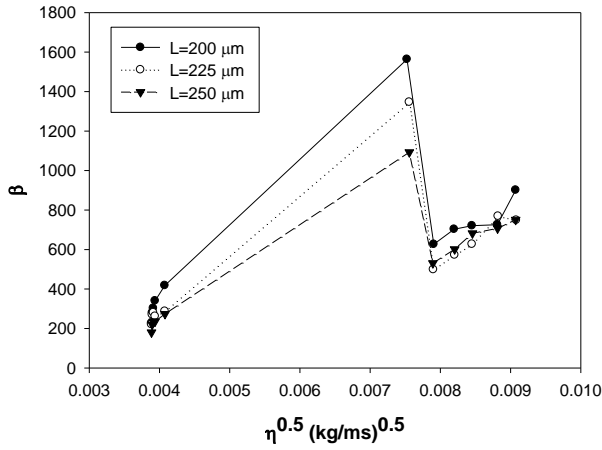


**Figure 4.43:**  $\beta$  vs  $\eta^{0.5}$  at  $T=25$  °C

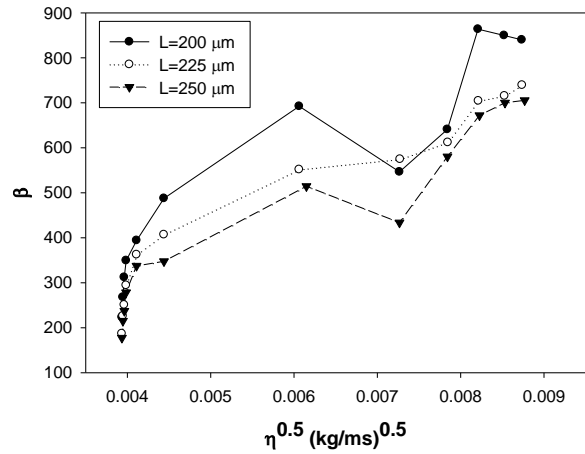


**Figure 4.44:**  $\beta$  vs  $\eta^{0.5}$  at  $T=35$  °C

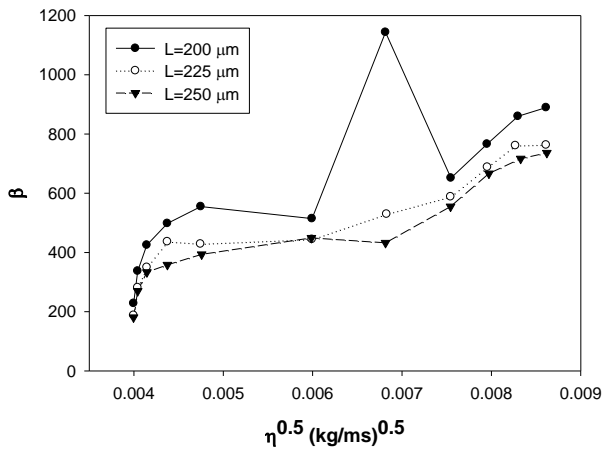


**Figure 4.45:**  $\beta$  vs  $\eta^{0.5}$  at  $T=45$  °C

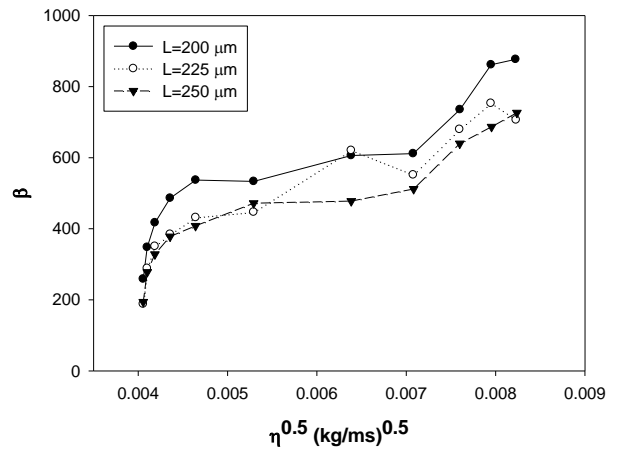


**Figure 4.46:**  $\beta$  vs  $\eta^{0.5}$  at  $T=55$  °C

As seen in Figure 4.43-46, this relationship is not validated in our case. This may be due to the multilayered structure of the cantilevers used in this study whereas the theory is developed using single layer cantilevers. The general trend in damping parameter is first a rapid and then a gradual increase with respect to square root of viscosity. The damping parameter values around the phase transition region are generally deviate from the

monotonic increase such as the case for T=25 °C. At T=25 °C, the damping parameter increases dramatically due to bubble formation. Also, the damping parameter is observed to increase with decreasing length. This is possibly due to the sensitivity of the cantilevers. When the relationship is investigated in the gas phase, a general trend can be achieved as shown in Figure 4.47-50.

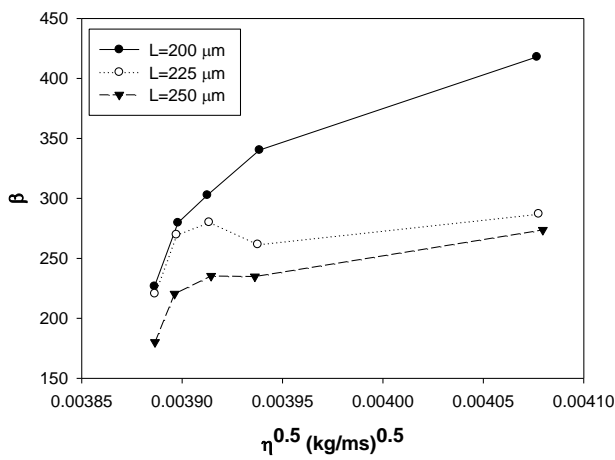


**Figure 4.47:**  $\beta$  vs  $\eta^{0.5}$  at T=25 °C (gas)

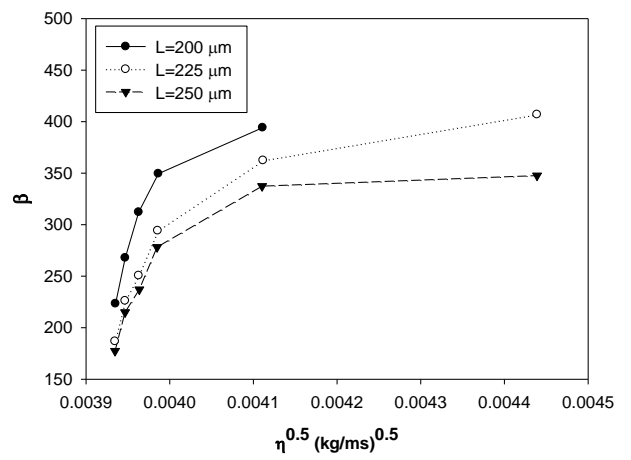


**Figure 4.48:**  $\beta$  vs  $\eta^{0.5}$  at T=35 °C (gas)

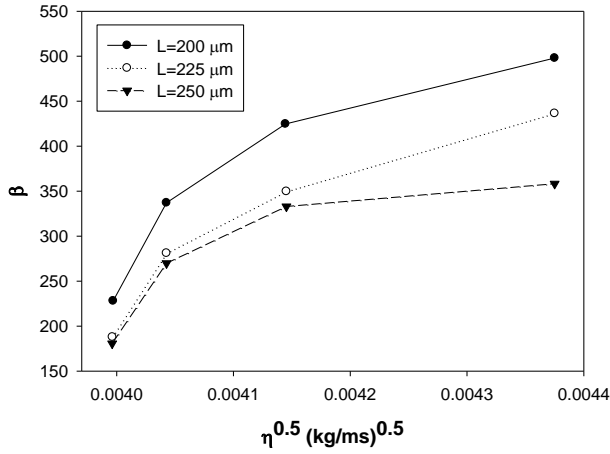


**Figure 4.49:**  $\beta$  vs  $\eta^{0.5}$  at  $T=45$  °C (gas)

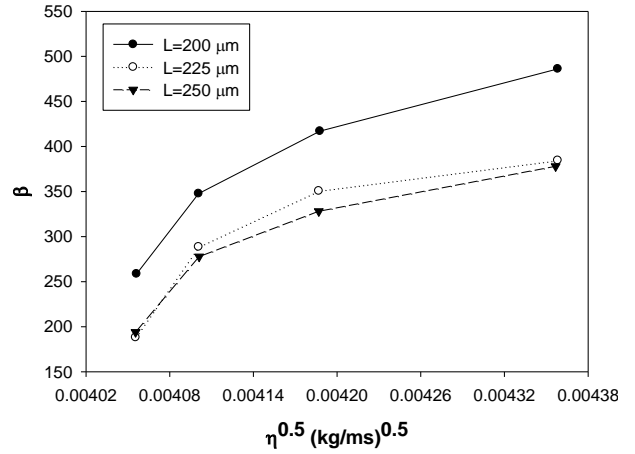


**Figure 4.50:**  $\beta$  vs  $\eta^{0.5}$  at  $T=55$  °C (gas)

Analyzing the trends, it can be proposed that there is a somewhat quadratic relationship between the damping parameter and the square root of viscosity. Moreover, the damping increases for shorter cantilevers for all cases. However, these relationships are not so certain since there is always problem in quality factor acquisition, thus in damping parameter calculation as quality factors and damping parameters are inversely related quantities.

---

## Chapter 5

### 5 Conclusion

#### 5.1 Conclusion

In this study, the frequency response of microcantilevers in CO<sub>2</sub> was investigated in order to relate the thermophysical properties such as density ( $\rho$ ), viscosity ( $\eta$ ) and isothermal compressibility ( $K_T$ ) to the resonance frequency ( $f_R$ ), quality factor ( $Q$ ) and damping parameter ( $\beta$ ). This thesis is the study that investigates the frequency response of microcantilevers in supercritical medium. An experimental setup is prepared starting from scratch. It involves the custom designed Teflon housing for holding microcantilever chip and electromagnetic coil, the high pressure resistant leak-free glands for electrical connection to the coil, the passive vibration isolation pads placed under the granite block which acts as a damper to eliminate vibration. Improvements have been implemented in the fabrication of microcantilevers with high length-to-width ratio. Experiments are conducted in a large pressure range of 1 atm to 200 atm at 25 °C, 35 °C, 45 °C and 55 °C using 200  $\mu\text{m}$ , 225  $\mu\text{m}$ , 250  $\mu\text{m}$  long, 20  $\mu\text{m}$  wide and 1  $\mu\text{m}$  thick multilayered Ni microcantilevers consisting thin Cr and Au films. Sinusoidal electromagnetic actuation and optical detection by LDV are used. Analyzing the results, it is seen that  $f_R$  decreases with increasing  $\rho$  and  $Q$  decreases with increasing  $\eta$ . The changes in  $f_R$  and  $Q$  are larger in the gas phase than those in the liquid or supercritical (sc) phase. Additionally, linear relationships between  $f_R$  and  $\rho$  as well as between  $f_R$  and  $(\rho\eta)^{0.5}$  are observed in the gas phase. This enables the determination of  $\rho$  and  $\eta$  through a simple calibration with percentage errors less than 1 %. Moreover, the extrapolation of  $f_R$  versus  $\rho$  line gives the  $f_{Rvac}$  values with percentage errors less than 3%. A somewhat quadratic relationship was

---

observed between  $Q$  and  $\eta$ , however there is always errors encountered in the calculation of  $Q$  using the resonance curves. Apart from that, the decreases of  $f_R$  observed in subsequent measurements (i.e. drifts) at a constant temperature and pressure were found to be described completely by the shifts of the maxima of the density multiplied by compressibility, defined as  $-\rho K_T = \left(\frac{\partial \rho}{\partial P}\right)_T$ , through LDV heating. Moreover, the effect of phase transition (from gas to liquid or from gas to sc) on resonance spectra was evidently observed. For example, at the bubble point pressure at 25 °C, microscale bubbles formed due to LDV heating can be utilized in microscale heat transfer studies and microstructure release checking.

## 5.2 Suggestions for further studies

In order to increase the efficiency of this study in terms of time and equipments, there are some suggestions listed below.

- The uppermost operating pressure and temperature limits of the equipments used, namely the pressure vessel, Swagelok fittings, pressure transducer, the gland assemblies for electrical connection for the electromagnetic actuation, are limiting factors for experiments at higher pressures and temperatures. For example, despite the possibility of malfunctioning, some experiments have to be carried out above 3000 psia (~204 atm, i.e. the mechanical limit of the pressure transducer). For that reason, these equipments must be replaced with the ones which are in the targeted operating range.
- A common trend in the experiments is the unreliable  $Q$  measurement. This is due to very low  $Q$  values at high pressures. In that case, an active feedback circuit and

---

driving system (i.e. electromagnetic actuation) may be used for assisted self-oscillation of the microcantilevers at their resonance frequencies. This feedback system increases the quality factor and the sensitivity of the microcantilevers drastically [47]. Since driving system is also used, the frequency sweep outlined in this study can be used to obtain the resonance spectra.

- Another bottleneck is the focusing of the laser beam on the cantilever surface. Lack of focusing distorts the signal and adds noise that it becomes impossible to obtain a clear resonance fitting. Focal length of a 10X lens is almost suitable for operations at low pressures. However the refractive index of  $\text{CO}_2$  changes from 1 to 1.5 with increasing pressure which in turn decreases the focal length. Thus, focusing problems arise at high pressures. The focal length is the sum of the following terms: the distance of chip to the inner surface of the sapphire window, the thickness of the sapphire window, the clearance of the lid of the pressure vessel and the distance between the lid and the LDV lens. The only variables are the clearance of the front lid and the distance between the lid and the LDV lens. To decrease the total distance, the clearance is decreased by lathing to an extent that LDV lens fits into the lid as shown in Figure 5.1.

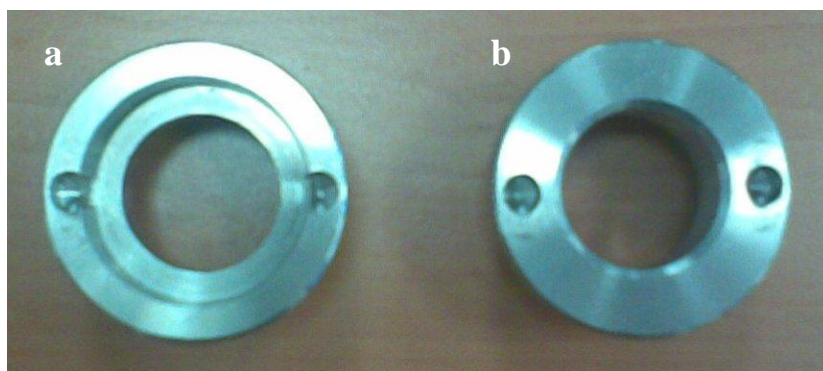


**Figure 5.1:** Lids of the pressure vessel. a) Lathed front lid b) Back lid



---

However, it is observed that this decrease seems to be insufficient. Despite that, measurements are able to be taken with very sensitive adjustments where focusing problems are encountered. A practical solution for focusing problems is to fabricate microcantilevers wider than 20  $\mu\text{m}$ .

- Mechanical and acoustic vibration causes noise in the measurements. This is eliminated in great extent by using passive vibration isolation pads mounted under the breadboard. However, the noise caused by the cables of the equipments still contributes to noise. For that reason, the vibration isolation pads can be mounted under the table on which the equipments and the breadboard are located. The upper weight limit of the pads is sufficient for that operation.
- The heating may be supplied by the recirculator or electrical heater. During experiments, it is observed that a larger heating rate is attained by using the electrical heater. However, the electrical connections must be shielded very carefully.
- Measurements of resonance frequency can be performed quickly using a power spectrum analyzer. However, since the quality factor cannot be read directly from the analyzer, an image processing procedure is needed for the analyzer screen capture to fit the equation of motion and acquire the quality factor.
- To acquire more data points in the vicinity of the critical point, much better temperature and pressure control are needed.
- Instead of CRT TV used in combination with LDV, video capturing devices such as Easycap is advantageous in terms of capturing videos such as bubbling phenomenon.
- The automation of the measurements can be achieved using LabVIEW and appropriate National Instruments virtual devices. In that case, there may be no need

---

for oscilloscope, signal generator, preamplifier and the data acquisition and analysis can be done quickly.

- In order to simplify the actuation and detection, piezoelectric actuation and piezoresistive detection methods should be incorporated as the microcantilevers are fabricated. However, this requires additional investment for fabrication laboratory and a very careful, rational design of the microcantilevers.

### 5.3 Future Work

There is more work to do in order to strengthen the scientific basis of this study. First, to reach a general conclusion about the behavior of microcantilever resonators in supercritical medium, many data points in supercritical medium are needed at different temperatures. For that reason, equipments that can withstand high pressure and temperature are needed. In addition, for quantitative calculations of fluid dynamics using own-written code or commercial softwares like COMSOL and ANSYS Fluent, the microcantilevers must be characterized to obtain the actual stiffness and elasticity modulus values. Also, the temperature and pressure must be carefully controlled for accurate modeling and simulations. Next, experiments using mixtures (e.g.  $\text{CCl}_4$ , acetone, ether) in supercritical phase must be conducted in order to understand the effect of concentration on resonance spectra.

This study is the first step in the collaboration of Energy Technologies and Supercritical Fluids Laboratory (ETSFL, supervised by Prof. Can Erkey) with Cleanroom (supervised by Prof. Erdem Alaca) and Optical Microsystems Laboratory (OML, supervised by Prof. Hakan Ürey). This collaboration will continue with possible future work. Currently, the main ideas are to develop new techniques and devices using MEMS for real-time measurement of various thermophysical phenomena in supercritical medium.

---

First, the feasibility of permeability measurements of materials like aerogels and polymers is being discussed. Second, the measurement of elasticity modulus of thin films composed of newly developed insulation materials in ETSFL is being evaluated. Next, the real-time adsorption and desorption measurements are being assessed. Finally, it is thought that the kinetic measurements of various catalytic reactions taking place in supercritical medium may be possible.

---

## Appendix

### A.1 Raw Experimental Data

The density and viscosity values are obtained from [48]. The data are given with respect to lengths of the microcantilevers. The colored data depict the points where drifts are observed.

#### A.1.1 Raw Data for L=200 $\mu\text{m}$

**Table A.1:** Raw data for L=200  $\mu\text{m}$  at room temperature

<b>P (atm)</b>	<b>T (<math>^{\circ}\text{C}</math>)</b>	<b>Phase</b>	<b><math>\rho</math> (<math>\text{kg}/\text{m}^3</math>)</b>	<b><math>\eta</math> (<math>\text{kg}/\text{ms}</math>)</b>	<b><math>f_R</math> (Hz)</b>	<b>Q</b>	<b><math>\beta</math></b>
8.84	26.9	g	16.54	1.51E-05	19947	44.01	226.66
15.71	26.6	g	30.63	1.52E-05	19677	35.18	279.72
22.18	26.1	g	45.18	1.53E-05	19397	32.05	302.70
29.25	26.0	g	62.76	1.55E-05	19130	28.11	340.31
48.50	25.4	g	126.90	1.66E-05	18139	21.71	417.95
64.76	25.5	dbl pt	707.24	5.66E-05	13742	4.45	1563.59
72.86	25.6	liq	749.05	6.25E-05	12816	10.25	626.84
80.75	25.2	liq	779.09	6.72E-05	12882	9.19	702.81
92.52	25.3	liq	804.09	7.14E-05	12994	9.04	720.77
115.44	25.6	liq	837.48	7.77E-05	12958	8.95	725.75
137.89	26.1	liq	860.17	8.23E-05	12679	7.07	901.05

**Table A.2:** Raw data for L=200  $\mu\text{m}$  at T=35  $^{\circ}\text{C}$ 

<b>P (atm)</b>	<b>T (<math>^{\circ}\text{C}</math>)</b>	<b>Phase</b>	<b><math>\rho</math> (<math>\text{kg}/\text{m}^3</math>)</b>	<b><math>\eta</math> (<math>\text{kg}/\text{ms}</math>)</b>	<b><math>f_R</math> (Hz)</b>	<b>Q</b>	<b><math>\beta</math></b>
8.50	35.0	g	15.40	1.55E-05	19924	44.60	223.38
14.97	35.0	g	28.04	1.56E-05	19677	36.74	267.82
21.97	34.8	g	42.84	1.57E-05	19412	31.10	312.13
28.78	35.0	g	58.48	1.59E-05	19125	27.37	349.50
49.46	35.0	g	118.49	1.69E-05	18282	23.21	394.10
68.84	35.1	g	217.52	1.97E-05	17049	17.50	487.51
80.68	35.2	sc	512.88	3.68E-05	15236	11.02	692.40
91.22	35.2	sc	674.03	5.28E-05	12757	11.61	546.61
107.89	35.2	sc	739.98	6.15E-05	12562	9.82	640.92
125.31	35.2	sc	778.76	6.74E-05	13127	7.63	863.76
144.49	35.1	sc	809.67	7.26E-05	12985	7.67	849.70
161.09	35.2	sc	829.59	7.63E-05	12879	7.70	839.99

**Table A.3:** Raw data for L=200  $\mu\text{m}$  at T=45  $^{\circ}\text{C}$ 

<b>P (atm)</b>	<b>T (<math>^{\circ}\text{C}</math>)</b>	<b>Phase</b>	<b><math>\rho</math> (<math>\text{kg}/\text{m}^3</math>)</b>	<b><math>\eta</math> (<math>\text{kg}/\text{ms}</math>)</b>	<b><math>f_R</math> (Hz)</b>	<b>Q</b>	<b><math>\beta</math></b>
9.12	45.1	g	15.97	1.60E-05	20039	43.94	228.07
29.18	44.9	g	56.48	1.63E-05	19327	28.67	337.12
49.39	44.8	g	108.99	1.72E-05	18850	21.85	424.73
69.73	45.2	g	185.84	1.91E-05	17502	17.59	498.00
83.40	45.0	sc	277.23	2.26E-05	16521	14.90	555.08
98.78	45.1	sc	496.73	3.59E-05	13724	13.36	514.43
110.07	45.0	sc	613.49	4.64E-05	11150	4.93	1143.69
133.40	45.4	sc	704.41	5.70E-05	13001	10.00	651.41
152.65	45.1	sc	749.98	6.32E-05	13265	8.69	766.13
176.26	45.2	sc	786.15	6.88E-05	13220	7.72	859.91
202.18	45.1	sc	817.22	7.42E-05	12946	7.31	889.35

**Table A.4:** Raw data for L=200  $\mu\text{m}$  at T=55  $^{\circ}\text{C}$ 

<b>P (atm)</b>	<b>T (<math>^{\circ}\text{C}</math>)</b>	<b>Phase</b>	<b><math>\rho</math> (<math>\text{kg}/\text{m}^3</math>)</b>	<b><math>\eta</math> (<math>\text{kg}/\text{ms}</math>)</b>	<b><math>f_R</math> (Hz)</b>	<b>Q</b>	<b><math>\beta</math></b>
9.86	55.0	g	16.73	1.65E-05	19901	38.47	258.71
29.93	55.1	g	55.40	1.68E-05	19213	27.63	347.75
49.73	55.0	g	102.43	1.75E-05	18517	22.21	417.09
69.59	55.1	g	164.74	1.90E-05	17756	18.28	486.10
86.46	54.9	sc	242.20	2.16E-05	16926	15.78	536.86
104.56	55.2	sc	374.25	2.80E-05	15471	14.52	533.40
124.42	54.9	sc	549.32	4.08E-05	13725	11.34	606.16
145.31	55.1	sc	643.70	5.01E-05	12778	10.47	611.42
170.14	55.1	sc	707.96	5.78E-05	13452	9.17	735.51
192.93	55.1	sc	747.51	6.32E-05	13329	7.77	861.67
214.56	55.0	sc	776.91	6.76E-05	13123	7.52	876.67

**A.1.2 Raw Data for L=225  $\mu\text{m}$** **Table A.5:** Raw data for L=225  $\mu\text{m}$  at room temperature

<b>P (atm)</b>	<b>T (<math>^{\circ}\text{C}</math>)</b>	<b>Phase</b>	<b><math>\rho</math> (<math>\text{kg}/\text{m}^3</math>)</b>	<b><math>\eta</math> (<math>\text{kg}/\text{ms}</math>)</b>	<b><math>f_R</math> (Hz)</b>	<b>Q</b>	<b><math>\beta</math></b>
8.91	26.9	g	16.68	1.51E-05	14781	33.51	220.57
15.65	26.5	g	30.51	1.52E-05	14458	26.80	269.80
22.24	26.2	g	45.30	1.53E-05	14161	25.29	280.12
29.18	25.9	g	62.61	1.55E-05	13937	26.64	261.66
48.57	25.4	g	127.20	1.66E-05	13158	22.92	287.15
64.56	25.3	bbl pt	710.96	5.71E-05	10345	3.91	1346.39
72.72	25.6	liq	748.51	6.24E-05	9477	9.53	498.63
81.02	25.2	liq	779.79	6.73E-05	9843	8.62	572.54
92.52	25.3	liq	804.09	7.14E-05	9875	7.90	627.12
116.12	25.6	liq	838.36	7.78E-05	9789	6.40	769.09
138.57	26.1	liq	860.87	8.25E-05	9747	6.55	748.61

**Table A.6:** Raw data for L=225  $\mu\text{m}$  at T=35  $^{\circ}\text{C}$ 

<b>P (atm)</b>	<b>T (<math>^{\circ}\text{C}</math>)</b>	<b>Phase</b>	<b><math>\rho</math> (<math>\text{kg}/\text{m}^3</math>)</b>	<b><math>\eta</math> (<math>\text{kg}/\text{ms}</math>)</b>	<b><math>f_R</math> (Hz)</b>	<b>Q</b>	<b><math>\beta</math></b>
8.44	34.9	g	15.29	1.55E-05	15356	41.12	186.76
14.90	35.0	g	27.90	1.56E-05	15156	33.51	226.15
21.97	34.8	g	42.84	1.57E-05	14963	29.86	250.61
28.57	35.0	g	57.97	1.59E-05	14720	25.03	294.21
49.52	35.0	g	118.70	1.69E-05	14058	19.41	362.39
68.84	35.1	g	217.52	1.97E-05	13081	16.09	406.92
80.68	35.2	sc	512.88	3.68E-05	11417	10.37	551.82
91.36	35.2	sc	674.88	5.29E-05	10355	9.04	574.65
107.76	35.1	sc	740.71	6.16E-05	10035	8.23	612.06
125.58	35.2	sc	779.26	6.75E-05	10061	7.18	704.43
144.83	35.1	sc	810.13	7.27E-05	9913	6.96	715.49
161.36	35.2	sc	829.89	7.63E-05	9829	6.68	739.42

**Table A.7:** Raw data for L=225  $\mu\text{m}$  at T=45  $^{\circ}\text{C}$ 

<b>P (atm)</b>	<b>T (<math>^{\circ}\text{C}</math>)</b>	<b>Phase</b>	<b><math>\rho</math> (<math>\text{kg}/\text{m}^3</math>)</b>	<b><math>\eta</math> (<math>\text{kg}/\text{ms}</math>)</b>	<b><math>f_R</math> (Hz)</b>	<b>Q</b>	<b><math>\beta</math></b>
9.05	45.0	g	15.85	1.60E-05	15434	41.08	187.88
29.18	44.9	g	56.48	1.63E-05	14877	26.47	281.13
49.39	45.0	g	108.82	1.72E-05	14232	20.36	349.79
69.73	45.2	g	185.84	1.91E-05	13458	15.43	436.50
83.33	45.0	sc	276.59	2.25E-05	12579	14.69	428.76
98.78	45.1	sc	496.73	3.59E-05	10093	11.38	444.24
110.07	44.9	sc	615.23	4.66E-05	9584	9.07	529.72
132.93	45.3	sc	704.10	5.69E-05	10182	8.68	588.24
152.86	45.1	sc	750.36	6.33E-05	10266	7.49	687.99
173.27	45.0	sc	783.36	6.84E-05	10096	6.67	761.01
202.18	45.1	sc	817.22	7.42E-05	9984	6.58	762.90

**Table A.8:** Raw data for L=225  $\mu\text{m}$  at T=55  $^{\circ}\text{C}$ 

<b>P (atm)</b>	<b>T (<math>^{\circ}\text{C}</math>)</b>	<b>Phase</b>	<b><math>\rho</math> (<math>\text{kg}/\text{m}^3</math>)</b>	<b><math>\eta</math> (<math>\text{kg}/\text{ms}</math>)</b>	<b><math>f_R</math> (Hz)</b>	<b>Q</b>	<b><math>\beta</math></b>
9.80	54.9	g	16.63	1.64E-05	15319	40.73	188.09
29.93	55.1	g	55.40	1.68E-05	14798	25.65	288.55
49.66	54.9	g	102.31	1.75E-05	14269	20.36	350.64
69.59	55.1	g	164.74	1.90E-05	13549	17.63	384.54
86.46	54.9	sc	242.20	2.16E-05	12977	15.05	431.59
104.42	55.1	sc	374.15	2.80E-05	11702	13.11	447.07
124.42	54.9	sc	549.32	4.08E-05	10972	8.87	620.56
145.31	55.1	sc	643.70	5.01E-05	10055	9.14	551.60
169.86	55.1	sc	707.39	5.77E-05	10313	7.62	679.89
192.79	55.1	sc	747.30	6.32E-05	10164	6.78	753.21
215.03	55.0	sc	777.47	6.77E-05	10057	7.15	706.33

**A.1.3 Raw Data for L=250  $\mu\text{m}$** **Table A.9:** Raw data for L=250  $\mu\text{m}$  at room temperature

<b>P (atm)</b>	<b>T (<math>^{\circ}\text{C}</math>)</b>	<b>Phase</b>	<b><math>\rho</math> (<math>\text{kg}/\text{m}^3</math>)</b>	<b><math>\eta</math> (<math>\text{kg}/\text{ms}</math>)</b>	<b><math>f_R</math> (Hz)</b>	<b>Q</b>	<b><math>\beta</math></b>
8.98	26.9	g	16.82	1.51E-05	12342	34.28	180.07
15.51	26.4	g	30.23	1.52E-05	12138	27.54	220.40
22.38	26.3	g	45.61	1.53E-05	11904	25.30	235.31
29.12	25.7	g	62.53	1.55E-05	11722	24.97	234.84
48.71	25.6	g	127.51	1.66E-05	11217	20.51	273.65
64.56	25.3	bbl pt	710.96	5.71E-05	8935	4.15	1092.36
72.93	25.7	liq	747.79	6.23E-05	8626	8.15	530.87
81.02	25.2	liq	779.79	6.73E-05	8423	7.04	601.45
92.31	25.2	liq	804.61	7.15E-05	8477	6.25	682.24
115.10	25.5	liq	837.75	7.77E-05	8411	5.99	707.08
139.12	26.3	liq	860.21	8.23E-05	8324	5.59	750.65



**Table A.10:** Raw data for L=250  $\mu\text{m}$  at T=35  $^{\circ}\text{C}$ 

<b>P (atm)</b>	<b>T (<math>^{\circ}\text{C}</math>)</b>	<b>Phase</b>	<b><math>\rho</math> (<math>\text{kg}/\text{m}^3</math>)</b>	<b><math>\eta</math> (<math>\text{kg}/\text{ms}</math>)</b>	<b><math>f_R</math> (Hz)</b>	<b>Q</b>	<b><math>\beta</math></b>
8.44	34.9	g	15.29	1.55E-05	13146	37.06	177.37
14.83	35.0	g	27.76	1.56E-05	12977	30.19	214.97
21.84	35.0	g	42.51	1.57E-05	12789	26.98	237.10
28.37	35.0	g	57.49	1.59E-05	12597	22.65	278.19
49.39	35.0	g	118.24	1.69E-05	11997	17.80	337.34
68.84	35.1	g	217.52	1.97E-05	11031	15.88	347.63
80.54	35.0	sc	525.61	3.78E-05	9687	9.44	514.42
91.22	35.2	sc	674.03	5.28E-05	8416	9.73	433.70
107.55	35.1	sc	740.13	6.15E-05	8613	7.45	580.36
126.26	35.2	sc	780.49	6.77E-05	8622	6.45	672.12
144.69	35.0	sc	810.62	7.28E-05	8510	6.12	700.11
163.33	35.1	sc	832.70	7.69E-05	8327	5.94	705.57

**Table A.11:** Raw data for L=250  $\mu\text{m}$  at T=45  $^{\circ}\text{C}$ 

<b>P (atm)</b>	<b>T (<math>^{\circ}\text{C}</math>)</b>	<b>Phase</b>	<b><math>\rho</math> (<math>\text{kg}/\text{m}^3</math>)</b>	<b><math>\eta</math> (<math>\text{kg}/\text{ms}</math>)</b>	<b><math>f_R</math> (Hz)</b>	<b>Q</b>	<b><math>\beta</math></b>
8.91	45.0	g	15.60	1.60E-05	13287	36.78	180.67
29.18	44.9	g	56.48	1.63E-05	12801	23.73	269.80
49.39	45.0	g	108.82	1.72E-05	12240	18.39	332.99
69.73	45.2	g	185.84	1.91E-05	11421	15.96	358.25
83.61	45.0	sc	279.18	2.26E-05	10839	13.79	393.39
98.71	45.1	sc	495.66	3.58E-05	9514	10.62	448.89
110.34	45.1	sc	613.52	4.65E-05	8630	10.01	432.20
132.52	45.2	sc	703.96	5.69E-05	8719	7.89	554.99
153.88	45.1	sc	752.22	6.36E-05	8738	6.59	666.46
178.10	45.1	sc	789.22	6.93E-05	8719	6.13	716.37
203.40	45.2	sc	817.94	7.43E-05	8434	5.77	736.22

**Table A.12:** Raw data for L=250  $\mu\text{m}$  at T=55  $^{\circ}\text{C}$ 

<b>P (atm)</b>	<b>T (<math>^{\circ}\text{C}</math>)</b>	<b>Phase</b>	<b><math>\rho</math> (<math>\text{kg}/\text{m}^3</math>)</b>	<b><math>\eta</math> (<math>\text{kg}/\text{ms}</math>)</b>	<b><math>f_R</math> (Hz)</b>	<b>Q</b>	<b><math>\beta</math></b>
9.73	54.9	g	16.51	1.64E-05	13138	33.88	193.92
29.86	55.2	g	55.22	1.68E-05	12664	22.80	277.79
49.66	54.9	g	102.31	1.75E-05	12214	18.63	328.10
69.46	55.1	g	164.26	1.90E-05	11642	15.41	378.05
86.39	55.0	sc	241.39	2.15E-05	11120	13.64	408.09
104.42	55.1	sc	374.15	2.80E-05	10250	10.89	471.69
124.42	54.9	sc	549.32	4.08E-05	9020	9.47	477.65
145.51	55.1	sc	644.37	5.02E-05	8689	8.52	511.83
169.66	55.0	sc	707.73	5.77E-05	8871	6.97	639.80
192.86	55.0	sc	748.03	6.33E-05	8764	6.42	686.92
215.37	54.9	sc	778.42	6.79E-05	8637	5.97	726.39

## A.2 Density and Viscosity in the Experimental Conditions

### A.2.1 Density Change in the Experimental Range

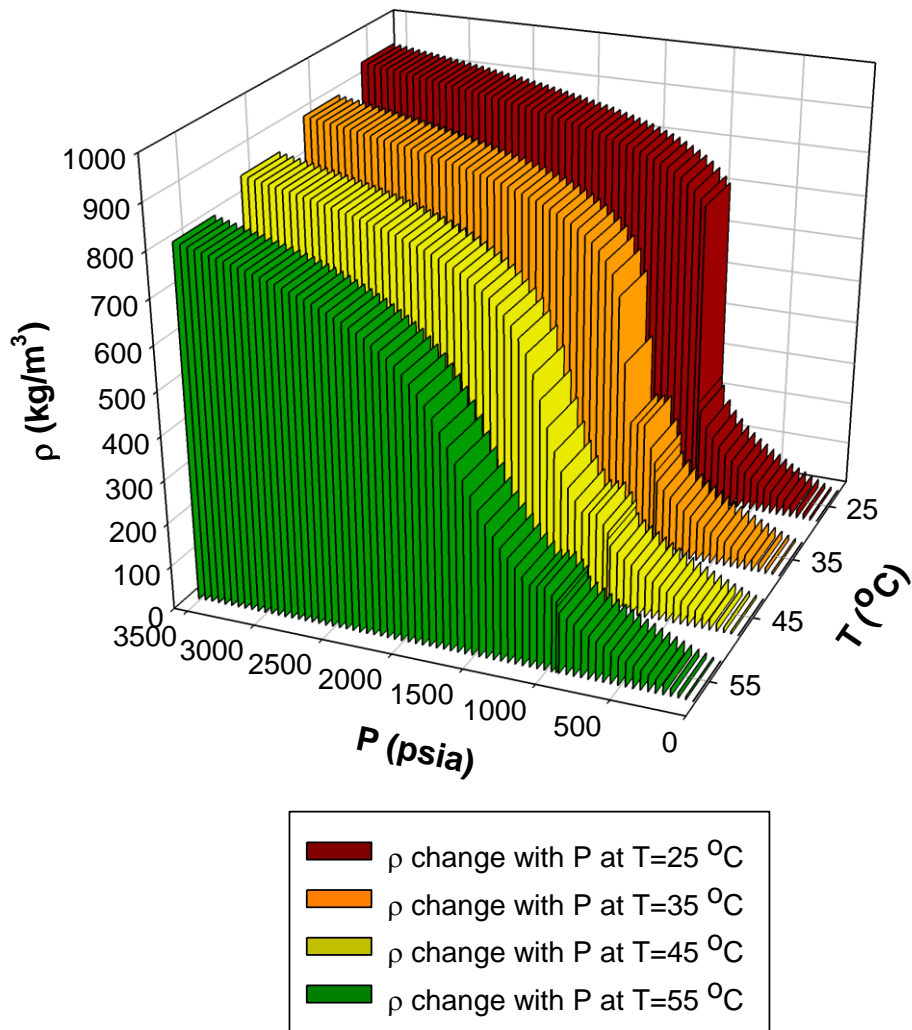


**Figure A.1:** Density variation of CO<sub>2</sub> with respect to temperature and pressure

### A.2.2 Viscosity Change in the Experimental Range

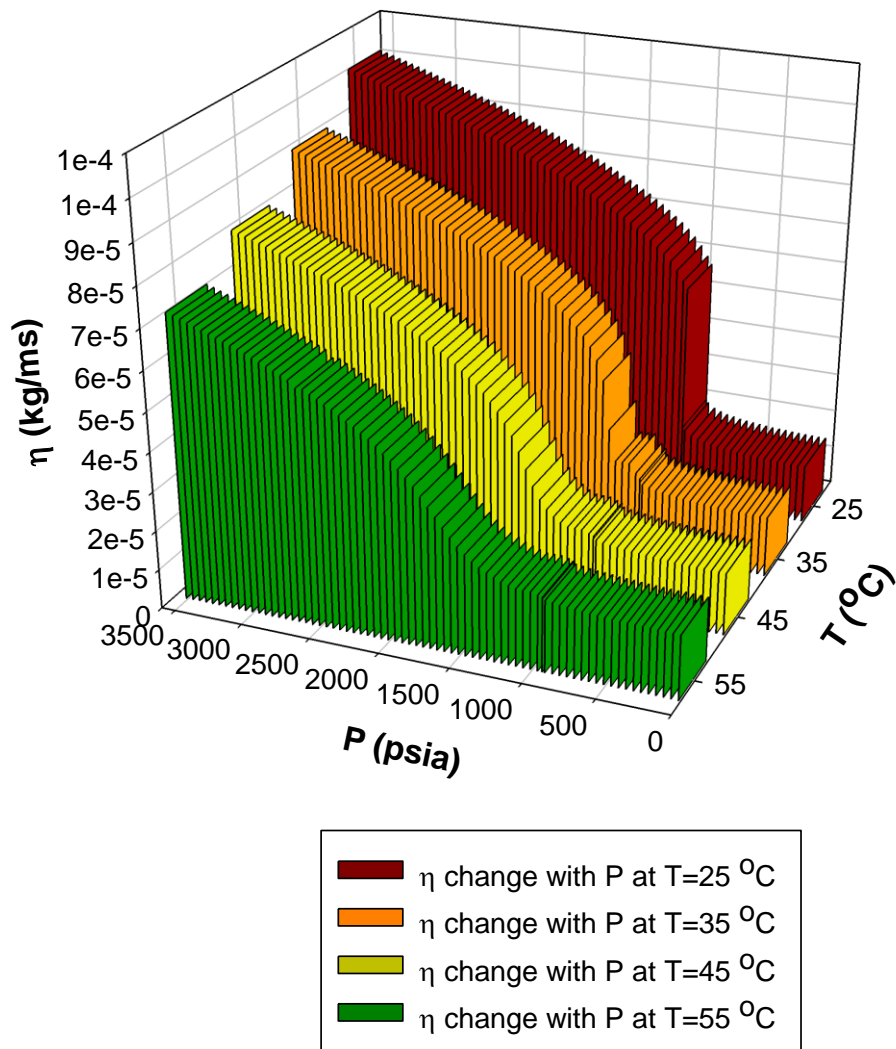


**Figure A.2:** Viscosity variation of CO<sub>2</sub> with respect to temperature and pressure

### A.3 Plotted Results

The results obtained in this study are investigated graphically first with respect to temperature then with respect to length of the microcantilevers. Nomenclature used in figure captions are sc: supercritical, ex.: excluding, dr.: drift, af.: after, meaning the data in the increasing pressure direction. For example, (sc, ex. & af. dr.) means the data at supercritical region excluding the drift and in the increasing pressure direction.

#### A.3.1 Results at T=25 °C

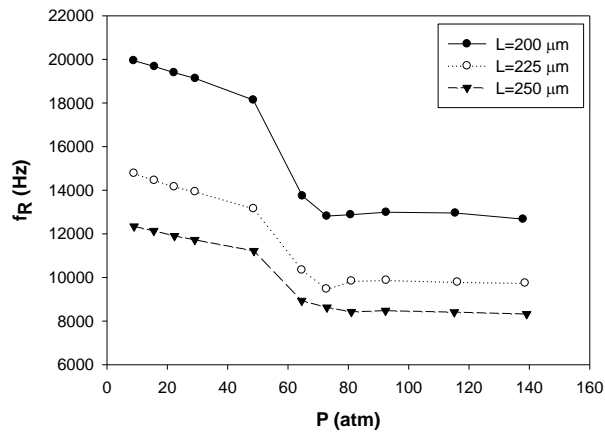


Figure A.3:  $f_R$  vs P

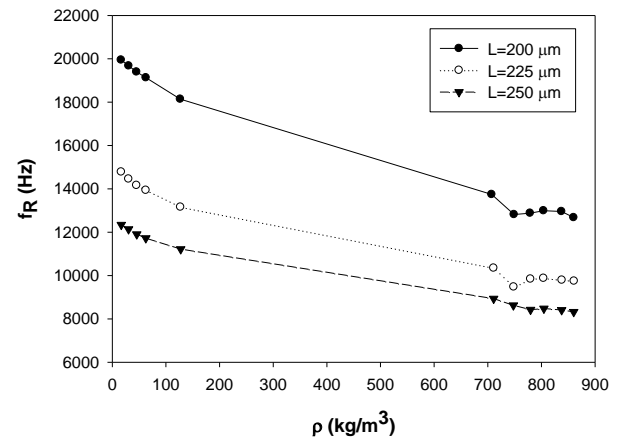


Figure A.4:  $f_R$  vs  $\rho$

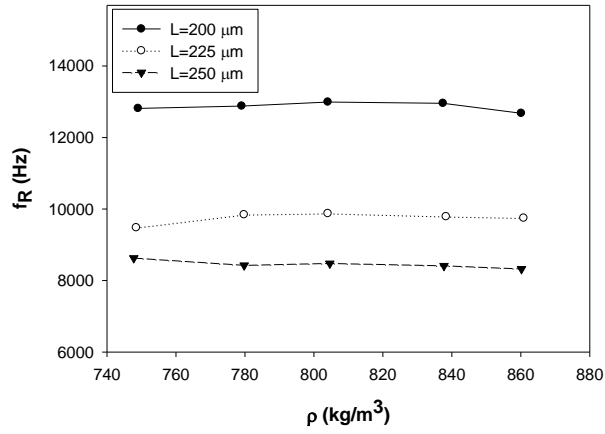


Figure A.5:  $f_R$  vs  $\rho$  (liquid)

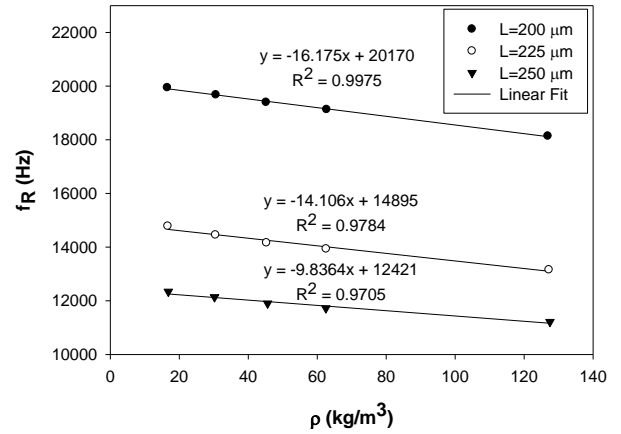


Figure A.6:  $f_R$  vs  $\rho$  (gas)

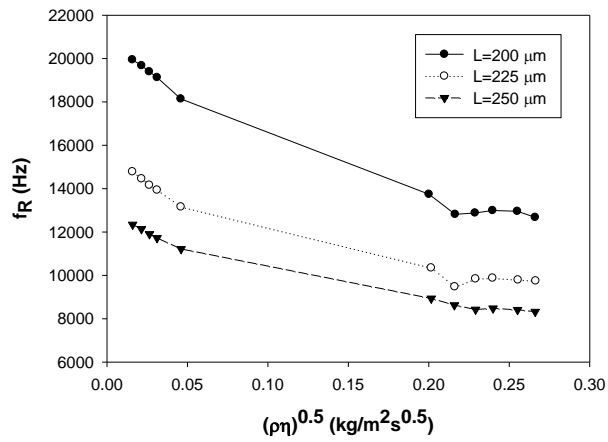


Figure A.7:  $f_R$  vs  $(\rho\eta)^{0.5}$

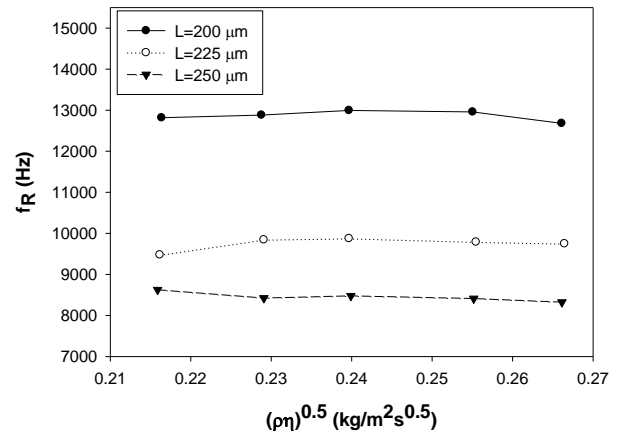


Figure A.8:  $f_R$  vs  $(\rho\eta)^{0.5}$  (liquid)

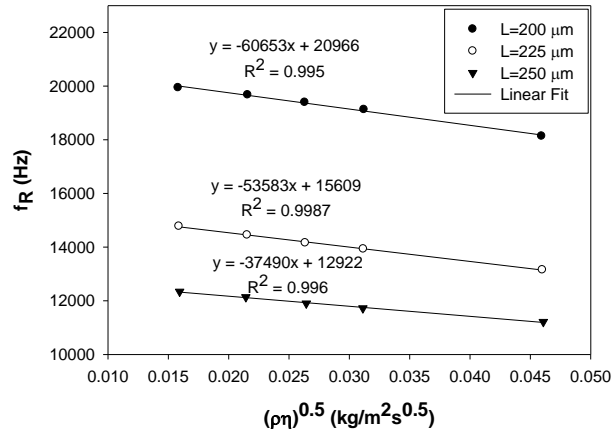


Figure A.9:  $f_R$  vs  $(\rho\eta)^{0.5}$  (gas)

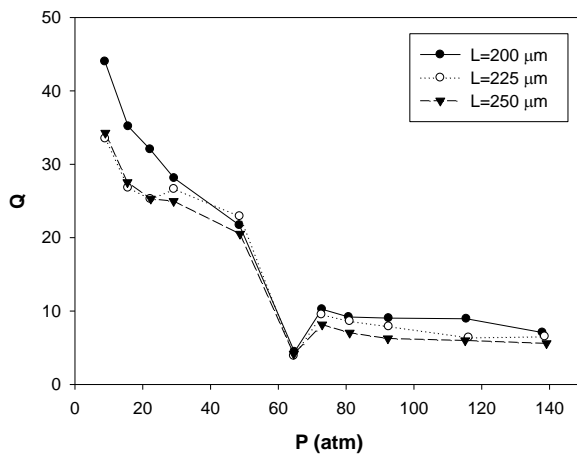


Figure A.10: Q vs P

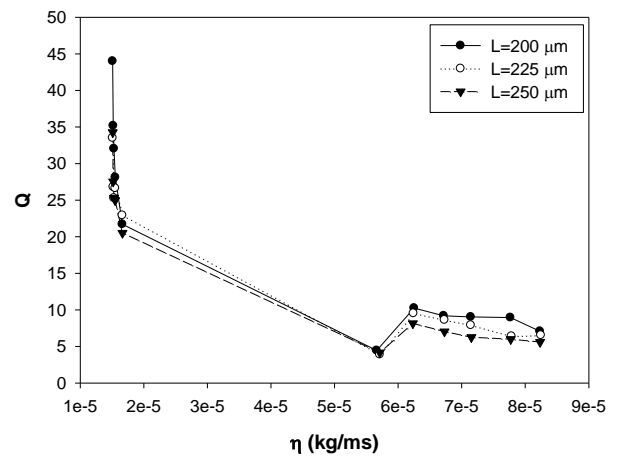


Figure A.11: Q vs  $\eta$

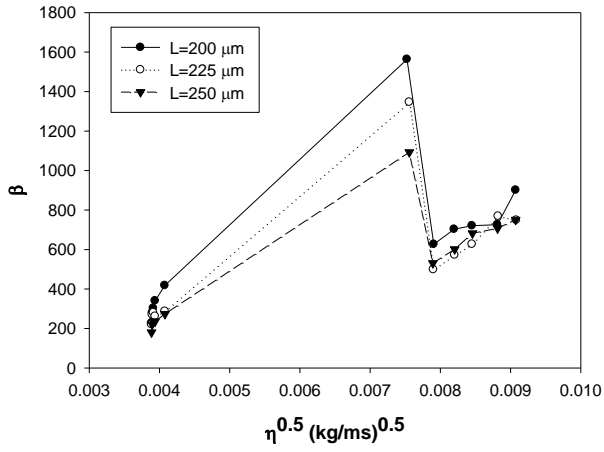


Figure A.12:  $\beta$  vs  $\eta^{0.5}$

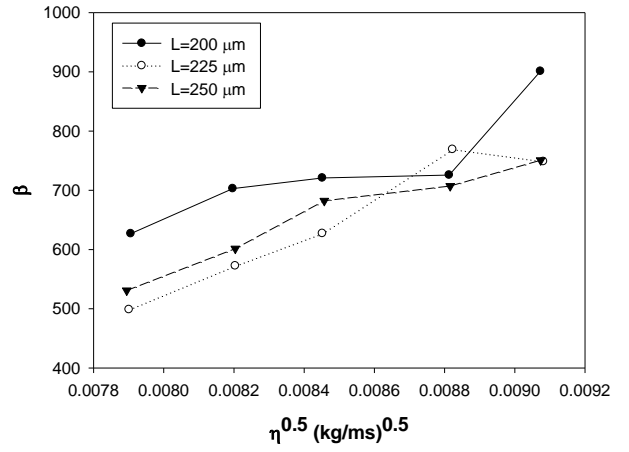


Figure A.13:  $\beta$  vs  $\eta^{0.5}$  (liquid)

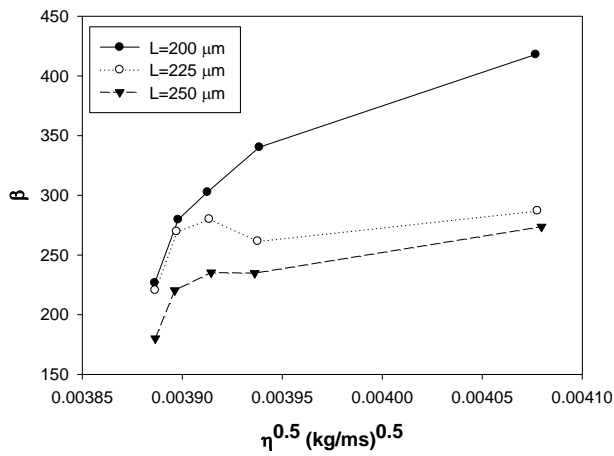


Figure A.14:  $\beta$  vs  $\eta^{0.5}$  (gas)



A.3.2 Results at T=35 °C

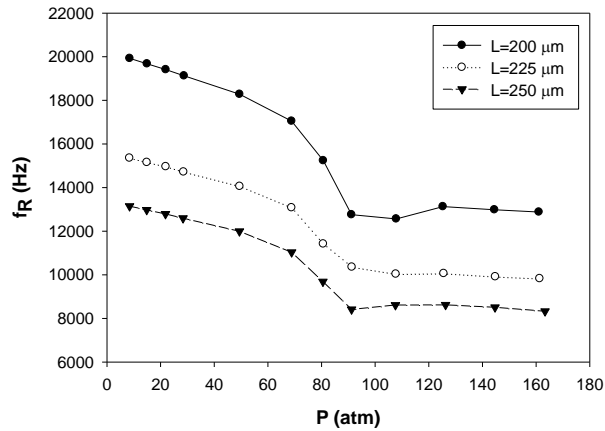


Figure A.15:  $f_R$  vs P

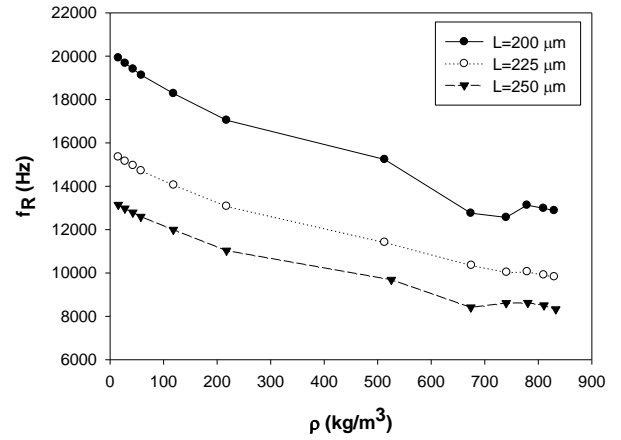


Figure A.16:  $f_R$  vs  $\rho$

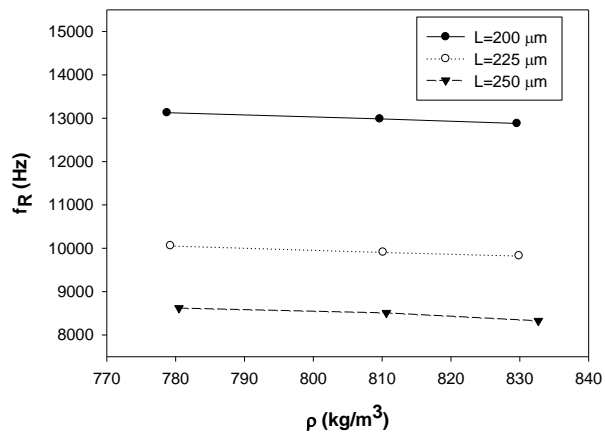


Figure A.17:  $f_R$  vs  $\rho$  (sc, excluding drift)

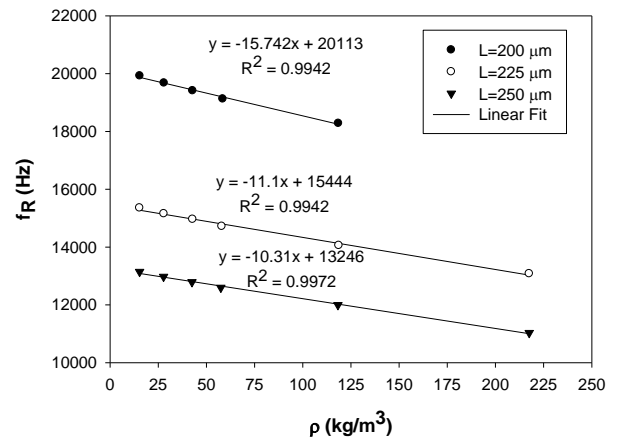


Figure A.18:  $f_R$  vs  $\rho$  (gas, ex. dr.)

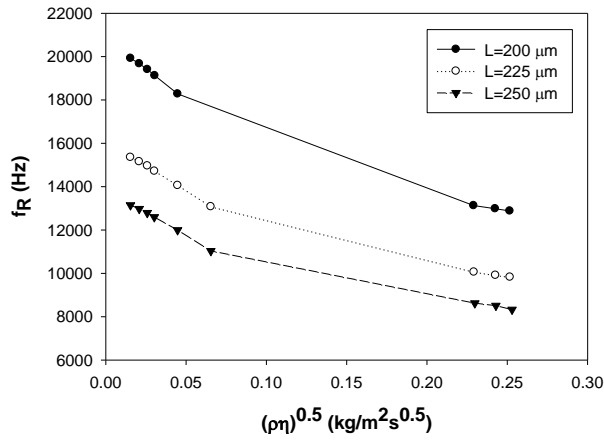


Figure A.19:  $f_R$  vs  $(\rho\eta)^{0.5}$  (ex. dr.)

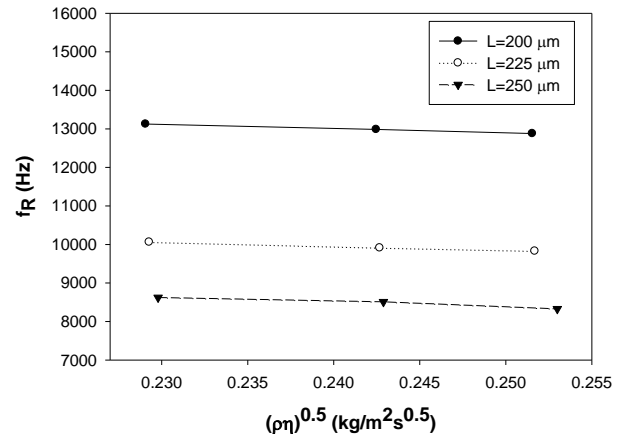


Figure A.20:  $f_R$  vs  $(\rho\eta)^{0.5}$  (sc, ex. dr.)

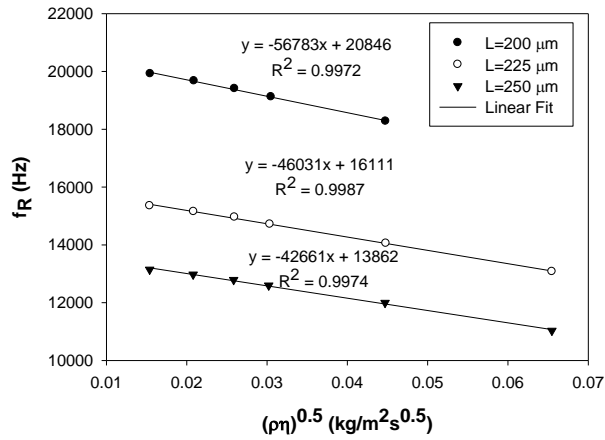


Figure A.21:  $f_R$  vs  $(\rho\eta)^{0.5}$  (gas, ex. dr.)

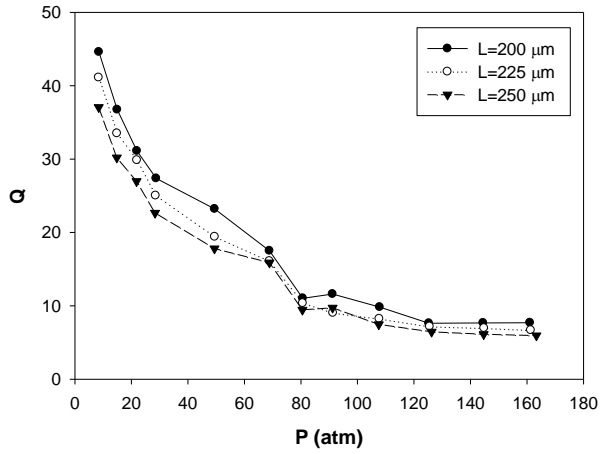


Figure A.22: Q vs P

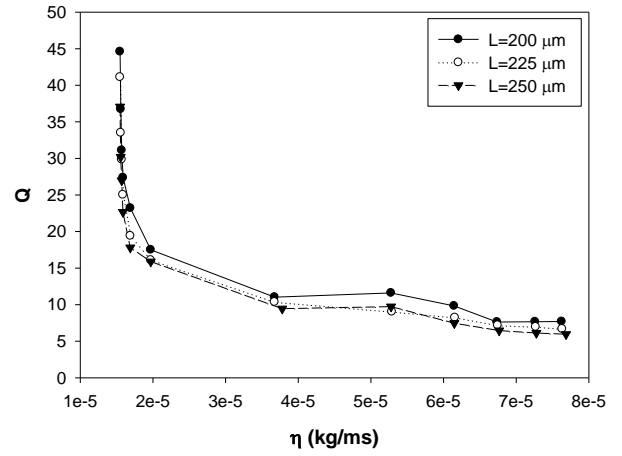


Figure A.23: Q vs  $\eta$

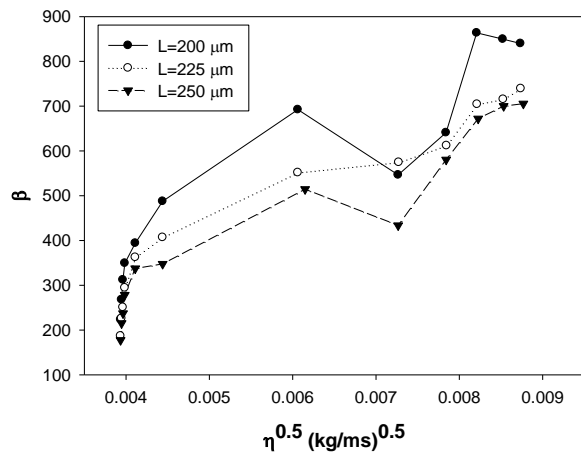


Figure A.24:  $\beta$  vs  $\eta^{0.5}$

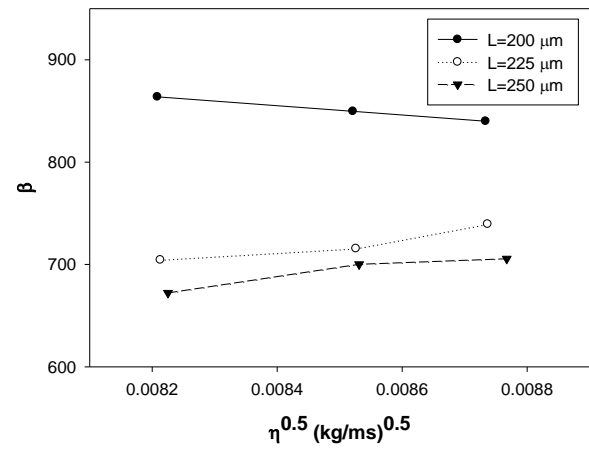
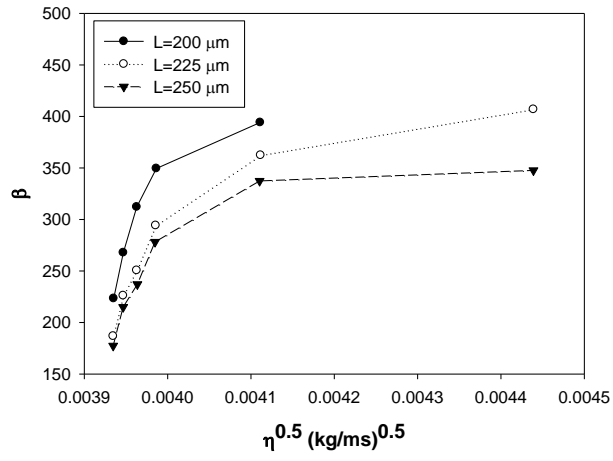
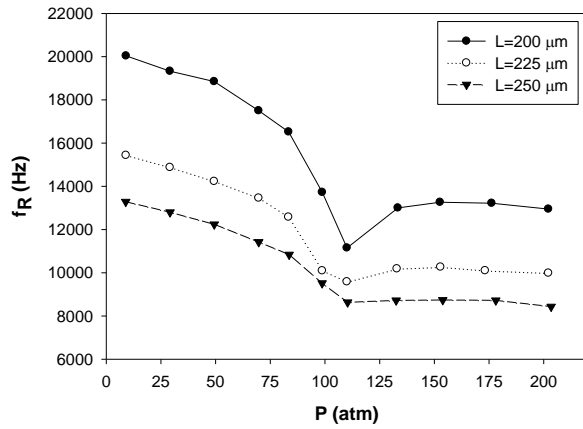


Figure A.25:  $\beta$  vs  $\eta^{0.5}$  (sc, ex. dr.)



**Figure A.26:**  $\beta$  vs  $\eta^{0.5}$  (gas, ex. dr.)

**A.3.3 Results at T=45 °C**



**Figure A.27:  $f_R$  vs P**

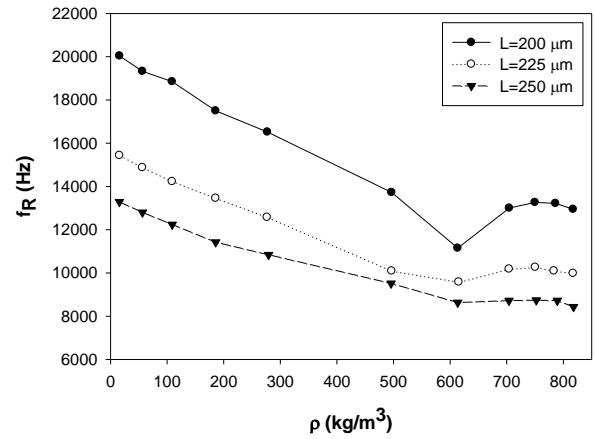


**Figure A.28:  $f_R$  vs  $\rho$**

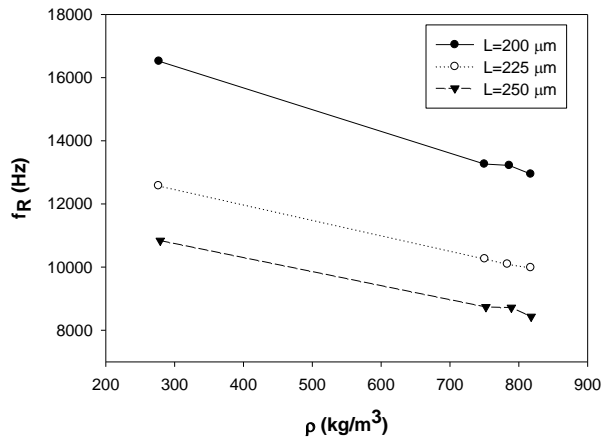


**Figure A.29:  $f_R$  vs  $\rho$  (sc, ex. dr.)**

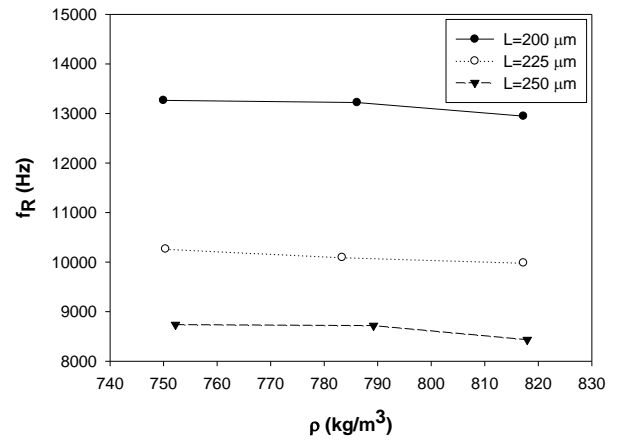


**Figure A.30:  $f_R$  vs  $\rho$  (sc, ex. & after dr.)**

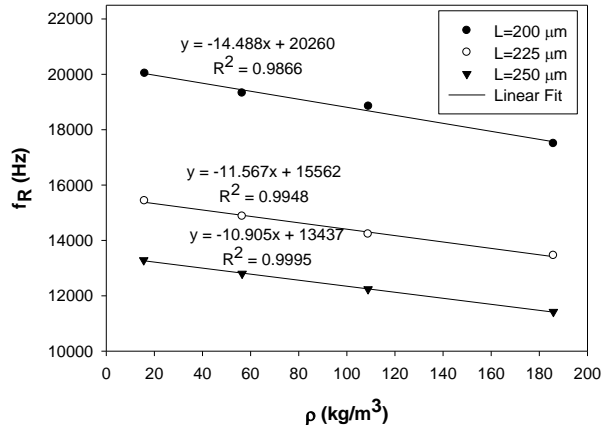


Figure A.31:  $f_R$  vs  $\rho$  (gas, ex. dr.)

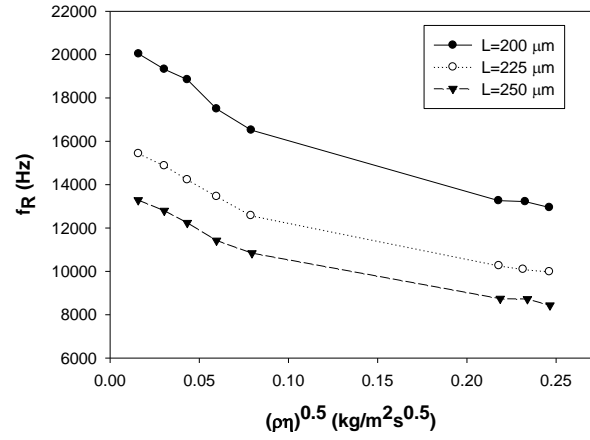


Figure A.32:  $f_R$  vs  $(\rho\eta)^{0.5}$  (ex. dr.)

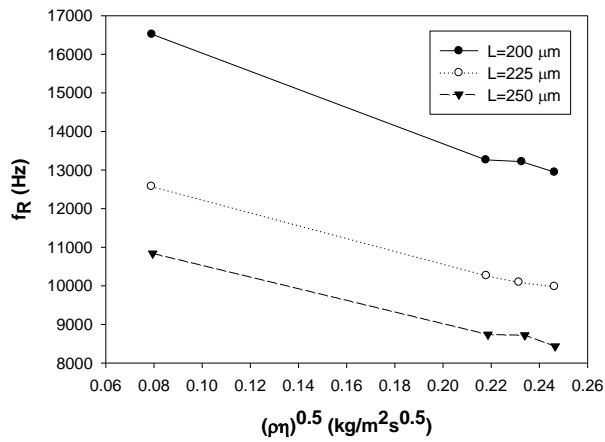


Figure A.33:  $f_R$  vs  $(\rho\eta)^{0.5}$  (sc, ex. dr.)

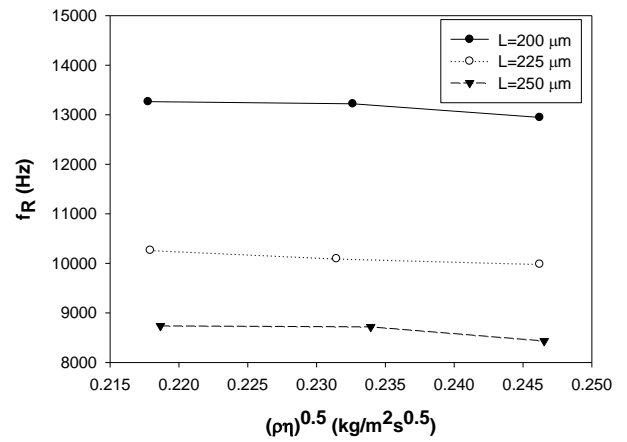


Figure A.34:  $f_R$  vs  $(\rho\eta)^{0.5}$  (sc, ex. & af. dr.)

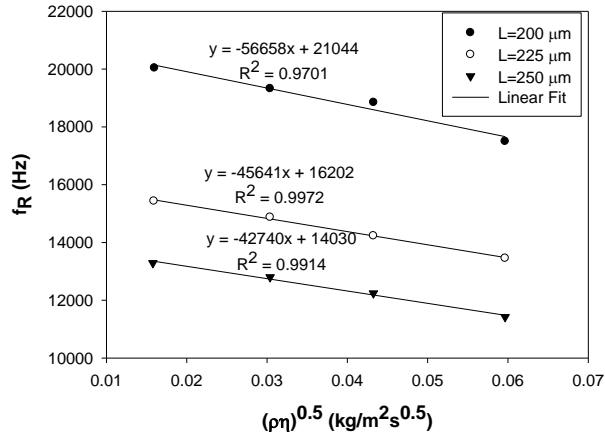


Figure A.35:  $f_R$  vs  $(\rho\eta)^{0.5}$  (gas, ex. dr.)

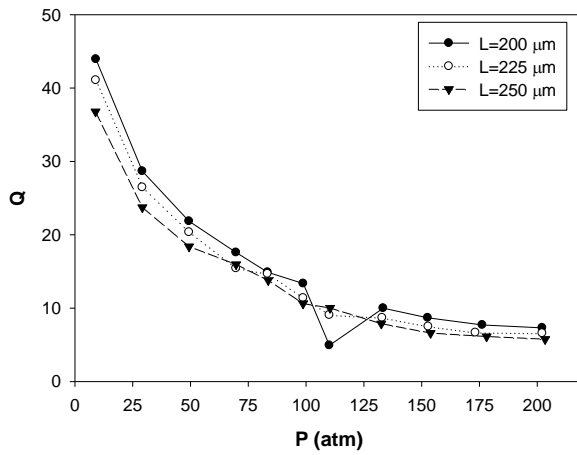


Figure A.36:  $Q$  vs  $P$

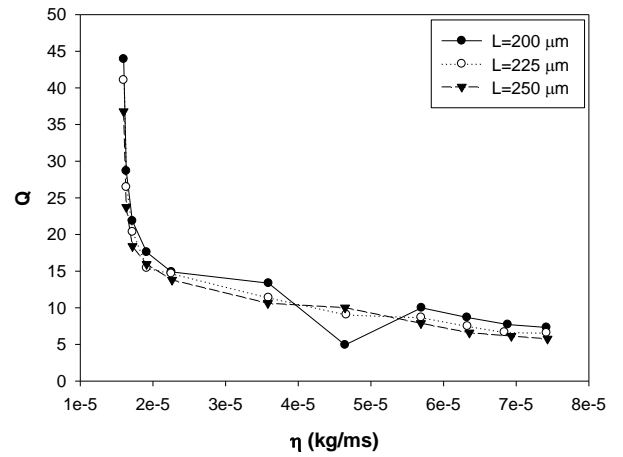


Figure A.37:  $Q$  vs  $\eta$

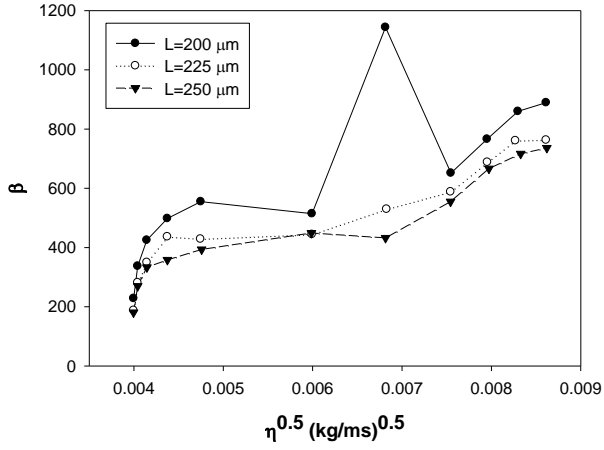


Figure A.38:  $\beta$  vs  $\eta^{0.5}$

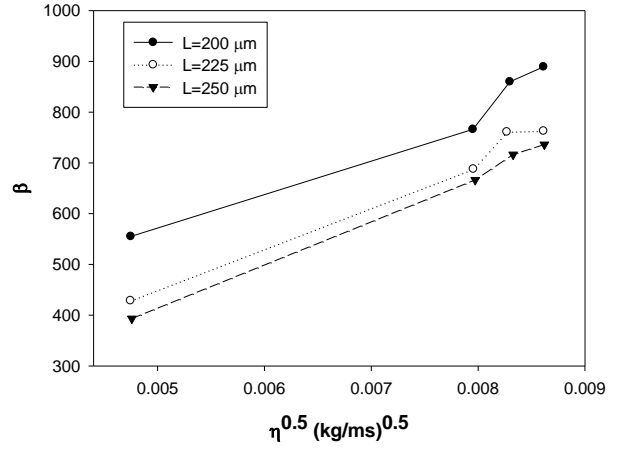


Figure A.39:  $\beta$  vs  $\eta^{0.5}$  (sc, ex. dr.)

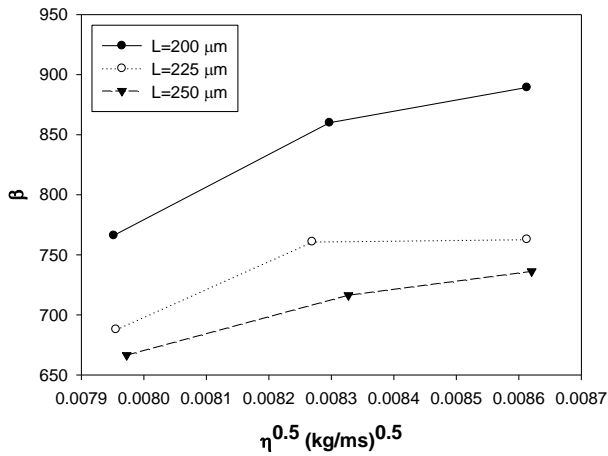


Figure A.40:  $\beta$  vs  $\eta^{0.5}$  (sc, ex. & af. dr.)

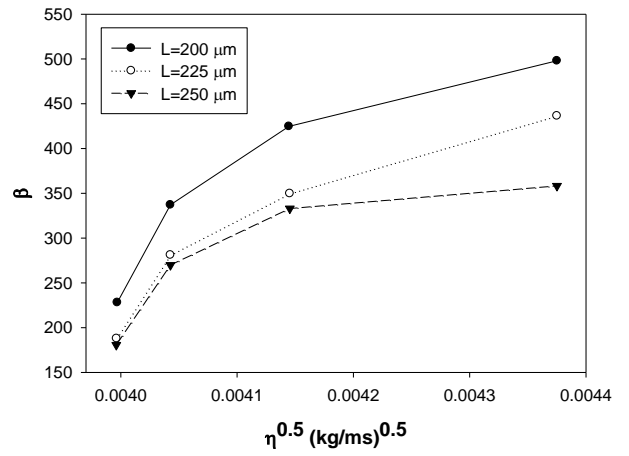


Figure A.41:  $\beta$  vs  $\eta^{0.5}$  (gas, ex. dr.)



A.3.4 Results at T=55 °C

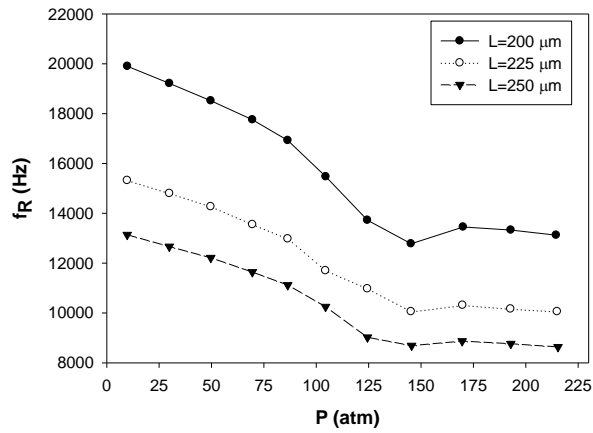


Figure A.42:  $f_R$  vs P

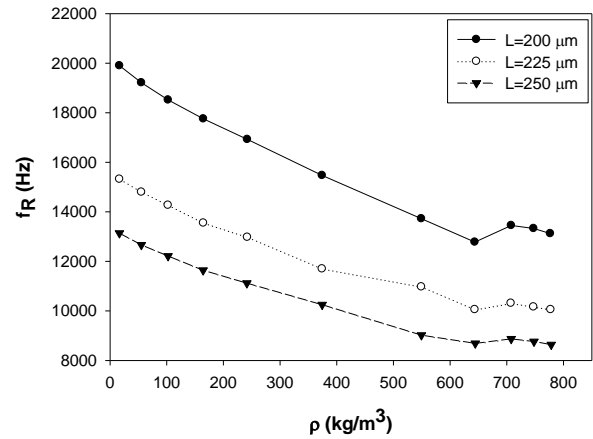


Figure A.43:  $f_R$  vs  $\rho$

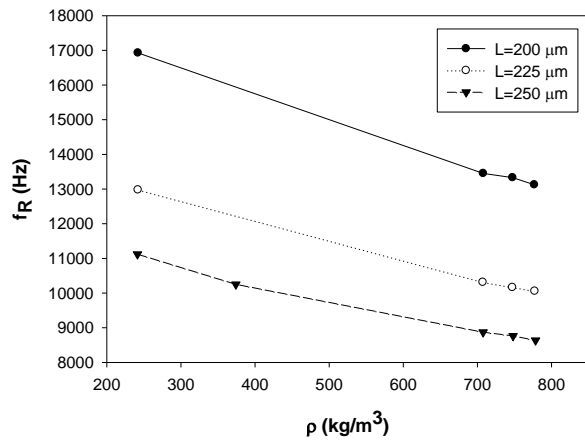


Figure A.44:  $f_R$  vs  $\rho$  (sc, ex. dr.)

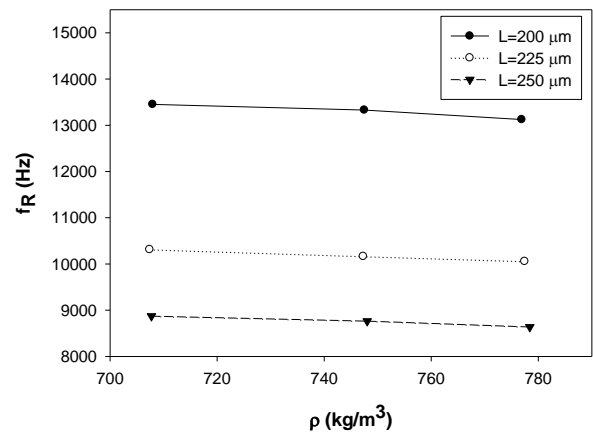


Figure A.45:  $f_R$  vs  $\rho$  (sc, ex. & af. dr.)

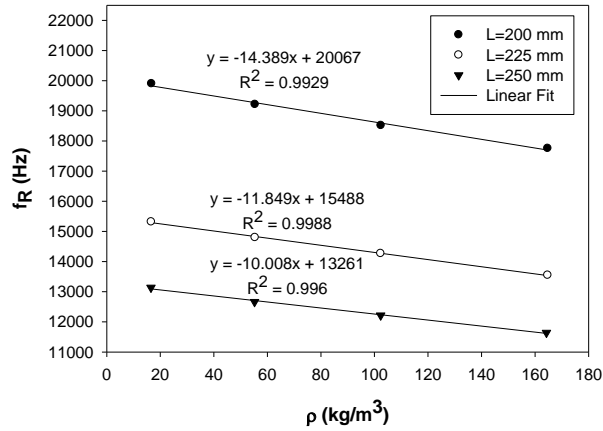


Figure A.46:  $f_R$  vs  $\rho$  (gas, ex. dr.)

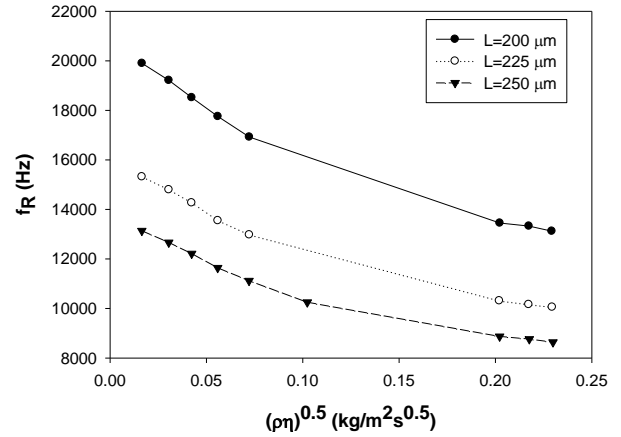


Figure A.47:  $f_R$  vs  $(\rho\eta)^{0.5}$  (ex. dr.)

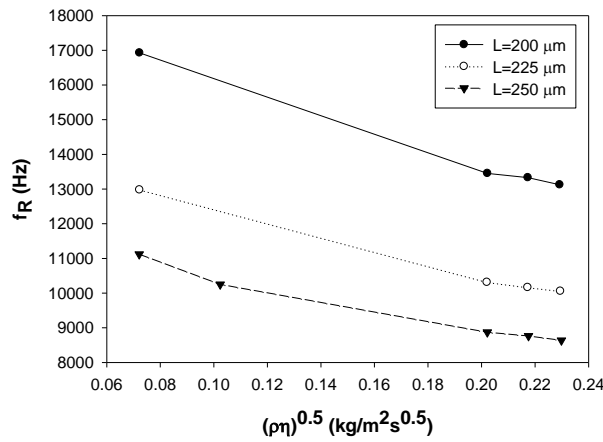


Figure A.48:  $f_R$  vs  $(\rho\eta)^{0.5}$  (sc, ex. dr.)

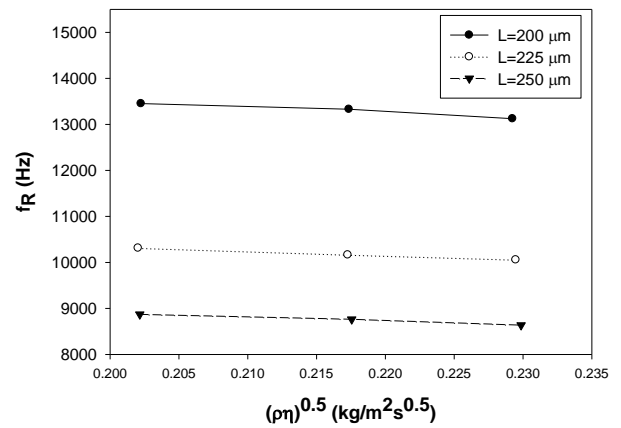


Figure A.49:  $f_R$  vs  $(\rho\eta)^{0.5}$  (sc, ex. & af. dr.)

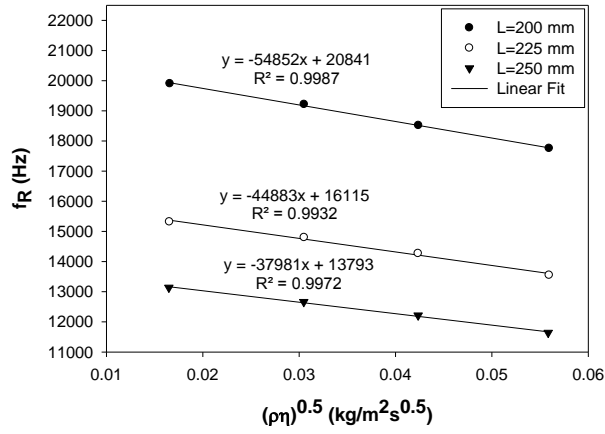


Figure A.50:  $f_R$  vs  $(\rho\eta)^{0.5}$  (gas, ex. dr.)

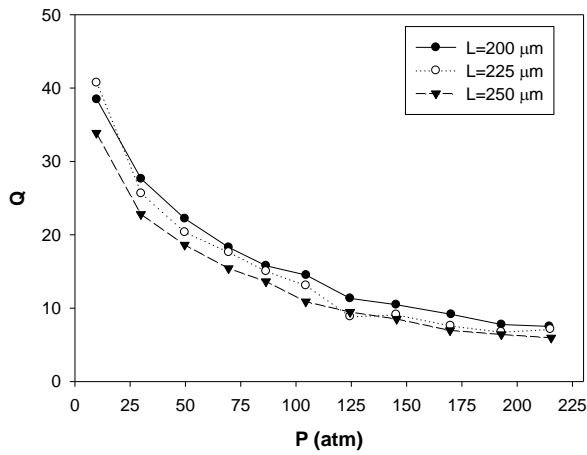


Figure A.51: Q vs P

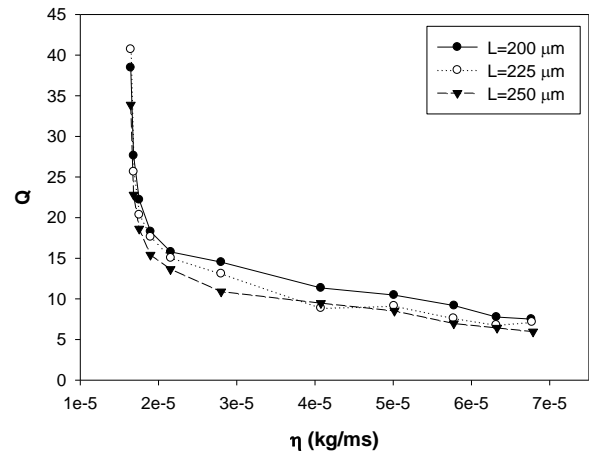


Figure A.52: Q vs  $\eta$

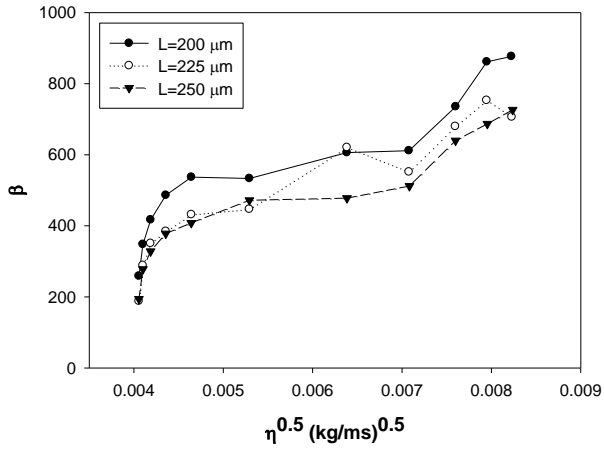


Figure A.53:  $\beta$  vs  $\eta^{0.5}$

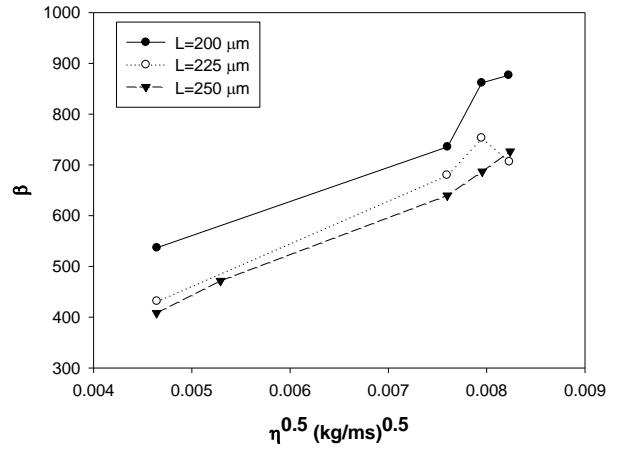


Figure A.54:  $\beta$  vs  $\eta^{0.5}$  (sc, ex. dr.)

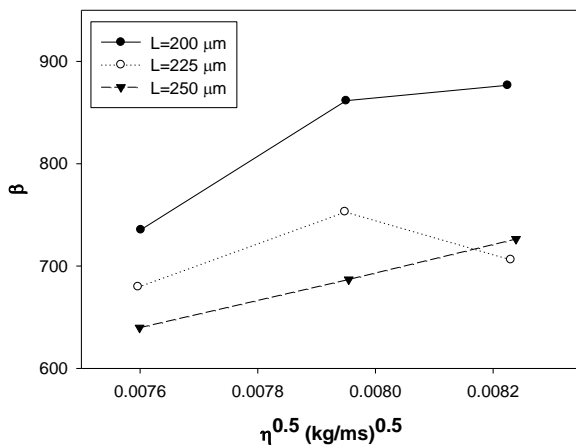


Figure A.55:  $\beta$  vs  $\eta^{0.5}$  (sc, ex. & af. dr.)

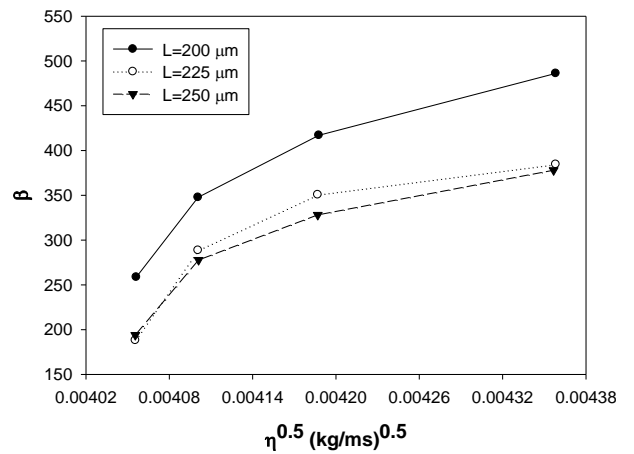
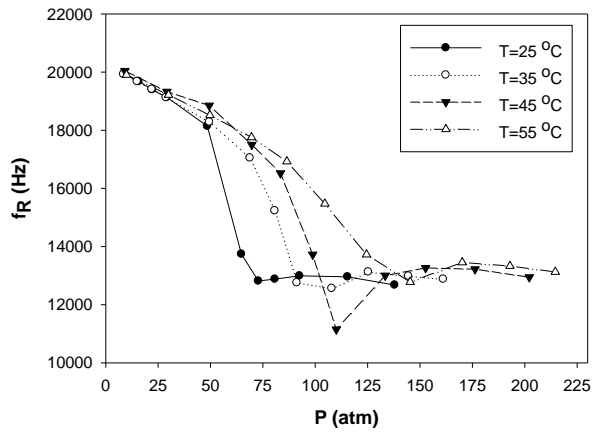
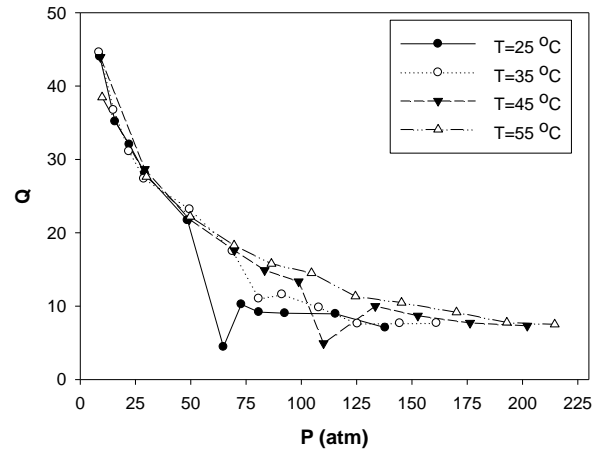


Figure A.56:  $\beta$  vs  $\eta^{0.5}$  (gas, ex. dr.)

**A.3.5 Results for  $L=200 \mu\text{m}$**



**Figure A.57:  $f_R$  vs P**



**Figure A.58: Q vs P**

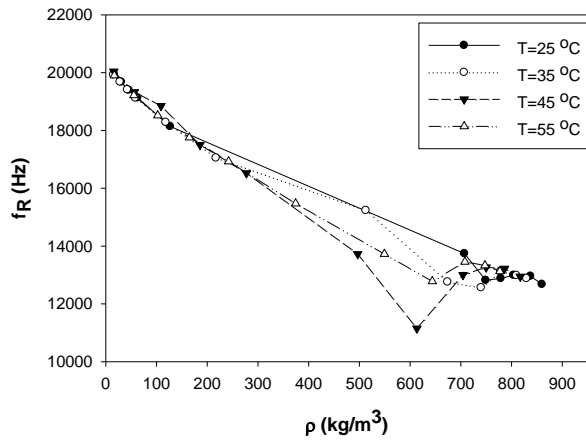


**Figure A.59:  $f_R$  vs  $\rho$**

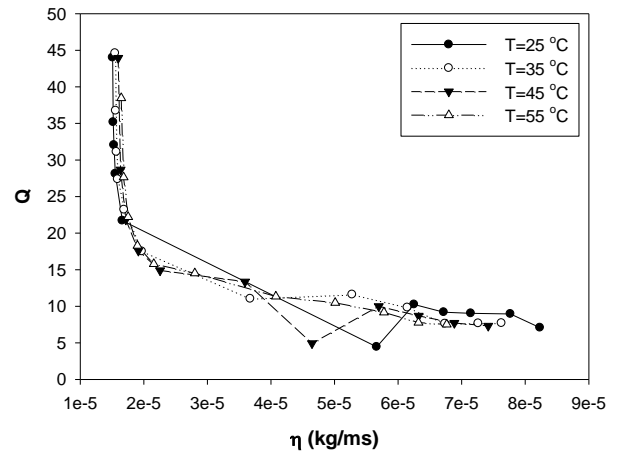


**Figure A.60: Q vs  $\eta$**

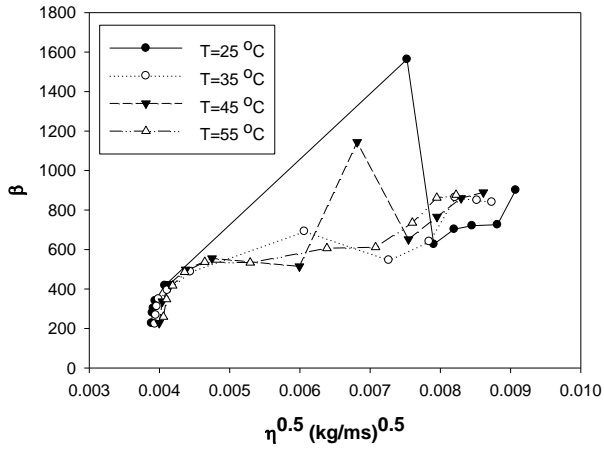


**Figure A.61:**  $\beta$  vs  $\eta^{0.5}$

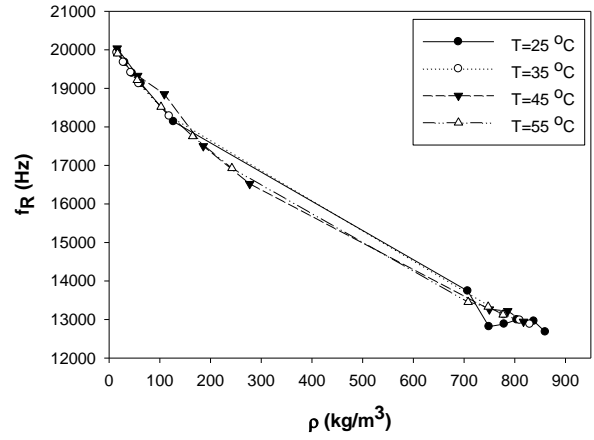


**Figure A.62:**  $f_R$  vs  $\rho$  (ex. dr.)

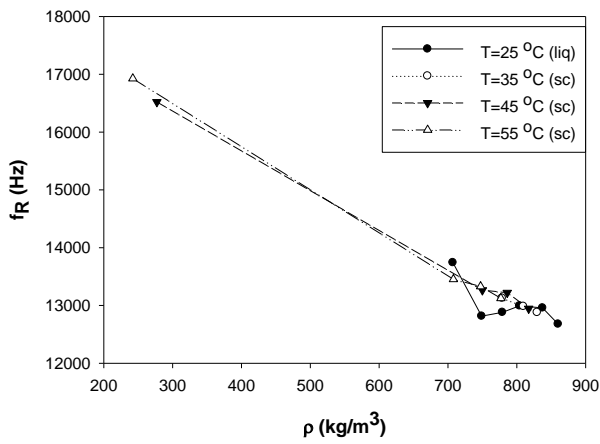


**Figure A.63:**  $f_R$  vs  $\rho$  (liq. + sc, ex. dr.)

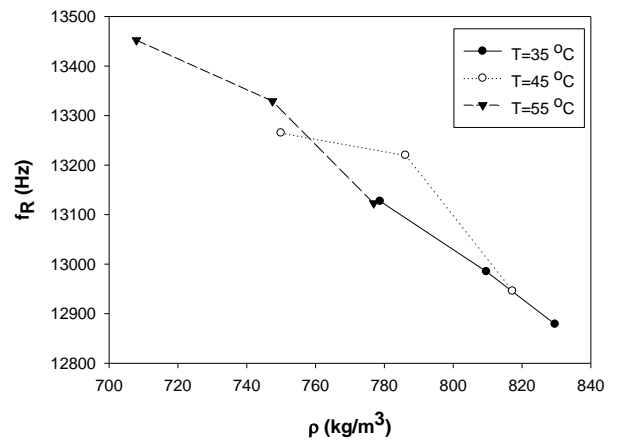


**Figure A.64:**  $f_R$  vs  $\rho$  (sc, ex. & af. dr.)

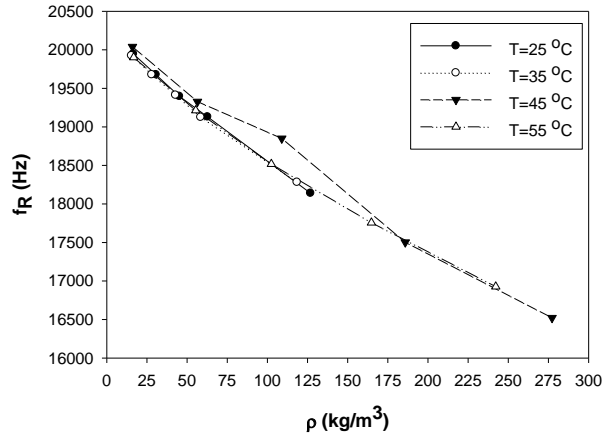


Figure A.65:  $f_R$  vs  $\rho$  (gas, ex. dr.)

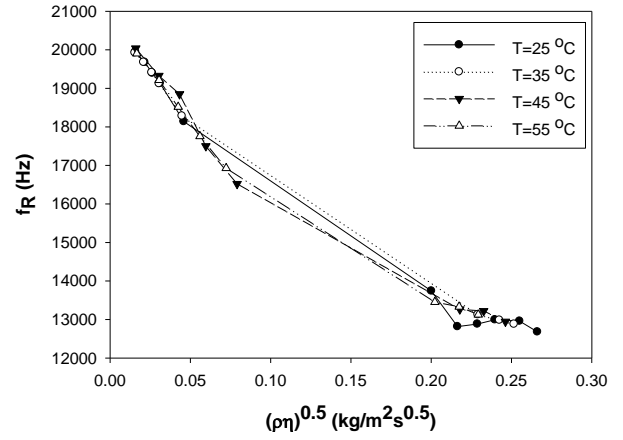


Figure A.66:  $f_R$  vs  $(\rho\eta)^{0.5}$  (ex. dr.)

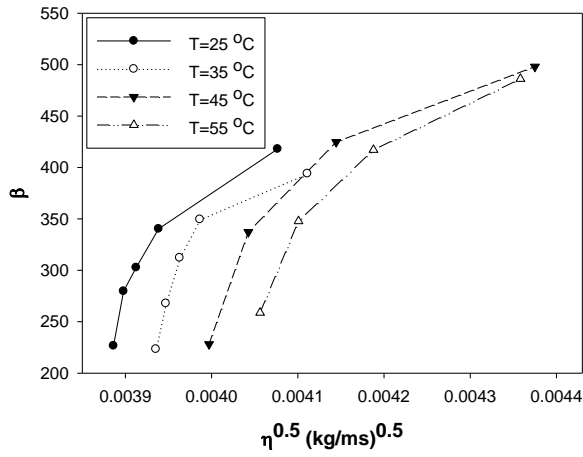


Figure A.67:  $\beta$  vs  $\eta^{0.5}$  (gas, ex. dr.)

A.3.6 Results for  $L=225 \mu\text{m}$

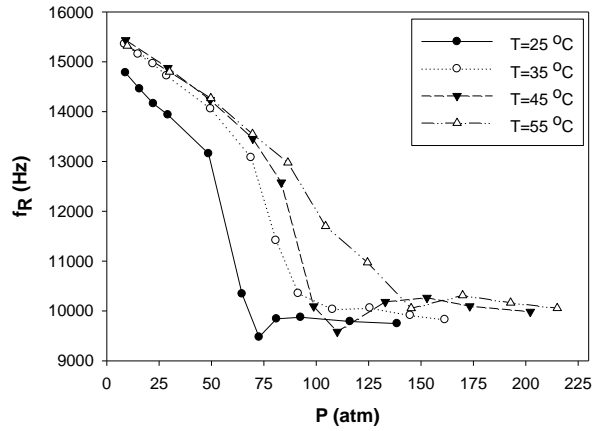


Figure A.68:  $f_R$  vs P

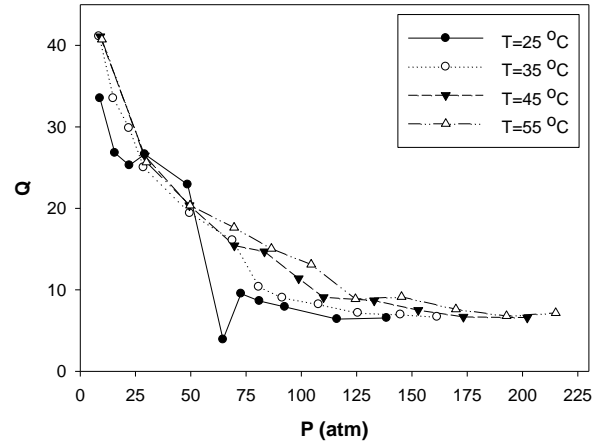


Figure A.69: Q vs P

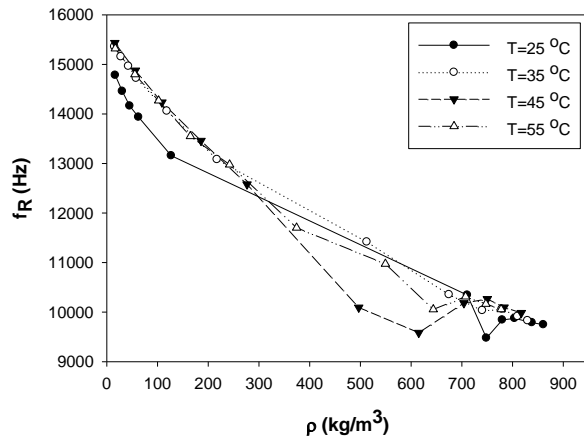


Figure A.70:  $f_R$  vs  $\rho$

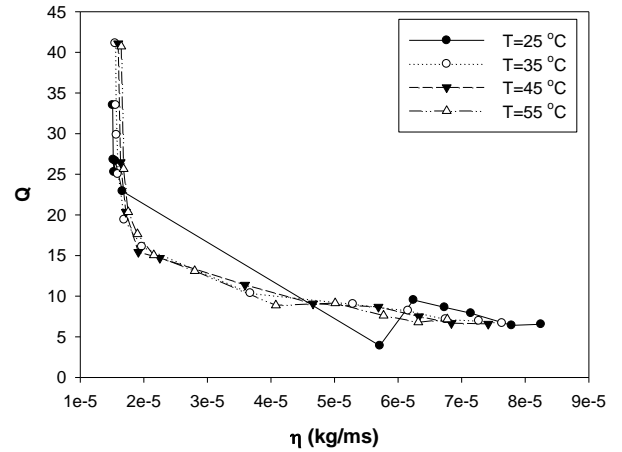


Figure A.71: Q vs  $\eta$



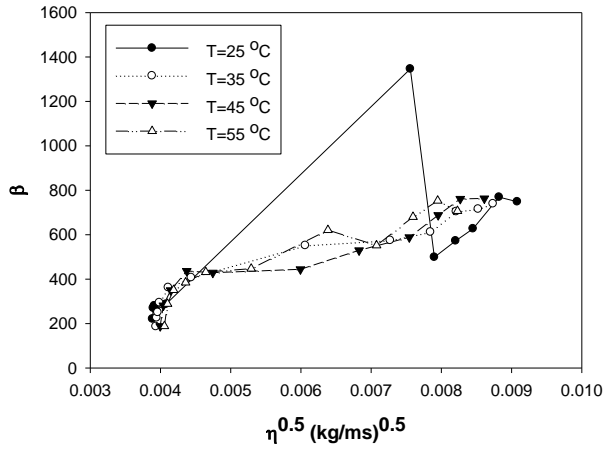


Figure A.72:  $\beta$  vs  $\eta^{0.5}$

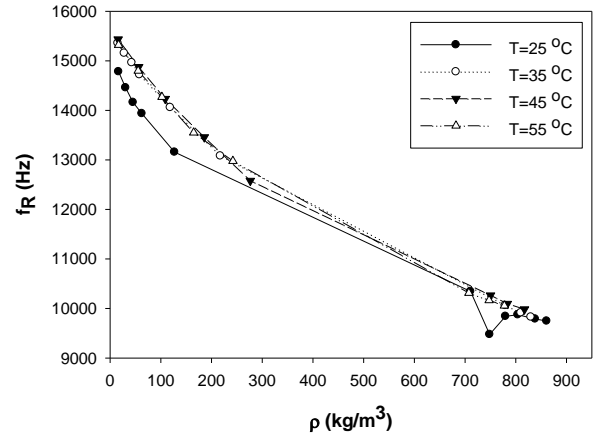


Figure A.73:  $f_R$  vs  $\rho$  (ex. dr.)

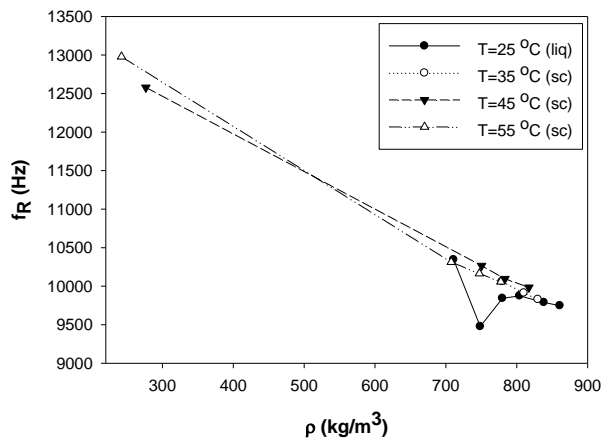


Figure A.74:  $f_R$  vs  $\rho$  (liq. + sc, ex. dr.)

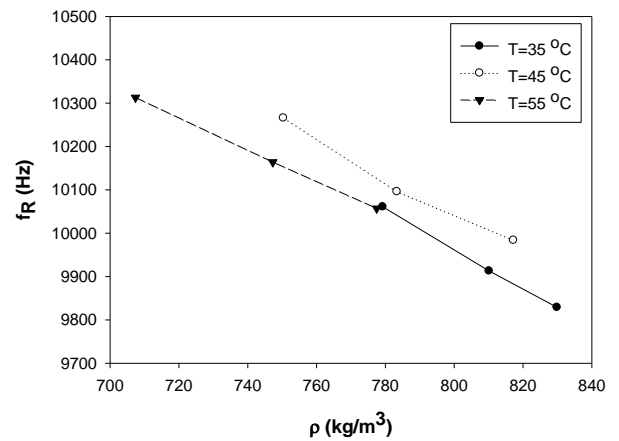


Figure A.75:  $f_R$  vs  $\rho$  (sc, ex. & af. dr.)

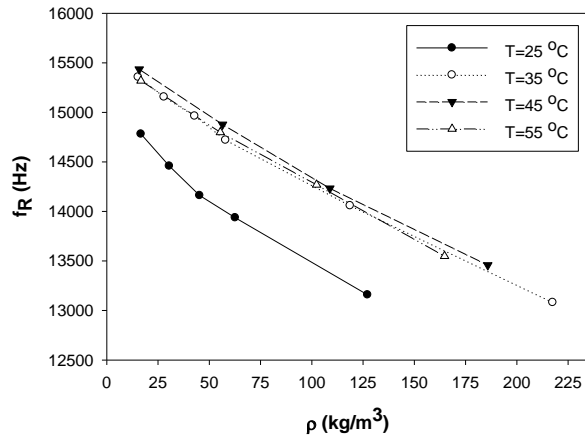


Figure A.76:  $f_R$  vs  $\rho$  (gas, ex. dr.)

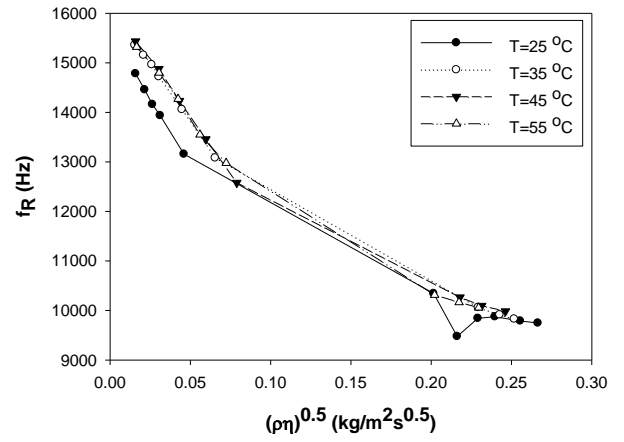


Figure A.77:  $f_R$  vs  $(\rho\eta)^{0.5}$  (ex. dr.)

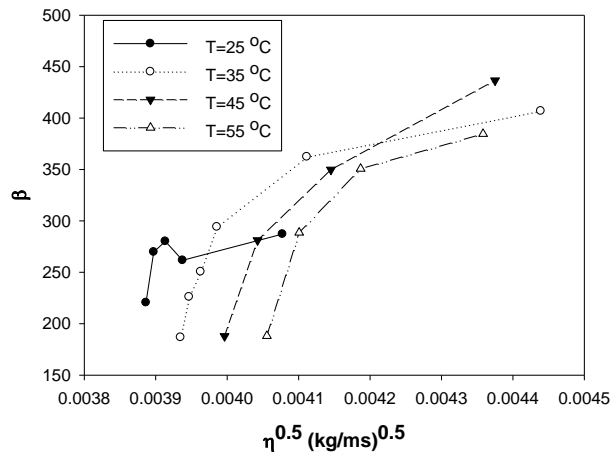
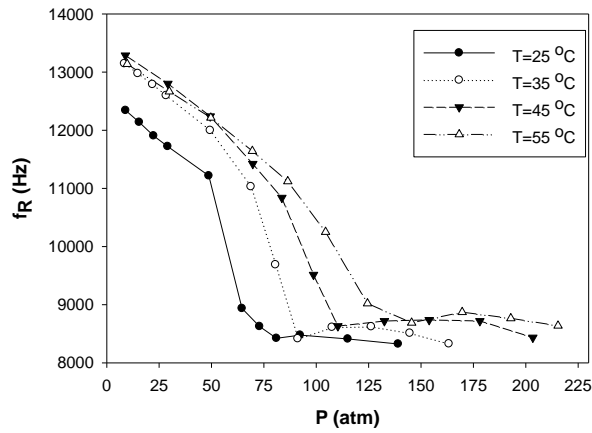
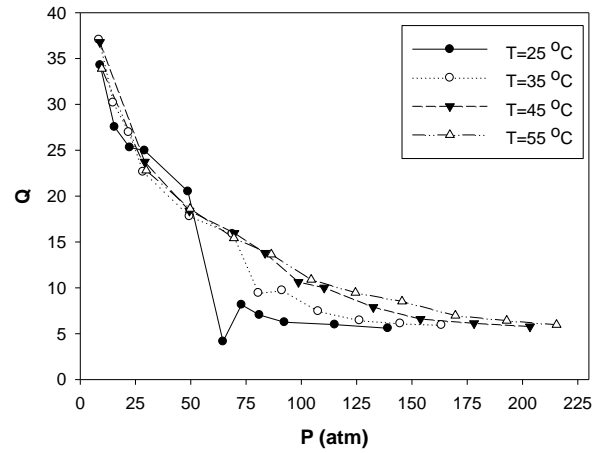


Figure A.78:  $\beta$  vs  $\eta^{0.5}$  (gas, ex. dr.)

**A.3.7 Results for L=250  $\mu\text{m}$**



**Figure A.79:  $f_R$  vs P**



**Figure A.80: Q vs P**

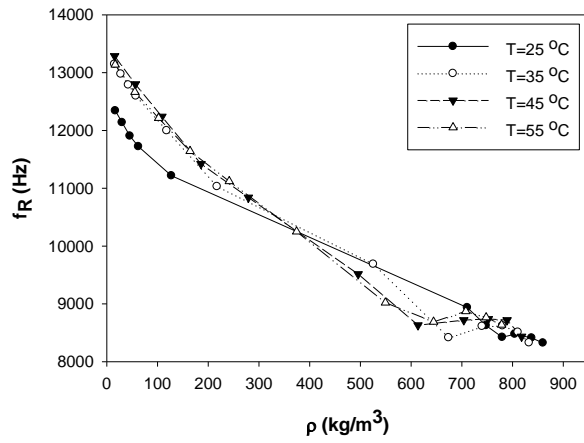


**Figure A.81:  $f_R$  vs  $\rho$**

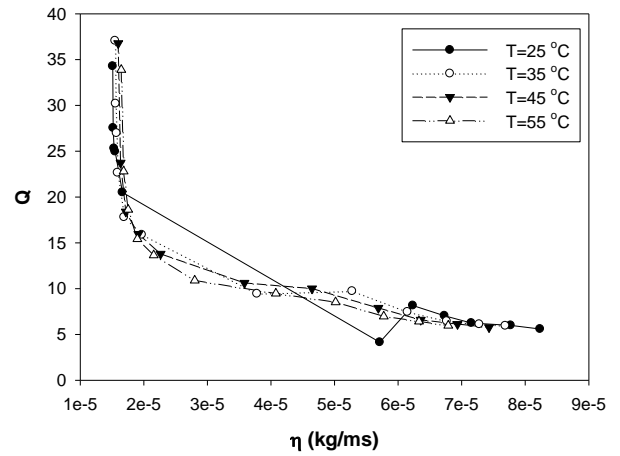


**Figure A.82: Q vs  $\eta$**

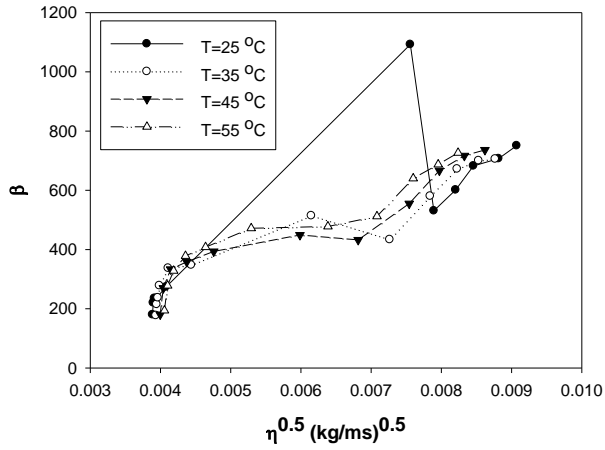


**Figure A.83:**  $\beta$  vs  $\eta^{0.5}$

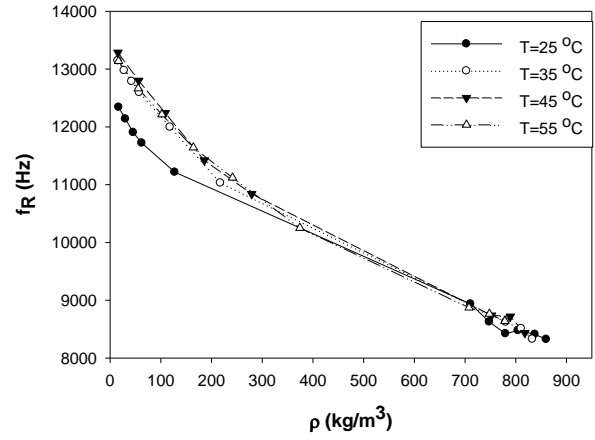


**Figure A.84:**  $f_R$  vs  $\rho$  (ex. dr.)

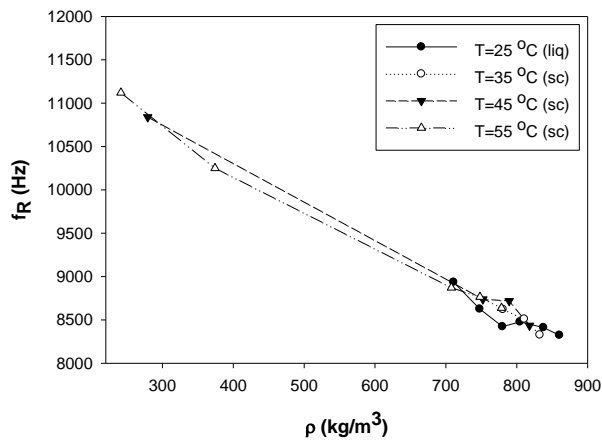


**Figure A.85:**  $f_R$  vs  $\rho$  (liq. + sc, ex. dr.)

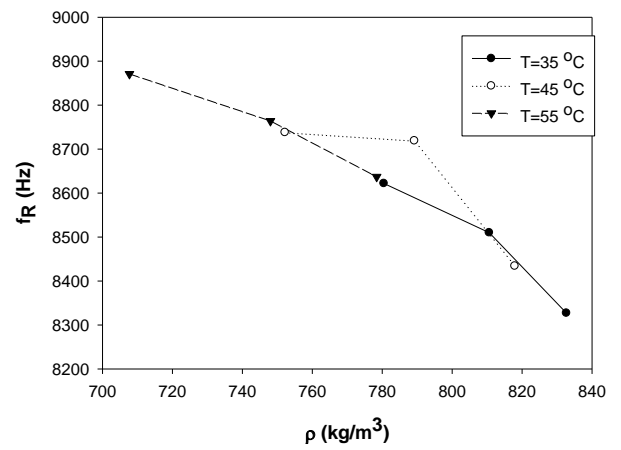


**Figure A.86:**  $f_R$  vs  $\rho$  (sc, ex. & af. dr.)

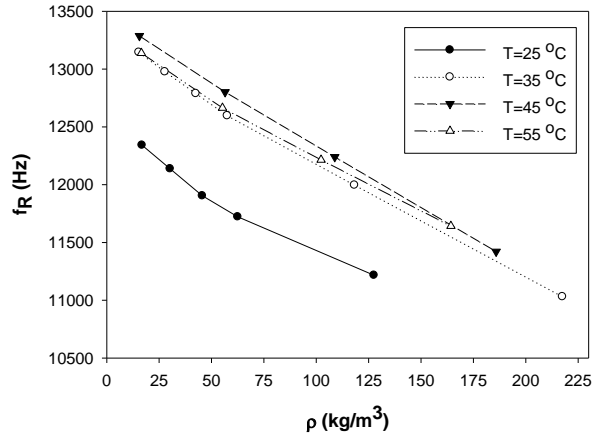


Figure A.87:  $f_R$  vs  $\rho$  (gas, ex. dr.)

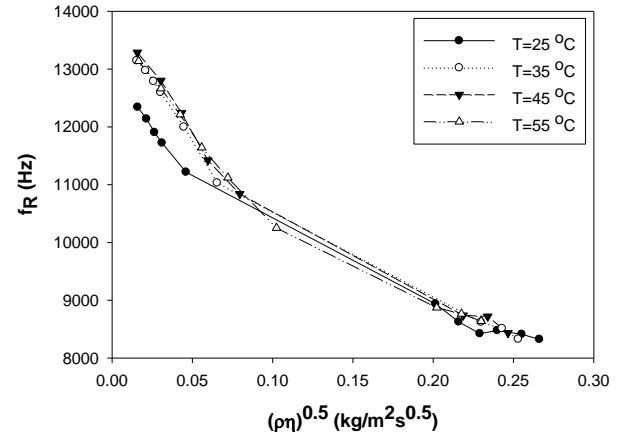


Figure A.88:  $f_R$  vs  $(\rho\eta)^{0.5}$  (ex. dr.)

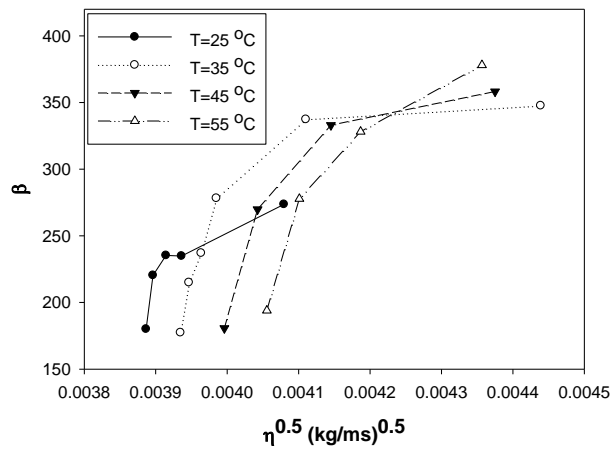


Figure A.89:  $\beta$  vs  $\eta^{0.5}$  (gas, ex. dr.)

#### A.4 CO<sub>2</sub> Compressibility Calculation

In order to calculate the compressibility of CO<sub>2</sub>, the pressure and density data at T=25 °C, T=35 °C and T=55 °C acquired from [48] are fitted to a 5<sup>th</sup> order polynomial. The reciprocal of the derivative of the polynomial gives the “denormalized compressibility” as shown in Equation A.1,

$$-\rho K_T = \left( \frac{\partial \rho}{\partial P} \right)_T \quad (\text{A.1})$$

The pressure versus density plots and the polynomial fit equations with the corresponding R<sup>2</sup> values for T=35 °C, T=45 °C and T=55 °C are given in Figure A.90-92.

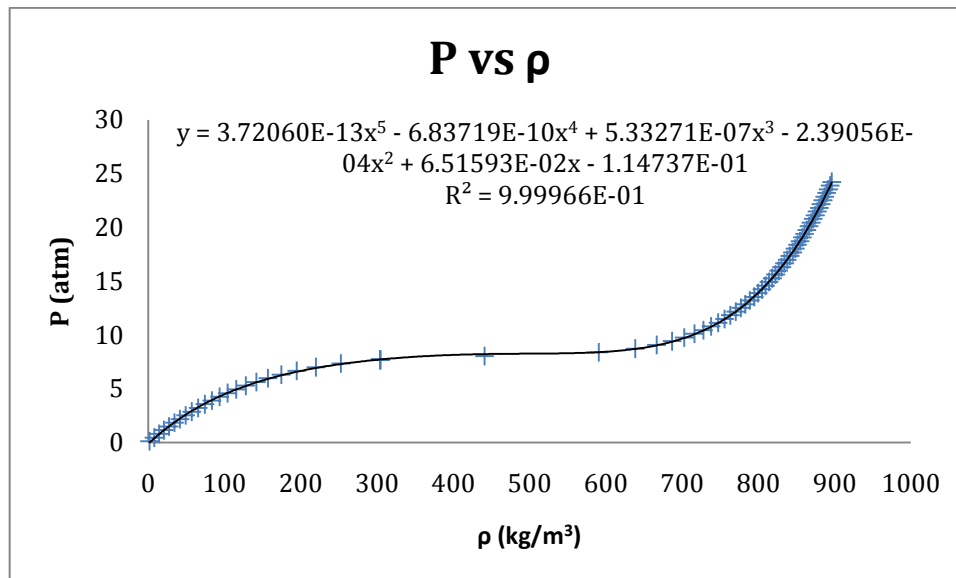


**Figure A.90:** P vs ρ at T=35 °C

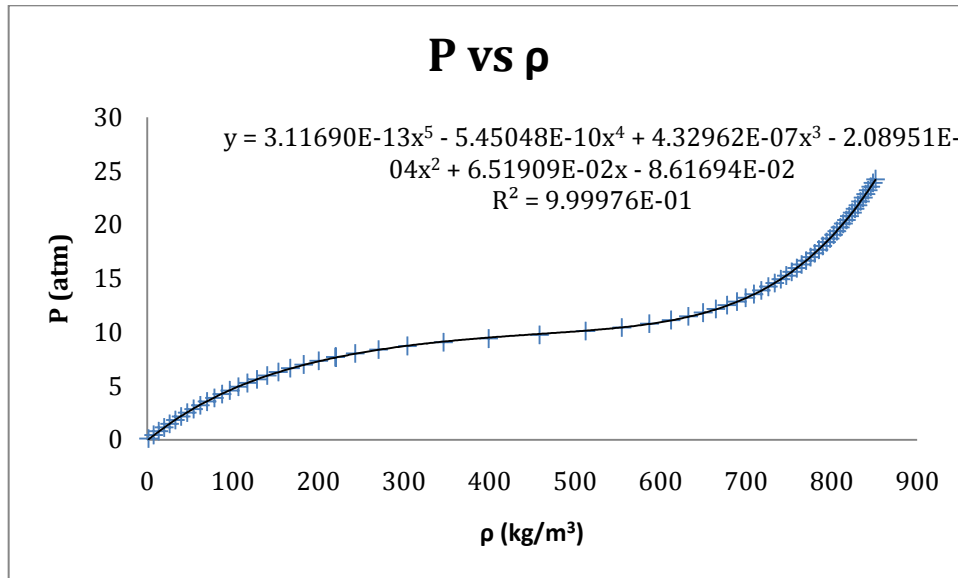


**Figure A.91: P vs  $\rho$  at T=45 °C**

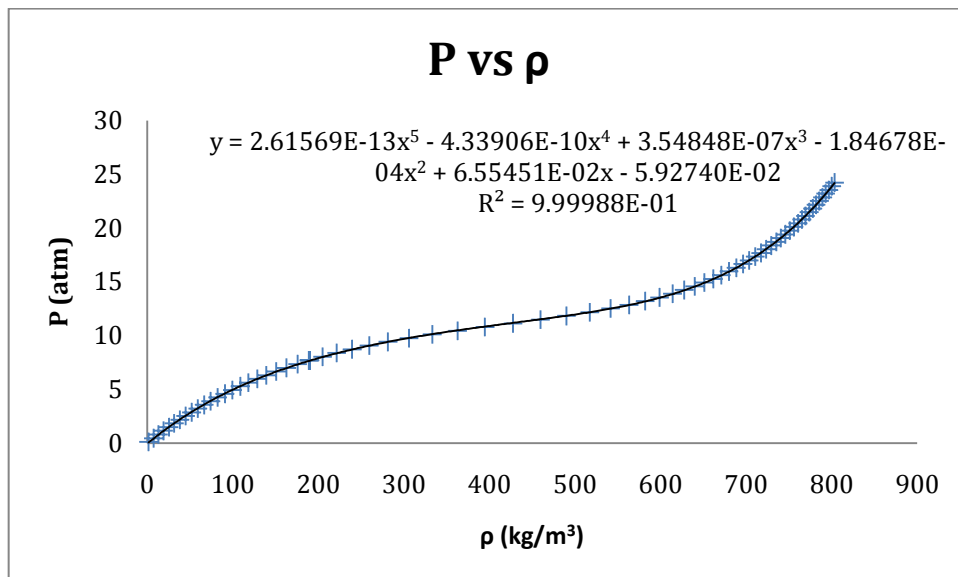


**Figure A.92: P vs  $\rho$  at T=55 °C**

---

The average of calculated denormalized compressibility values for each data point at each temperature are given in Table A.13.

**Table A.13:** Average  $-\rho K_{Tavg}$  values at experimental data points

$-\rho K_{Tavg} (s^2/m^2)$		
T=35 °C	T=45 °C	T=55 °C
17.18	16.98	16.75
18.87	22.05	20.80
21.08	30.78	26.90
23.64	49.38	37.29
37.33	84.13	54.35
77.68	173.78	90.12
1754.01	66.13	65.49
61.45	27.10	32.73
26.93	17.82	19.92
17.85	13.26	14.76
13.33	10.36	11.89
11.10		



---

## A.5 Written MATLAB Codes

### A.5.1 Code for Data Acquisition

#### *daqscript.m*

```
clear all;
clc
close all;
format long;

%% reset signal generator
sg=gplib('ni',0,10);
fopen(sg);

% reset oscilloscope
os=gplib('ni',0,15);
fopen(os);
fprintf(os,'SELECT:CONTROL CH2');

mainfolder='C:\Documents and Settings\Administrator\My
Documents\MATLAB\olcum\';
subfolder='22-8\';
folder=[mainfolder,subfolder];
file='co2 t33-6 p-970 12x180 6 n3 try14';

%% measurements settings
amp = 2;
center = 46000;
delta = 7000;
delta2 = 3400;
startfreq = center-delta;
stopfreq = center+delta2;
step = 100;
ave_n = 500; % number of averages
pause_n = ave_n/startfreq;
scale_ver = 0.2; % 1; % scale of CH1: Volts/div
scale_hor = round(1e5/center)*4e-6; % horizontal scale: Secs/div

ref = startfreq:step:stopfreq;
N = 3;

%% initiliaze signal generator for measurement
fprintf(sg,'FUNC SIN');
fprintf(sg,'VOLT:UNIT VPP');
fprintf(sg,['VOLT ',num2str(amp)]);
```

---

```

fprintf(sg, ['FREQ ', num2str(startfreq)]); % update frequency
fprintf(sg, 'OUTP ON')

%% initiliazze oscilloscope for measurement
fprintf(os, 'MEASUREMENT:IMMED:SOURCE CH1');
fprintf(os, 'MEASUREMENT:IMMED:SOURCE2 CH2');
fprintf(os, 'AUTOSET EXECUTE');
fprintf(os, 'TRIGGER:MAIN:EDGE:SOURCE CH2');
fprintf(os, 'TRIGGER:MAIN:EDGE:COUPLING AC');
fprintf(os, ['ACQUIRE:NUMAVG ', num2str(ave_n)]);
fprintf(os, 'ACQUIRE:MOD AVE');
fprintf(os, ['HORIZONTAL:MAIN:SECDIV ', num2str(scale_hor)]);
fprintf(os, 'CH1:COUPLING AC');
fprintf(os, 'CH2:COUPLING AC');
fprintf(os, 'CH1:POSITION 0');
fprintf(os, ['CH1:SCALE ', num2str(scale_ver)]);

pause(1);

count = 1;

for i = startfreq:step:stopfreq

    fprintf(sg, ['FREQ ', num2str(i)]); % update frequency

    for j = 1:N

        % measure duty-cycle N times and take average
        fprintf(os, 'MEASUREMENT:IMMED:TYPE PK2PK')
        fprintf(os, 'MEASUREMENT:IMMED:VALUE?')
        temppk2pk(j) = fscanf(os, '%f');

        % measure phase N times and take average
        fprintf(os, 'MEASUREMENT:IMMED:TYPE PHA')
        fprintf(os, 'MEASUREMENT:IMMED:VALUE?')
        temppha(j) = fscanf(os, '%f');

    end

    vel(count) = mean(temppk2pk);
    pha(count) = mean(temppha);

    count = count + 1;
end

%reset all devices and close the gpib session
wR=mean(ref(round(find(max(vel)==vel))));

```

---

```

fprintf(sg, ['FREQ ', num2str(wR)]); % update frequency
fprintf(os, ['ACQUIRE:NUMAVG ', num2str(20)]);
fclose(sg);
clear sg;
fclose(os);
clear os;

filename=[folder, file];

plot(ref(30:((stopfreq-startfreq)/step+1)), pha(30:((stopfreq-
startfreq)/step+1)));
xlabel('Frequency [Hz]');
ylabel('Phase [deg]');
saveas(gcf, [filename, 'p'], 'fig')

figure, plot(ref(30:((stopfreq-startfreq)/step+1)), vel(30:((stopfreq-
startfreq)/step+1)));
xlabel('Frequency [Hz]');
ylabel('Magnitude [V_19]');
saveas(gcf, filename, 'fig')

newmain
saveas(gcf, filename, 'png')
saveas(gcf, [filename, '-fit'], 'fig')

```

## A.5.2 Code for Lorentzian Fitting

### *newmain.m*

```

lh=findall(gcf, 'type', 'line');
xdata=get(lh, 'xdata') ./1000;
ydata=get(lh, 'ydata');

%% Lorentzian Model Function
newfun = inline('1000.*v(1).*v(2).^2./((x.^2-v(3)^2).^2 + (v(2).*x).^2)',
'v', 'x'); %/(2*pi)^2

%% For eliminating defects in the onset of ydata
originallength=length(xdata);
defectedlength=5;

xdata=xdata(defectedlength:originallength);
ydata=ydata(defectedlength:originallength) ./max(ydata(defectedlength:orig
inallength));

```

---

```
ydatasq=ydata.^2;

disp('# starting');

xx=xdata;
yy=ydatasq;
x=xx(1,:);
yOrig=yy(1,:);
figure;
plot(x,yOrig,'or');
hold on;

%% define start point
x0=xx(1);
y0=ydatasq(1);

imax=round(median(find(max(ydatasq)== ydatasq)));

ilinewidth=[min(find(ydatasq(imax)/sqrt(2)<= ydatasq))
max(find(ydatasq(imax)/sqrt(2)<= ydatasq))];

Linewidth=(xdata(ilinewidth(2))-xdata(ilinewidth(1)));

w0=xdata(imax);

Q=w0/Linewidth;

A=ydatasq(imax)*(w0^2/Q)^2;

vStart=[A,Linewidth,w0];

yStart=newfun(vStart,x);

fprintf('Start: A=%f b=%f Q=%f
w0=%f\n',vStart(1),vStart(2)/2,vStart(3)/vStart(2),vStart(3));

%% using nlinfit
[vEnd,resid,J]=nlinfit(x,yOrig,newfun,vStart);
yEnd=newfun(vEnd,x);
Q=vEnd(3)/vEnd(2);
beta=vEnd(2)/2;
w0=vEnd(3);
wR=sqrt(w0^2-2*beta^2);
y_label=ydatasq(imax)/sqrt(2);
```

---

```
fprintf('End: A=%f b=%f Q=%f wR=%f\n',vEnd(1),beta,Q,vEnd(3));
plot(x,yEnd,'-b','Linewidth',2);
text(vEnd(3),y_label,[' \bf{\it f_0 = ',num2str(ceil(w0*1000))},' Hz
\newline f_R = ',...
      num2str(ceil(wR*1000)),' Hz \newline Q = ',num2str(Q),' \newline
\beta = ',...

num2str(ceil(beta*1000)),'}'],'EdgeColor','black','BackgroundColor',[.75,
0.8,0.85],'Color',...
      'black','HorizontalAlignment','center','VerticalAlignment','bottom')
%
legend('Orig','Fit');

%% ending
disp('# ending');
```

---

### Bibliography

- [1] B. Ilic, D. Czaplewski, H.G. Craighead, P. Neuzil, C. Campagnolo, and C. Batt, Mechanical resonant immunospecific biological detector, *Applied Physics Letters*, 77 (2000), 450-452.
- [2] G. Muralidharan, A. Wig, L.A. Pinnaduwege, D. Hedden, T. Thundat, and R.T. Lareau, Absorption-desorption characteristics of explosive vapors investigated with microcantilevers, *Ultramicroscopy*, 97 (2003), 433-439.
- [3] T. Ono and M. Esashi, Magnetic force and optical force sensing with ultrathin silicon resonator, *Review of Scientific Instruments*, 74 (2003), 5141-5146.
- [4] J.W.M. Chon, P. Mulvaney, and J.E. Sader, Experimental validation of theoretical models for the frequency response of atomic force microscope cantilever beams immersed in fluids, *Journal of Applied Physics*, 87 (2000), 3978-3988.
- [5] A.M. Schilowitz, D.G. Yablon, E. Lansey, and F.R. Zypman, Measuring hydrocarbon viscosity with oscillating microcantilevers, *Measurement*, 41 (2008), 1169-1175.
- [6] S. Boskovic, J.W.M. Chon, P. Mulvaney, and J.E. Sader, Rheological measurements using microcantilevers, *Journal of Rheology*, 46 (2002), 891-899.
- [7] L. Bellon, Thermal noise of microcantilevers in viscous fluids, *Journal of Applied Physics*, 104 (2008), -.
- [8] N. Belmiloud, I. Dufour, A. Colin, and L. Nicu, Rheological behavior probed by vibrating microcantilevers, *Applied Physics Letters*, 92 (2008), -.
- [9] M. Hennemeyer, S. Burghardt, and R.W. Stark, Cantilever micro-rheometer for the characterization of sugar solutions, *Sensors*, 8 (2008), 10-22.
- [10] A.R.H. Goodwin, E.P. Donzier, O. Vancauwenberghe, A.D. Fitt, K.A. Ronaldson, W.A. Wakeham, M.M. De Lara, F. Marty, and B. Mercier, A vibrating edge supported plate, fabricated by the methods of micro electro mechanical system for the simultaneous measurement of density and viscosity: Results for methylbenzene and octane at temperatures between (323 and 423) K and pressures in the range (0.1 to 68) MPa, *Journal of Chemical and Engineering Data*, 51 (2006), 190-208.
- [11] P.I. Oden, G.Y. Chen, R.A. Steele, R.J. Warmack, and T. Thundat, Viscous drag measurements utilizing microfabricated cantilevers, *Applied Physics Letters*, 68 (1996), 3814-3816.
- [12] T. Thundat, P.I. Oden, and R.J. Warmack, Microcantilever sensors, *Microscale Thermophysical Engineering*, 1 (1997), 185-199.

- 
- [13] K.M. Goeders, J.S. Colton, and L.A. Bottomley, Microcantilevers: Sensing chemical interactions via mechanical motion, *Chemical Reviews*, 108 (2008), 522-542.
- [14] B. Rogers, L. Manning, M. Jones, T. Sulchek, K. Murray, B. Beneschott, J.D. Adams, Z. Hu, T. Thundat, H. Cavazos, and S.C. Minne, Mercury vapor detection with a self-sensing, resonating piezoelectric cantilever, *Review of Scientific Instruments*, 74 (2003), 4899-4901.
- [15] D.R. Franca and A. Blouin, All-optical measurement of in-plane and out-of-plane Young's modulus and Poisson's ratio in silicon wafers by means of vibration modes, *Measurement Science & Technology*, 15 (2004), 859-868.
- [16] A. Passian, R.J. Warmack, A. Wig, R.H. Farahi, F. Meriaudeau, T.L. Ferrell, and T. Thundat, Observation of Knudsen effect with microcantilevers, *Ultramicroscopy*, 97 (2003), 401-406.
- [17] C.A. Van Eysden and J.E. Sader, Resonant frequencies of a rectangular cantilever beam immersed in a fluid, *Journal of Applied Physics*, 100 (2006), -.
- [18] C.A. Van Eysden and J.E. Sader, Frequency response of cantilever beams immersed in compressible fluids with applications to the atomic force microscope, *Journal of Applied Physics*, 106 (2009), -.
- [19] F. Cansell, C. Aymonier, and A. Loppinet-Serani, Review on materials science and supercritical fluids, *Current Opinion in Solid State & Materials Science*, 7 (2003), 331-340.
- [20] Y.-P. Sun, *Supercritical fluid technology in materials science and engineering: synthesis, properties, and applications*, First Edition, CRC Press, (2002).
- [21] J.E. Sader, Frequency response of cantilever beams immersed in viscous fluids with applications to the atomic force microscope, *Journal of Applied Physics*, 84 (1998), 64-76.
- [22] A.M. Schilowitz, D. G. Yablon, and F. Zypman, Frequency Response of Microcantilevers in Viscous Fluids, *Mater. Res. Soc. Symp. Proc.*, Materials Research Society, 838E (2005).
- [23] A.R.H. Goodwin, A.D. Fitt, K.A. Ronaldson, and W.A. Wakeham, A vibrating plate fabricated by the methods of microelectromechanical systems (MEMS) for the simultaneous measurement of density and viscosity: Results for argon at temperatures between 323 and 423K at pressures up to 68 MPa, *International Journal of Thermophysics*, 27 (2006), 1650-1676.
- [24] A.R.H. Goodwin, C.V. Jakeways, and M.M. De Lara, A MEMS vibrating edge supported plate for the simultaneous measurement of density and viscosity: Results for nitrogen, methylbenzene, water, 1-propene, 1,1,2,3,3,3-hexafluoro-oxidized-polyimide, and polydimethylsiloxane and four certified reference materials with viscosities in the range (0.038 to 275) mpa.s and densities between (408 and 1834)

- 
- kg.m(-3) at temperature from (313 to 373) K and pressure up to 60 MPa, *Journal of Chemical and Engineering Data*, 53 (2008), 1436-1443.
- [25] A.R.H. Goodwin, A MEMS Vibrating Edge Supported Plate for the Simultaneous Measurement of Density and Viscosity: Results for Argon, Nitrogen, and Methane at Temperatures from (297 to 373) K and Pressures between (1 and 62) MPa, *Journal of Chemical and Engineering Data*, 54 (2009), 536-541.
- [26] L.D. Landau, and E.M. Lifshitz, *Fluid Mechanics*, Butterworth-Heinemann, (1981).
- [27] W.Y. Shih, X.P. Li, H.M. Gu, W.H. Shih, and I.A. Aksay, Simultaneous liquid viscosity and density determination with piezoelectric unimorph cantilevers, *Journal of Applied Physics*, 89 (2001), 1497-1505.
- [28] N. Belmiloud, I. Dufour, L. Nicu, A. Colin, and J. Pistre, Vibrating Microcantilever used as Viscometer and Microrheometer, *IEEE SENSORS 2006, EXCO, Korea*, (2006).
- [29] I. Etchart, H. Chen, P. Dryden, J. Jundt, C. Harrison, K. Hsu, F. Marty, and B. Mercier, MEMS sensors for density-viscosity sensing in a low-flow microfluidic environment, *Sensors and Actuators a-Physical*, 141 (2008), 266-275.
- [30] C.A. Van Eysden and J.E. Sader, Compressible viscous flows generated by oscillating flexible cylinders, *Physics of Fluids*, 21 (2009), -.
- [31] K. Otake, S. Kurosawa, T. Sako, T. Sugeta, M. Hongo, and M. Sato, Frequency Change of a Quartz-Crystal Microbalance at the Supercritical Condition of Carbon-Dioxide, *Journal of Supercritical Fluids*, 7 (1994), 289-292.
- [32] H.I. Ocakli, *Fabrication and Characterization of Magnetic Microresonators*, M.S. Thesis, Koc University, (2008).
- [33] A. Ozturk, *Development of a Diffraction-Grating Based Micro-Gravimetric Sensing Method for Biological Applications*, M.S. Thesis, Koc University, (2008).
- [34] M.S. Kilic, *Investigation of a Microgravimetric Sensor and Application to the Deflection of Protein-Antibody Interaction*, M.S. Thesis, Koc University, (2009).
- [35] <http://britneyspears.ac/physics/fabrication/photolithography.htm>.
- [36] <http://tst.ewi.utwente.nl/research/microfabrication/mmflowcontrollers/index.html>.
- [37] J.K. Luo, A.J. Flewitt, S.M. Spearing, N.A. Fleck, and W.I. Milne, Young's modulus of electroplated Ni thin film for MEMS applications, *Materials Letters*, 58 (2004), 2306-2309.
- [38] M.H. Bao and H. Yang, Squeeze film air damping in MEMS, *Sensors and Actuators a-Physical*, 136 (2007), 3-27.
- [39] <http://www.freepatentsonline.com/7524427.html>.
- [40] [http://www.polytec.com/eur/158\\_463.asp](http://www.polytec.com/eur/158_463.asp).
- [41] V. Cimalla, F. Niebelschuetz, K. Tonisch, C. Foerster, K. Brueckner, I. Cimalla, T. Friedrich, J. Pezoldt, R. Stephan, M. Hein, and O. Ambacher,



- 
- Nanoelectromechanical devices for sensing applications, *Sensors and Actuators B-Chemical*, 126 (2007), 24-34.
- [42] M.K. Jain and C.A. Grimes, Effect of surface roughness on liquid property measurements using mechanically oscillating sensors, *Sensors and Actuators a-Physical*, 100 (2002), 63-69.
- [43] R.B. Bird, W.E. Stewart, and E.N. Lightfoot, *Transport Phenomena*, New York, J. Wiley, (2007).
- [44] G. Mchale, C. Hardacre, R. Ge, N. Doy, R.W.K. Allen, J.M. MacInnes, M.R. Bown, and M.I. Newton, Density-viscosity product of small-volume ionic liquid samples using quartz crystal impedance analysis, *Analytical Chemistry*, 80 (2008), 5806-5811.
- [45] J.H. Lee, S.T. Lee, C.M. Yao, and W.L. Fang, Comments on the size effect on the microcantilever quality factor in free air space, *Journal of Micromechanics and Microengineering*, 17 (2007), 139-146.
- [46] T.L. Wilson, G.A. Campbell, and R. Mutharasan, Viscosity and density values from excitation level response of piezoelectric-excited cantilever sensors, *Sensors and Actuators a-Physical*, 138 (2007), 44-51.
- [47] J. Tamayo, A.D.L. Humphris, and M.J. Miles, Piconewton regime dynamic force microscopy in liquid, *Applied Physics Letters*, 77 (2000), 582-584.
- [48] <http://webbook.nist.gov/chemistry/fluid/>.